Computational Investigations of Transition Metal Based Catalyzed Organic Transformations

A thesis submitted

in the fulfillment for the award of the degree of

Doctor of Philosophy

Submitted by:

Akanksha Katoch

(Regn. no. 902009021)

Under the supervision of

Dr. Debasish Mandal

(Associate Professor)

DEPARTMENT OF CHEMISTRY AND BIOCHEMISTRY

THAPAR INSTITUTE OF ENGINEERING AND TECHNOLOGY

PATIALA-147004, PUNJAB, INDIA

July 2025

Certificate

This is to certify that the thesis entitled **"Computational Investigations of Transition Metal Based Catalyzed Organic Transformations,"** is being submitted by **Ms. Akanksha Katoch,** in the fulfilment of the requirement for the award of the Degree of Doctor of Philosophy in the Department of Chemistry and Biochemistry, Thapar Institute of Engineering and Technology, Patiala, is a record of candidate's own independent and original research work carried out by her under my supervision and guidance. The matter embodied in the thesis has not been submitted in part or full for the award of any degree in any other University or Institute.

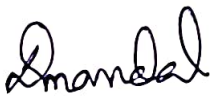

Dr. Debasish Mandal

Associate Professor and Supervisor

Department of Chemistry and Biochemistry

Thapar Institute of Engineering and Technology Patiala-147004, Punjab, India

Head:

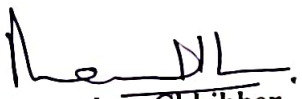

Dr. Manmohan Chhibber

Professor and Head

Department of Chemistry and Biochemistry

Thapar Institute of Engineering and Technology Patiala-147004, Punjab, India

Candidate's Declaration

I, hereby declare that the work presented in the thesis entitled **"Computational Investigations of Transition Metal Based Catalyzed Organic Transformations,"** in the fulfilment of the requirement for the award of the degree of Doctor of Philosophy in the Department of Chemistry and Biochemistry, Thapar Institute of Engineering and Technology, Patiala, is an authentic record of my work carried out under the supervision of **Dr. Debasish Mandal,** Associate Professor, Department of Chemistry and Biochemistry, Thapar Institute of Engineering and Technology, Patiala, India. The matter embodied in the thesis has not been submitted in part or full for the award of any degree in India or abroad.

Akanksha Katoch

Dr. Debasish Mandal

Associate Professor and Supervisor

Department of Chemistry and Biochemistry

Thapar Institute of Engineering and Technology Patiala-147004, Punjab, India

DEDICATED

TO

MY PARENTS

(MR. JAMEET CHAND KATOCH & MRS. SANTOSH KATOCH)

Acknowledgments

First and foremost, I want to express my deep gratitude to Almighty God for granting me the courage, patience, vision, and endurance necessary to complete this research.

I would like to extend my heartfelt gratitude and profound indebtedness to my doctorate advisor, **Dr. Debasish Mandal**, Associate Professor. Their unwavering support, expert guidance, and encouragement were crucial in navigating various research challenges and bringing this work to fruition.

I sincerely acknowledge **Dr. Padmakumar Nair**, honourable Director, **Dr. R. S. Kaler**, Dean of Research and Development Centre (DRDC), T.I.E.T, Patiala, for providing all the necessary facilities that have been immensely helpful in carrying out this research. I extend my sincere appreciation to **Dr. Manmohan Chhibber**, Professor and Head of the Department of Chemistry and Biochemistry at Thapar Institute of Engineering and Technology, Patiala, for his constant support and encouragement. I offer my sincere thanks to my doctoral committee members, **Dr. Amjad Ali, Dr. Bhupesh Goyal** and **Dr. Dheeraj Kumar**, for their crucial role in validating this research project. Their insightful feedback and scholarly discussions greatly enhanced the presentation and quality of my work. I am deeply grateful for the support provided by the entire faculty of the Department of Chemistry and Biochemistry at TIET, Patiala. I also want to express my sincere appreciation to all the administrative, technical, and office staff in the department, especially **Mr. Chander Thakur, Mr. Hemant** and **Mr. Mayank Sharma**, for their cooperation and assistance throughout the duration of my research.

I express my gratitude to our funding agencies, Department of Science and Technology (DST), the Government of India, for their financial support during the entire period of my doctoral research.

I gratefully acknowledge the help and support I got from my seniors **Dr. Pooja Soam**, and **Dr.**

Rajesh Kondabala. I would like to express my sincere gratitude to my fellow lab colleagues **Dr. Lovleen Kaur, Mr. Abinash Mohapatra**, and **Ms. Amanpreet Kaur** for their unwavering support and guidance during hard times. This entire journey would not have been possible without their indispensable contributions, rendering it an unforgettable and remarkable experience.

A very special thanks to my dearest friends **Dr. Jemini Dogra** and **Dr. Priya Kamboj** who have been my unwavering pillars of support throughout the journey of my Ph.D. Their presence, encouragement and belief in me have been invaluable, not just during the highs, but in every challenging phase along the way. Both of them not only shared in my successes but also stood by me during the struggles, making this journey all the more meaningful. I am truly blessed to have friends like them, and I will forever cherish the memories of this incredible journey together. I would also like to express my thanks to my friends and hostel mates **Dr. Monika Barak, Ms. Anshika Khandwal, Mrs. Harmanjot Kaur, Mrs. Sukhandeep Kaur, Ms. Damanjot Kaur, Ms. Azra Showkat, Ms. Parmjeet Kaur, and Ms. Asmita Sharma** for their unwavering support, consistent communication and dedicated efforts to ensure my well-being.

I can't put my thoughts or feelings into words to show my heartfelt appreciation to my respected parents, **Mr. Jameet Chand Katoch** and **Mrs. Santosh Katoch**. Their unwavering blessings, steadfast beliefs, and constant encouragement have guided me toward achieving my goals. They have been the driving force behind my growth into the person I am today. Whether near or far during this research journey, their insightful advice and support have been a constant presence, profoundly influencing the progress of my work. A big thanks to my loving sister **Dr. Sonali Katoch** and brother-in -law **Mr. Nitish Thakur** for their care and unwavering support. A special thanks to my little star, **Mr. Vedant Thakur** for bringing immense joy into my life and being the source of my happiness.

I express my gratitude to all the individuals who, despite not being acknowledged here, have provided assistance, whether consciously or unconsciously, in the successful completion of my thesis.

Akanksha Katoch

DFT	Density functional Theory
SSR	Single State Reactivity
TSR	Two State Reactivity
MSR	Multistate Reactivity
QMT	Quantum Mechanical Tunneling
CYP450	Cytochrome P450
TauD	Taurine/α-ketoglutarate dioxygenase
ACCO	1-aminocyclopropane-1 carboxylic acid oxidase
PheH	Phenylalanine hydroxylase
O_2	Oxygen
TMC	1,4,8,11-tetramethyl-1,4,8,11-tetraazacyclotetradecane
TMCS	1-mercaptoethyl-4,8,11-trimethyl-1,4,8,11-tetraazacyclotetradecane
TATM	1,4,7,10-tetramethyl-1,4,7,10-tetraazacyclotridecane
TAPM	1,4,8,12-tetramethyl-1,4,8,12-tetraazacyclopentadecane
TAPH	1,4,8,12- tetraazacyclopentadecane
TPA	tris(2-pyridylmethyl)amine
QBPA	(2-quinolylmethyl)bis(2-pyridylmethyl)amine
BPMCN	N,N-bis(2- pyridylmethyl)-N,N-dimethyl-trans-1,2-diaminocyclohexane
N4Py	N,N-bis(2-pyridylmethyl)-N-bis(2-pyridyl)methylamine
R-TPEN	N-R-N,N′,N′-tris(2-pyridylmethyl)ethane-1,2-diamine
Bispidine	3,7-dimethyl-9,9′-dihydroxy-2,4-di(2-pyridyl)-3,7-diazabicyclononane-1,5- dicarboxylate
Dpaq	bis(pyridine-2-yl-methyl)]amino-N-quinolin-8-yl-acetamido
Py	Pyridine
EDGs	Electron Donating Groups
EWGs	Electron Withdrawing Groups
HAT	Hydrogen Atom Transfer
PCET	Proton-Coupled Electron Transfer

OAT	Oxygen Atom Transfer
VB	Valence Bond
EER	Exchange-Enhanced Reactivity
BEP	Bell-Evans-Polanyi
ClO_4^-	Perchlorate Ion
$CF_3SO_3^-$	Triflate
Fe	Iron
Mn	Manganese
Cr	Chromium
Ru	Ruthenium
Co	Cobalt
R	Reactant
TS	Transition State
IH	Intermediate
CH_3CN	Acetonitrile
QM	Quantum Mechanics
KIE	Kinetic Isotope Effect
HF	Hartree Fock
G.S	Ground State
LDA	Local Density Approximation
GGA	Generalised Gradient Approximation
B	Becke
LYP	Lee-Yang-Parr
B3LYP	Becke, 3-parameter, Lee-Yang-Parr
STOs	Slater-type orbitals
GTOs	Gaussian-type orbitals
AOs	Atomic orbitals
SCRF	Self-Consistent Reaction Field
CPCM	Conductor-like Polarizable Continuum Model
SMD	Solvation Model based on Density
ZPVE	Zero-point vibrational energy
IRC	Intrinsic Reaction Coordinate
ax	Axial

DHA	Dihydroanthracene
LANL2DZ	Los Alamos National Laboratory 2 Double Zeta
ECP	Effective Core Potential
SDD	Stuttgart Dresden
EB	Ethyl Benzene
BA	Benzyl Alcohol
DHA	Dihydroanthracene
CHD	Cyclohexadiene
CHE	Cyclohexane
NHPI	N-hydroxyphthalimide
NHQI	N-hydroxyquinolinimide
PINO	Phthalimide-N-oxyl radical
QINO	Quinolinimide-N-oxyl radical
kcal/mol	Kilocalories per mole
eV	Electron Volt
PES	Potential Energy Surface
LUMO	Lowest Unoccupied Molecular Orbital

Symbols	Description
H^+	Proton (Hydrogen ion)
e^-	Electron
.+	Radical cation
σ	Sigma
π	Pi
α	Alpha spin
β	Beta spin
ΔE_{T-Q}	Spin State Gap
Å	Angstrom
$\hat{H}$	Hamiltonian operator
Ψ	Wavefunction
$\hat{F}$	Fock operator
ϕ	Molecular orbital
ε	Energy
ρ	Electron Density
ζ	Effective nuclear charge
r	Radius
*	Polarisation function
+	Diffuse Function
k	Rate Constant
κ	Transmission Constant
δ	Sigma
ΔG	Gibbs free energy change
K	Kelvin
°	Degrees
i	Imaginary Frequency
a.u.	Atomic unit
$\%V_{bur}$	Buried Volumes
$\Delta E^{\ddagger}_{dis}$	Distortion Energy

Chapter one provides a comprehensive overview of transition metal complexes, with a focus on the catalytic roles of iron complexes in reaction mechanisms, particularly oxidation reactions mediated by Fe(IV)O species, including non-heme variants. It reviews relevant literature on biologically inspired enzymes and biomimetic complexes, discussing key concepts like Two-State Reactivity and electron/proton transfer mechanisms. The chapter also examines the impact of ligand and metal substitutions on Fe-oxo reactivity, highlighting the role of carboxylate-rich macrocycles and mediators. It identifies key gaps in the current literature, with particular attention to recent advancements in the field. These insights are critical for guiding the rational design of next-generation catalysts that aim to improve performance and selectivity. The chapter concludes by outlining the objectives of the current research, which seeks to address these identified gaps.

Chapter two introduces the core principles and methods of computational chemistry, starting with quantum mechanics and the Schrödinger equation. It covers approximations like the Born-Oppenheimer and Hartree-Fock methods, addressing their limitations in electron-electron correlations. The chapter also explores post-Hartree-Fock methods and Density Functional Theory (DFT), highlighting its balance between efficiency and accuracy. Key computational tools, such as Gaussian 16 for geometry optimization and Chemcraft for molecular visualization, are discussed. The chapter lays the foundation for understanding computational chemistry techniques used in the research, setting the stage for further exploration.

Chapter three presents a DFT study on C–H activation reactivity and quantum mechanical tunneling in catalysis by a non-heme iron(IV)-oxo complex, $[Fe^{IV}(O)(dpaq\text{-}X)]^{+}$. The study incorporates solvent and counter-ion corrections to eliminate self-interaction errors. The dpaq ligand was modified at the 5-position of its quinoline moiety, resulting in dpaq-X, and its reactivity was compared with the original dpaq-H. Various electron-donating (e.g., $–N(CH_3)_2$, –OMe) and electron-withdrawing (e.g., $–NO_2$, $–SO_2CF_3$) substituents were studied. The

reactions favored two-state reactivity (TSR), with the S = 2 state crossing the S = 1 path during the reaction. This was confirmed by the tunneling-corrected kinetic isotope effect (KIE), which matched experimental data for the S = 2 state. Over 90% of C–H activation reactions proceeded via quantum mechanical tunneling at room temperature. More electron-donating groups increased tunneling contributions and KIE, supporting the anti-electrophilic tunneling control reactivity hypothesis. These results suggest the potential for designing metal-based catalysts by tuning ligands and substituents to optimize catalytic efficiency through tunneling effects.

Chapter four presents a DFT study comparing the C–H activation reactivity of high-valent iron-oxo and ruthenium-oxo complexes, focusing on four compounds: [Ru(IV)O(tpy-dcbpy)] (1), [Fe(IV)O(tpy-dcbpy)] (1'), [Ru(IV)O(TMCS)] (2), and [Fe(IV)O(TMCS)] (2'). The tpy-dcbpy macrocycle framework includes 2,2':6',2''-terpyridine, and 5,5'-dicarboxy-2,2'-bipyridine, while TMCS is TMC with an axially tethered $–SCH_2CH_2$ group. Compounds 1 and 2' are experimentally synthesized, and 1' and 2 maintain the macrocycle integrity with different metal centers. Three substrates—dihydroanthracene, benzyl alcohol, and ethyl benzene—were used for C–H activation. Fe(IV)O complexes showed greater reactivity than Ru(IV)O complexes, and the tpy-dcbpy macrocycle exhibited higher reactivity than TMCS, regardless of the metal. The study examined factors influencing reactivity, including spin state, steric effects, distortion energy, electron acceptor orbital energy, and quantum mechanical tunneling. Fe(IV)O complexes displayed enhanced two-state reactivity with a quintet state, while Ru(IV)O complexes had only a triplet state. Fe(IV)O also had lower acceptor orbital and distortion energies, supporting its increased reactivity. Hydrogen tunneling contributed significantly to C–H activation, especially for Ru, though it did not change the reactivity trend. The study concluded that enzymes prefer Fe over Ru as a cofactor for C-H activation due to these reactivity differences.

Chapter five presents a DFT analysis of the impact of a carboxylate-rich macrocycle on the reactivity of a non-heme Fe(IV)O complex in C–H activation. The study uses the non-heme iron oxo complex $[FeIV(O)(N4Py)]^{2+}$ (1) as the base compound, which is modified to form $[FeIV(O)(^{n}Bu\text{-}P2DA)]$ (2) by replacing two pyridine donors with carboxylate groups. Two other complexes (3 and 4) are modeled with progressively more carboxylate groups. The study finds that the reactivity increases with more carboxylate groups (1 < 2 < 3 < 4), aligning with experimental results for complexes 1 and 2. Factors affecting reactivity include spin inversion, available space for the abstractor, deformation energies, and the electrophilicity of the metal center. Hydrogen tunneling plays a role but doesn't significantly alter the reactivity trend. The findings suggest that incorporating more carboxylate groups could inspire the development of more efficient oxidants with carboxylate-enriched ligated macrocyclic compounds.

Chapter six presents a computational study on Fe(IV)O-catalyzed C–H activation, enhanced by N-hydroxy mediators. The analysis focuses on the Fe(IV)O complex $[Fe(IV)\text{-}ON4Py]^{2+}$ (1) with mediators N-hydroxyphthalimide (NHPI) and N-hydroxyquinolinimide (NHQI), examining three substrates: ethylbenzene, cyclohexane, and cyclohexadiene. The results show that the mediators significantly improve reactivity, with complex 1 predominantly following the S = 1 pathway, as indicated by the primary H/D kinetic isotope effect. The cleavage of the NO−H bond is more favorable than C–H activation, explained by the slower self-exchange reaction rate for C–H bonds compared to O–H bonds. Aminoxyl radicals, more reactive than Fe(IV)O species, are quickly generated, reducing activation energy. The study aligns with the Bell-Evans-Polanyi principle, showing that the mediator route is preferred. NHQI is more efficient than NHPI, and the kinetic isotope effect supports the role of quantum mechanical tunneling. This study highlights the potential for developing more effective mediators, encouraging further exploration to improve metal-oxo complex reactivity.

CHAPTER 1

Introduction & Literature Review

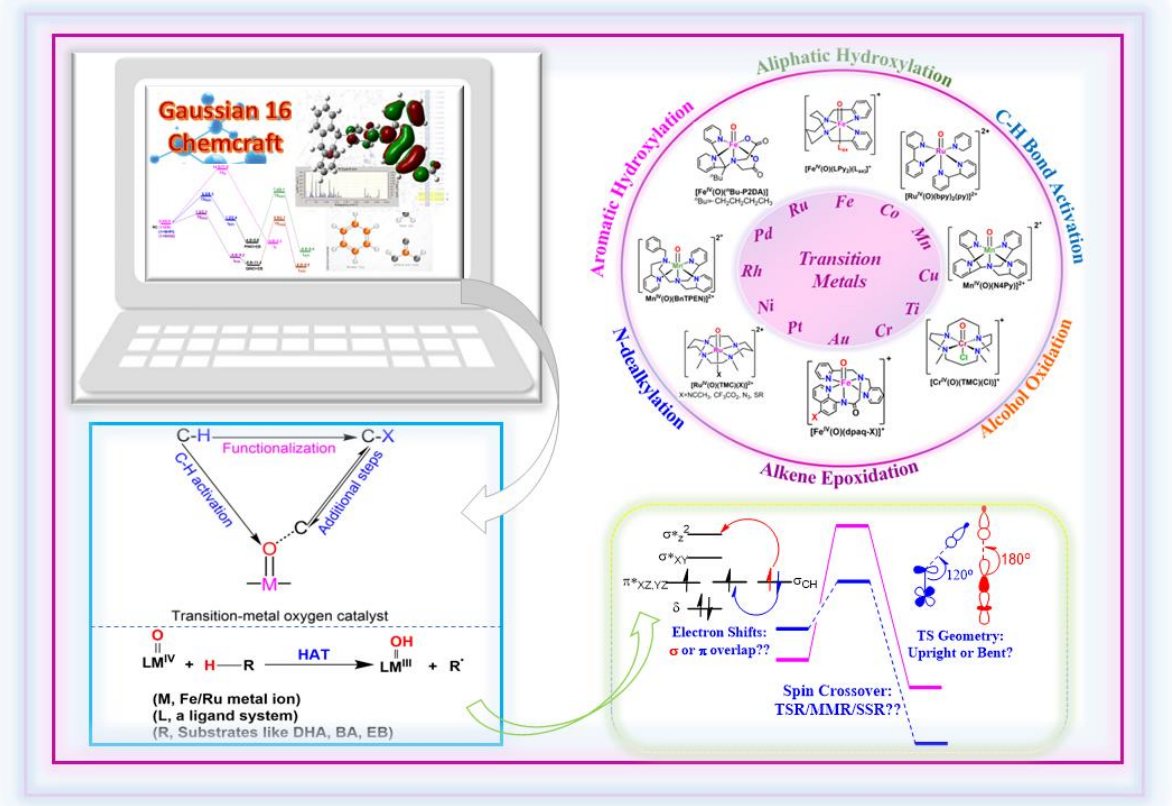

1.1: The Functions and Applications of Transition Metal-Centered Complexes

Within the domain of inorganic chemistry, transition metal-based complexes are of considerable importance due to their distinctive ability to coordinate with a diverse range of ligands—a characteristic derived from their d orbitals.[1] Transition metal complexes are pivotal across various domains, including medicinal chemistry, where platinum-based cisplatin and titanium in titanocene dichloride serve as effective anticancer agents, and metals such as silver, zinc, and manganese exhibit notable antimicrobial, antifungal, and antimalarial properties.[2] In industrial catalysis, iron plays a critical role in the Haber-Bosch process, while nickel is extensively utilized in hydrogenation reactions.[3] Additionally, they play important roles in biological systems, materials science, and catalysis within synthetic chemistry. A summary of their diverse applications is presented in Fig. 1.1.[4]

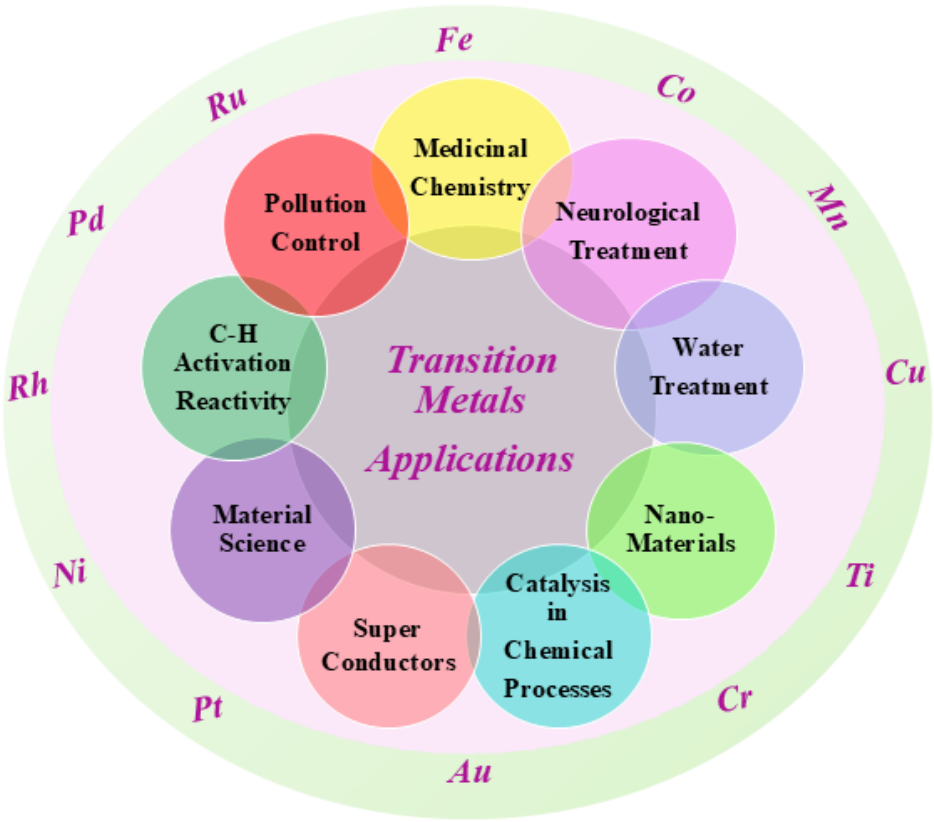

Fig. 1.1 The diverse applications of transition metal-based compounds.

1.2: Iron-Based Complexes in Catalytic Processes

Among the different states of oxidation, i.e., III, IV, and V, iron has been discovered to be a crucial part of the active sites of numerous catalytic reactions.[5-8] Its economic viability, low toxicity, and bioavailability have prompted extensive investigation within the domains of biomimetic chemistry as well as biological systems.[9] Our research has been based on these types of complexes, which are therefore a perfect topic for in-depth study. Iron-based complexes are also involved in a wide array of reactions, including hydrogenolysis, cyclization, oxidation, and cyclopropanation,[10,11] with oxidation processes—such as aliphatic and aromatic hydroxylation, alkene epoxidation, alcohol oxidation, C-H bond activation, N-dealkylation, etc.,[12-26] being particularly prevalent, as shown in Fig. 1.2.

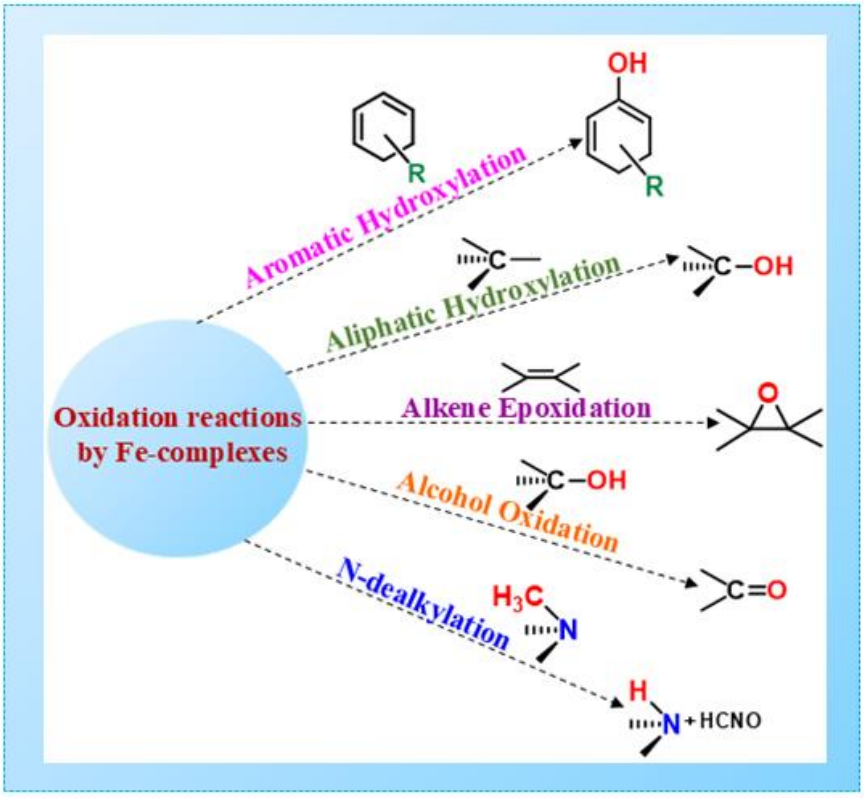

Fig. 1.2 Numerous ways of the oxidation process catalyzed by Fe complexes.

This thesis will concentrate on hydroxylation reactions, specifically C-H activation processes, which are crucial aspects of modern chemistry.[27,28] Due to the complex interplay of several

factors influencing reactivity behavior—such as the ligand's coordination at the axial or equatorial position to the central metal,[29] overall ligand structure,[30] acceptor orbital energy,[31] spin-state (which governs whether the reactivity follows single, two, or multi-state pathways),[32,33] and quantum mechanical tunneling (QMT)[34]—it is highly challenging to characterize and fully understand the reactivity patterns of these bond-activation processes.

1.3: Impact of Iron-Based Complexes on Biological Systems

1.3.1: Classification of Iron-Based Complexes

Iron complexes can be systematically arranged into separate classes based on their structural characteristics.[35,36] In terms of the ligand ring structure, these complexes are usually divided into two broad categories:

(a) Heme complexes and **(b)** Non-heme complexes

In numerous essential enzymes, such as cytochromes and peroxidases,[37-39] etc., heme complexes serve as integral prosthetic groups or catalytic sites. These complexes are structurally characterized by a central iron atom bonded to a large, cyclic porphyrin ring, which has four subunits of pyrrole connected by methine bridges, forming a heterocyclic macrocycle. This structure is exemplified by cytochrome P450 enzymes[40-42] (Fig. 1.3a). These enzymes are pivotal in various biological processes, including drug metabolism and steroid synthesis. Multiple bioinspired approaches have been used to recreate the structural framework of heme, where the porphyrin's ring configuration in its natural form has been extensively studied[43] and modified, resulting in a diverse array of analogs such as phthalocyanine,[44] thereby broadening the scope of heme-based systems in catalysis, as depicted in Fig. 1.3b.

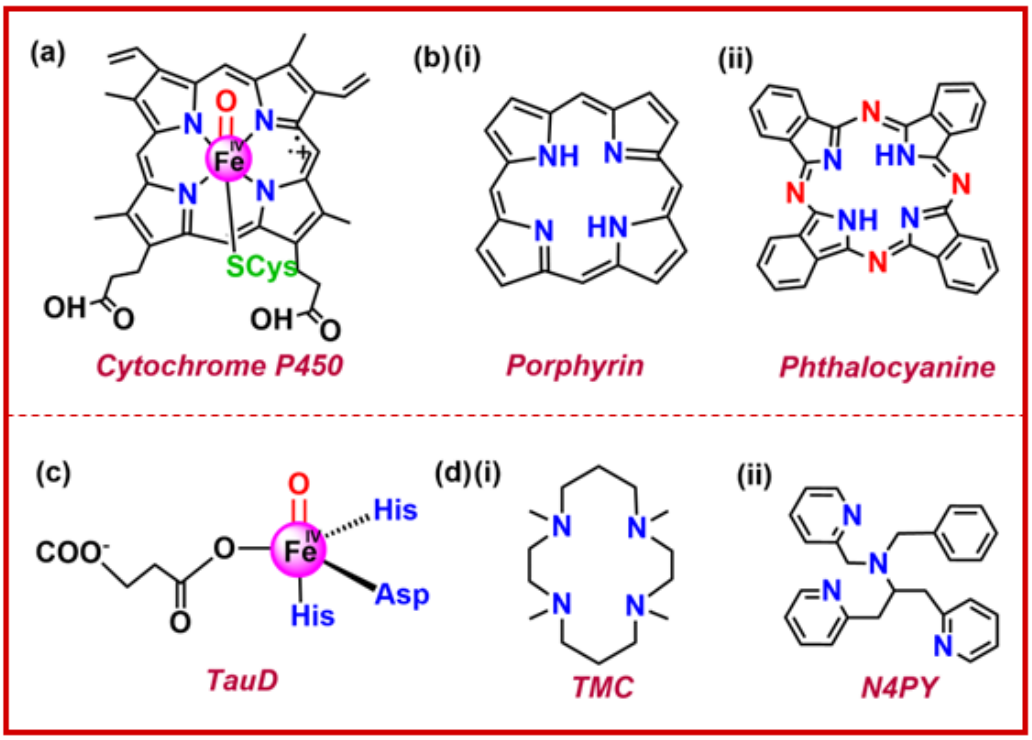

Fig. 1.3 Structure for heme enzymatic model (a) Cytochrome P450 (b) Heme frameworks: Porphyrin and its analog. Structure for a non-heme enzymatic model (c) TauD d) Non-heme frameworks: TMC and N4Py.

Conversely, non-heme iron complexes, function as catalytic centers in several enzymes like TauD (taurine/α-ketoglutarate dioxygenase)[45] (Fig. 1.3c), ACCO (1-aminocyclopropane-1-carboxylic acid oxidase),[46] and PheH (phenylalanine hydroxylase).[47] Rather than coordinating directly with porphyrin rings, these complexes interact with non-porphyrin ligands, including residual amino acid, water, or some additional heteroatoms in their structure, as demonstrated in Fig. 1.3d. This coordination allows for a diverse range of catalytic reactions. Despite the lack of a porphyrin ring, non-heme complexes exhibit considerable catalytic versatility, enabling them to facilitate a broader spectrum of reactions compared to their heme counterparts.[48-51] Additionally, we have discussed how the properties of the metal-oxygen link might affect the complexes that result from O being attached to the Fe atom.

1.3.2: Different Forms of Iron-Oxygen-based Complexes

Iron-oxygen bonding complexes can be categorized into oxo, superoxo, and peroxo complexes, each distinguished by the specific nature of the metal-oxygen interaction.[52,53] In oxo complexes, the iron center is covalently bonded to an oxygen atom via a double bond,[54-57] as represented in Fig. 1.4(a).

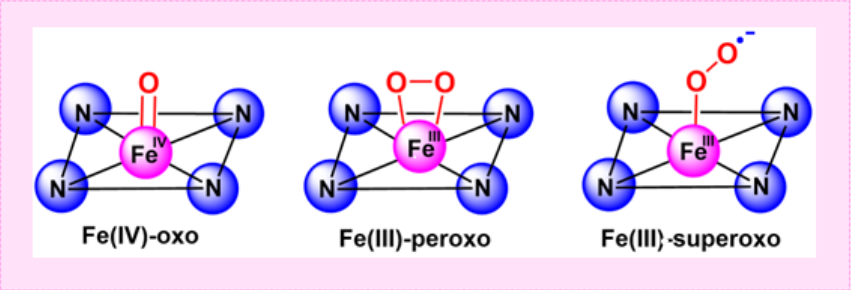

Fig 1.4 Different types of metal complexes: (a) Oxo, (b) Peroxo, and (c) Superoxo.

Conversely, peroxo complexes are characterized by an iron-oxygen bond in which the oxygen molecule (O_2) serves as a bridging ligand, forming a stable peroxo structure,[58] (Fig. 1.4(b)). Complexes with superoxide groups, meanwhile, feature an iron associated with an oxygen-containing moiety in an end-on manner, where the O_2 entity behaves like a superoxo ligand,[59] (Fig. 1.4(c)). This study primarily examines oxo complexes, serving as pivotal intermediates in C-H activation and playing an integral role in facilitating a wide array of catalytic reactions.

1.4: The Role of Iron-Oxo Complexes in Biomimetic Chemistry

A considerable number of researchers specializing not only in biological but also in bioinorganic and oxidation chemistry have developed catalysts incorporating the ferryl moiety. The pioneering biomimetic model system in this domain was the TMC (1,4,8,11-tetramethyl-1,4,8,11-tetraazacyclotetradecane), a tetraazamacrocyclic ligand, introduced by Rohde *et al.*[60] This system laid the groundwork for developing numerous synthetic non-heme Fe compounds, which have been designed to replicate the enzymatic intermediates' properties such as

spectroscopic characteristics, functionality, or architecture.[61,62] Additionally, various other Fe-oxo complexes have been synthesized utilizing a range of macrocyclic ligands, including tetradentate (N4), tripodal tetradentate (N4), as well as N5 and N4S pentadentate (N5 and N4S) coordinating ligands, as illustrated in Fig. 1.5.[18, 63]

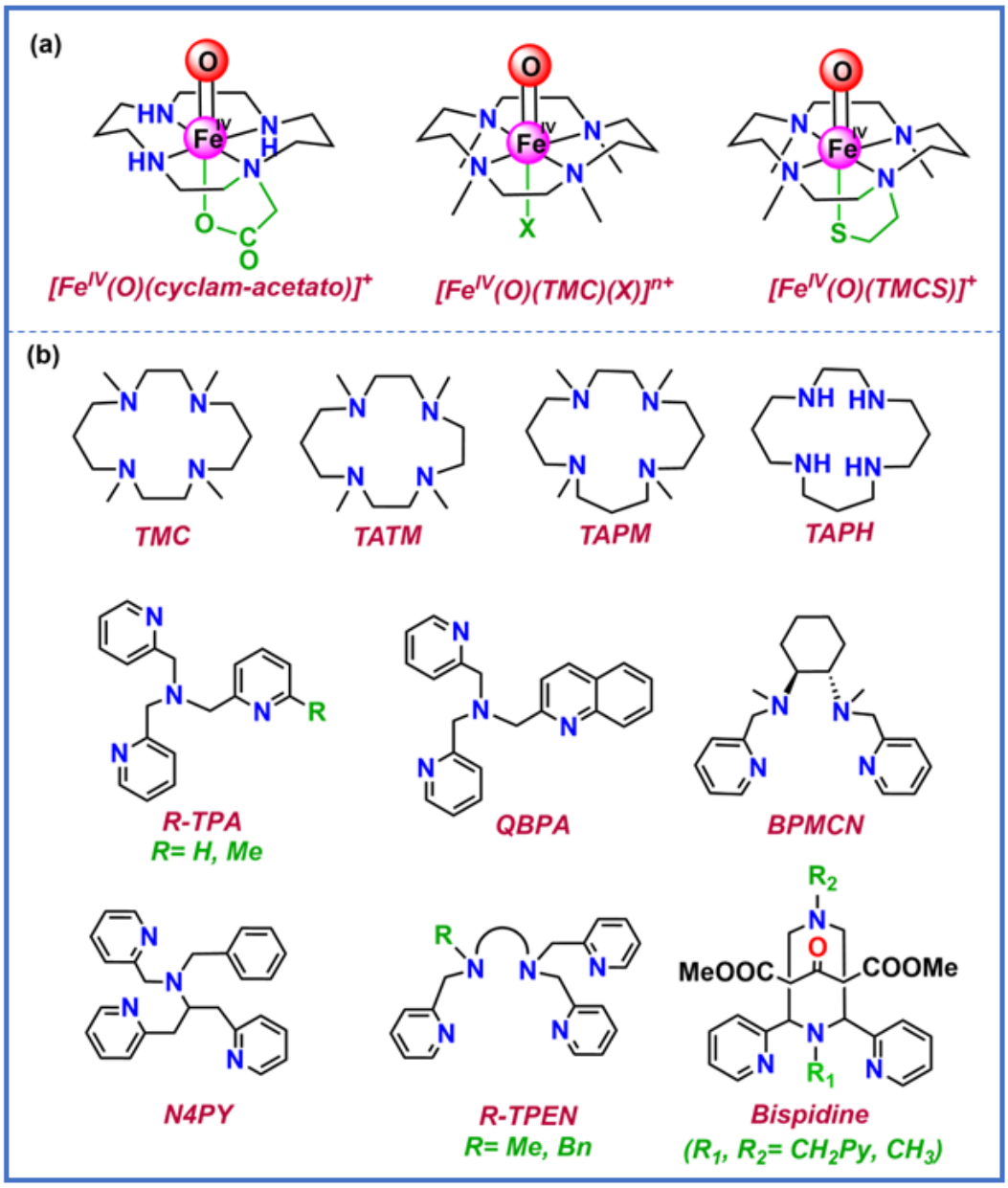

Fig. 1.5 Structures of iron(IV)–oxo complexes and ligands: cyclam-acetate, 1,4,8,11-tetraazacyclotetradecane 1-acetate; TMC, 1,4,8,11-tetramethyl-1,4,8,11-tetraazacyclotetradecane; TMCS, 1-mercaptoethyl-4,8,11-trimethyl-1,4,8,11-

tetraazacyclotetradecane; TATM, 1,4,7,10-tetramethyl-1,4,7,10-tetraazacyclotridecane; TAPM, 1,4,8,12-tetramethyl-1,4,8,12-tetraazacyclopentadecane; TAPH, 1,4,8,12-tetraazacyclopentadecane; TPA, tris(2-pyridylmethyl)amine; QBPA, (2-quinolylmethyl)bis(2-pyridylmethyl)amine; BPMCN, N,N-bis(2- pyridylmethyl)-N,N-dimethyl-trans-1,2-diaminocyclohexane; N4Py, N,N-bis(2-pyridylmethyl)-N-bis(2-pyridyl)methylamine; R-TPEN, N-R-N,N′,N′-tris(2-pyridylmethyl)ethane-1,2-diamine; Bispidine, 3,7-dimethyl-9,9′-dihydroxy-2,4-di(2-pyridyl)-3,7-diazabicyclononane-1,5- dicarboxylate.

A notable feature of many such macrocycles is the collective ligand framework, which predominantly originated from the TMC or alternative similar ring systems, namely N4Py and Me_2EBC, etc.[64-67] In light of these developments, the following section will focus on key aspects of this field.

1.4.1: Mechanistic Pathways for C-H Activation through the Transfer of Electrons and Protons

The process of hydrogen atom transfer (HAT) entails the concerted movement of a proton as well as an electron within two distinct types of substrates, occurring as a singular–kinetic phase.[68,69] From a conceptual standpoint, HAT is a subset within the more extensive class of proton-coupled electron transfer (PCET) processes, where both a proton along with the electron shift simultaneously in tandem, occupying in the same origin and ending orbitals.[70] Several investigative teams, are dedicated to constructing models that can explain HAT and predict the associated rates. A framework rooted in Marcus' theory[71] has been created to characterize HAT, and the valence bond (VB) model system has demonstrated its ability to effectively evaluate energy barriers in this process (hydrogen abstraction) and recognize patterns in bond energy values.[72] In many chemical reactions such as hydrocarbon combustion, oxidation (aerobic), and atmospheric processes, HAT is considered to be an important step. In biological systems,

it affects metalloenzymes, reactive oxygen species ROS activity, and antioxidant functioning.[73,74] Furthermore, HAT provides significant potential in organic synthesis by enabling the activation of bonds (R–H) selectively.[75] Fig. 1.6 outlines the general HAT mechanism.

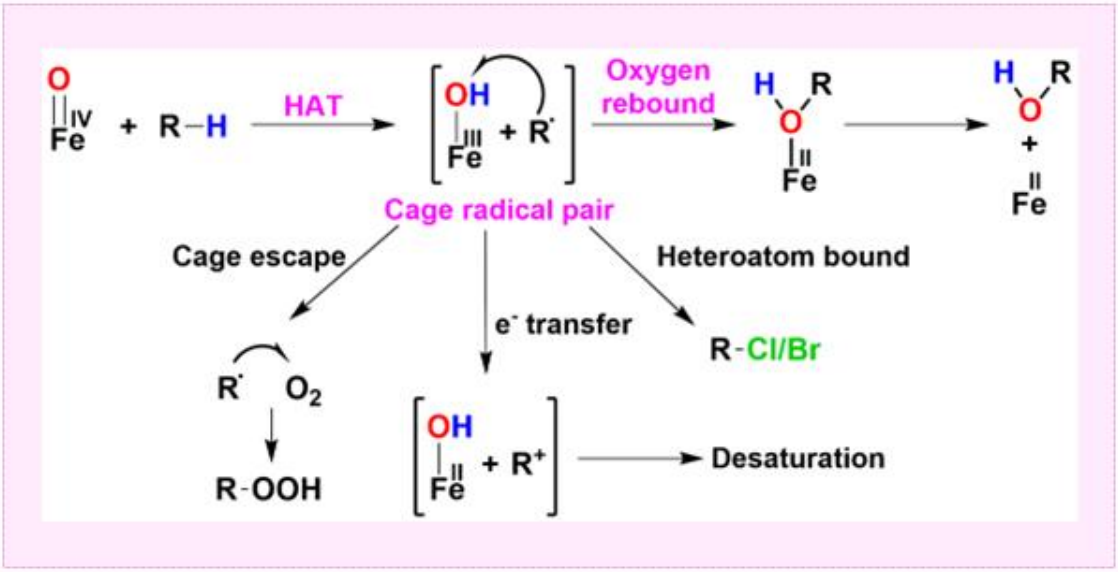

Fig. 1.6 Hydrogen atom transfer (HAT) mechanism.

1.4.2: Rearrangements of Electrons in Fe-Oxo Complexes

While the C–H activation reaction occurs, hydrogen is abstracted as a result of a single electron migrating from the substrate to the orbital of the acceptor.[76,77] According to the Fig. 1.7, this orbital could either be the π*, anti-bonding nature (in the case of $S = 1$, designated as triplet state) or the σ^*_{z2} (when $S = 2$, defined as quintet state) of the Fe(IV)oxo entity.

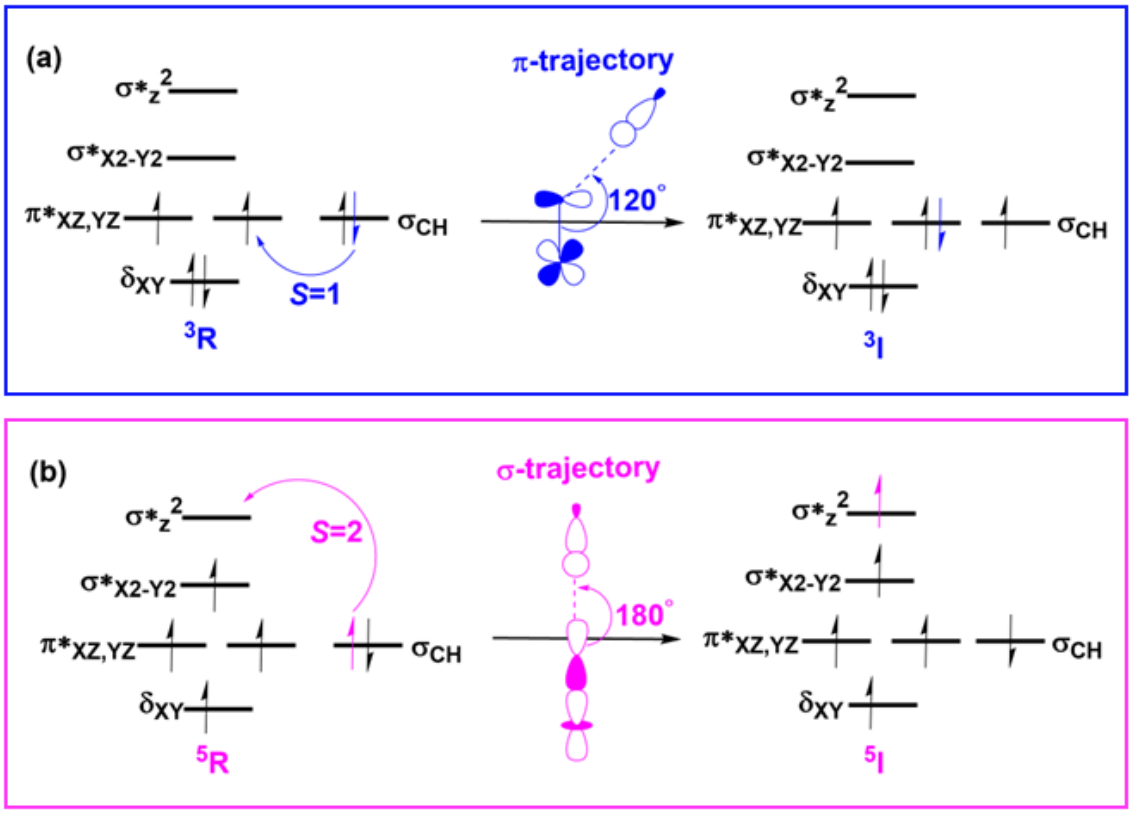

Fig. 1.7 The electron transfer diagram for spin states S = 1 (blue) and S = 2 (pink) during hydrogen atom transfer facilitated by Fe(IV)O complexes.

As represented in the figure above, S = 1 spin-state (referred to as the π route), which has a Fe–O–H angle of approximately 120°, the movement of an electron (β) to the Fe-oxo entity's π* orbital (demonstrated in blue) is facilitated. Conversely, within the S = 2 state, the transfer of an electron (α), via the σ path to the σ^*_{z2} orbital is highlighted by the pink arrow, with the Fe–O–H angle being about 180°. In this thesis, our findings are consistent with exchange-enhanced reactivity (EER), where the quintet state's transition state is energetically more suited than the triplet state's, owing to exchange interactions.[78,79] Consequently, the quintet state forms a more stable intermediate during the reaction.

1.4.3: Distinct Forms of Spin-State Reactivity

Reactivity can differ depending on the spin-states present,[80] as outlined below.

Fig. 1.8a illustrates **Single-State Reactivity (SSR)**, which involves a reaction that occurs solely via one spin state, with other spin states being much higher in energy than the ground state's energy level. Another type is the **Two-State Reactivity (TSR)**, which describes a reaction that proceeds via two separate spin states, which may be closely aligned (as seen in Fig. 1.8b) or involve a transition between various states on the reaction surface,[81] as demonstrated in Fig. 1.8c. Lastly, **Multi-State Reactivity (MSR)** addresses more complicated reactions, where multiple spin states (typically more than two) are involved, permitting interconversions between different arrangements of electrons along the pathway of the reaction, as depicted in Fig. 1.8d.

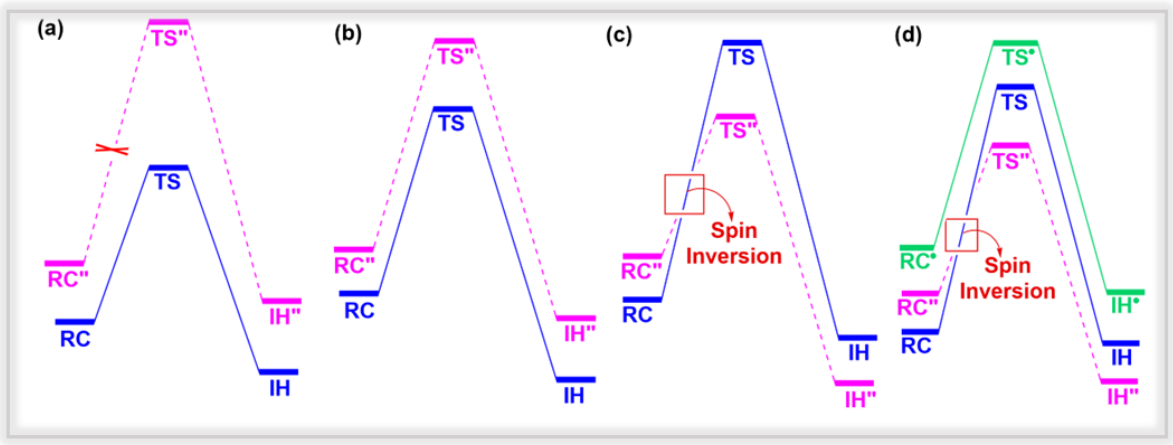

Fig. 1.8 a) SSR, b) and c) TSR, d) MSR, respectively where R represents the reactant, TS is the transition state, and IH denotes the intermediate, along with the reaction coordinates.

1.4.4: The Structural Roles of Ligands Substitution and the Influence of Metal Ions on the Fe-Oxo Complexes

Given the central role of C-H bond activation in this research, it is anticipated that the literature on this subject will broaden considerably. This increasing body of work provides a foundation for examining the structural contributions of the ligand and the effects of substrates and mediators in such reactions. Mandal *et al.*[82] put forward an idea of utilizing KIE to explore

tunneling phenomena and examine the spin-states reactivity pattern in M=O complexes. Their findings pointed that the surfaces exhibiting thermoneutral symmetry has the most prominent tunnelling effect, highlighting the significance of the Bell-Evans-Polanyi (BEP) principles governing quantum mechanical tunneling. In a related study, Janardanan *et al.*[83] addressed the issue of inaccuracies caused by self-interaction in DFT investigations of Fe-oxo complexes. They introduced a solution involving the use of counter-ions (ClO_4^-), in the $[(N4Py)FeIV(O)]^{2+}$ complex to improve computational accuracy and yield better predictions of experimental reactivity trends, as illustrated in Scheme 1.1.

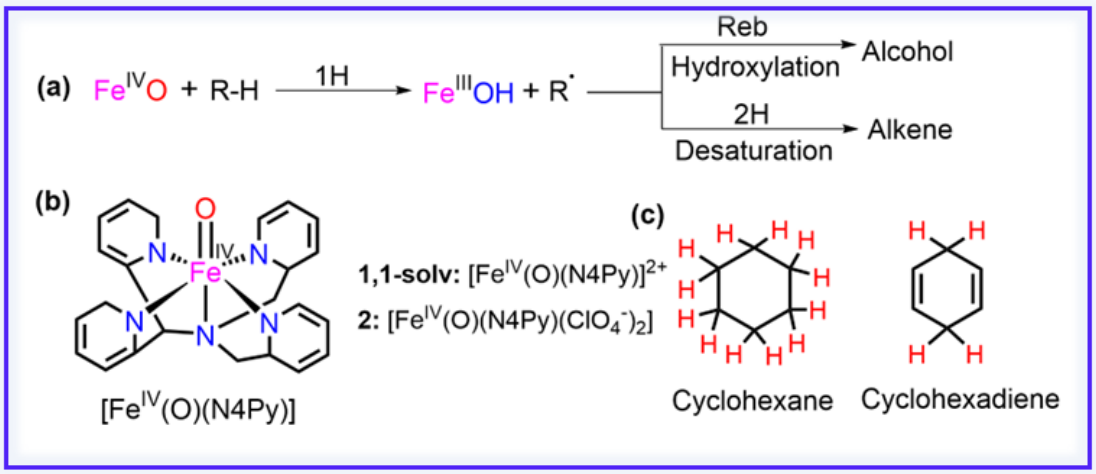

Scheme 1.1 (a) HAT reaction (b) Fe oxo-complex and (c) different substrates (adapted from reference 83).

In line with this study, Mandal *et al.*[84] also explored Fe(IV)O complex reactivity with macrocyclic ligands and L_{ax}, focusing on different types of substrates (CHD, DHA, etc.) for HAT as well as OAT reactivity. According to their research, tunneling contributions counteract the inherent electrophilic behavior in the H-abstraction by enhancing tunneling as L_{ax}'s electron-donating strength is amplified. In a similar vein, Park *et al.*[85] investigated that Fe(III)-hydroperoxo entities are unreactive not only for nucleophilic but also for electrophilic reactions. They also demonstrated that, in contrast to Fe(IV)O complexes, these entities act as

less reactive oxidants. Another important research focus has been the role of electron-tuning via substitutions on the ligand, linked to the metal centre.

A number of $[FeIV(O)(LPy_2)(L_{ax})]^{2+}$ complexes were examined in a research by Que and co-workers [86] where L_{ax} stood for various substituents at the 4th position of the pyridine (axial) in ligands (i.e. N-oxide). According to their findings, higher concentrations of electron-donating groups (similar to those seen in the well-known Fe-oxo complex with the TMC ligand)[87] led to the faster rates of HAT. Moreover, Hitomi *et al.*[88] experimentally synthesised a $[FeIV(O)(dpaq-X)]^{+}$ complex and found that it showed significantly higher reactivity compared to the Fe-oxo complex ligated with the ligand N4Py.[89]

Metal-oxo complexes of Mn, Cr, and Ru, etc., in their high oxidation states, have also shown tremendous promise in catalysing C–H activation processes, despite the fact that Fe-centered moieties have attracted significant attention.[90-93] Our understanding of metal-oxide chemistry is enhanced by the diverse reactivity behaviours and the arrangement of electrons that these metals offer. The catalytic efficiency of biomimetic heme in conjunction with nonheme Mn(IV)O complexes for C–H activation has been demonstrated in a number of investigations.[94-98] The catalytic capabilities of the complex $[(Bn\text{-}TPEN)Mn^{IV}O]^{2+}$ towards activation of C-H bonds were experimentally established by Cho *et al.*[99] According to the results of their inquiry, (Scheme 1.2), the H-abstraction substrate radical separates from the $Mn^{III}OH$ complex and then reacts with a second $Mn^{IV}O$ molecule to create Mn^{III}. Additionally, they highlighted the spin-state relevance for M=O reagents, pointing out that, nonheme $Mn^{IV}O$ displays a more complicated structure than $Fe^{IV}O$.

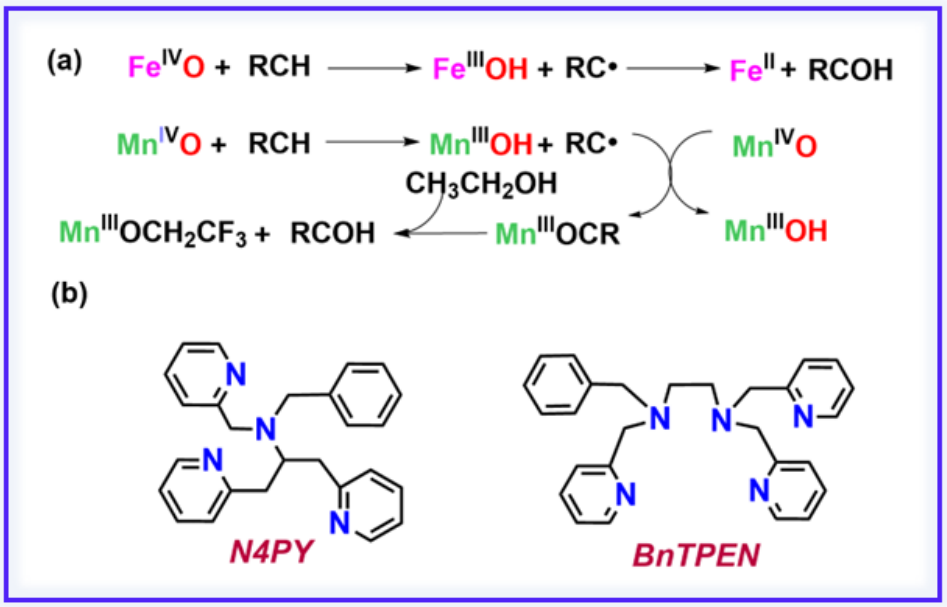

Scheme 1.2 (a) Rebound Fe(IV)O and Mn(IV)O hydroxylation mechanism (b) The ligands employed in this study (adapted from reference 99).

Some research has been dedicated to exploring the catalysis of chromium-oxo complexes.[100-101] In certain studies, ruthenium (Ru) has been the primary metal in biomimetic metal-oxo complexes.[102] Mayer and collaborators[103] showed that Ru(IV)O^{2+} oxidation of NADH analogs leads to selective HAT and hydride transfer in C–H oxidation. They established that the HAT pathway predominates over hydride transfer by noting a substantial KIE value of approximately 12 ± 1. A range of experimental studies has examined the mechanistic pathways involved in C–H activation catalyzed by Ru(IV)O complexes.[93,104,105] Comparative studies between experimental and theoretical investigations of Ru and Fe-oxo complexes have been conducted to assess their reactivity.[106]

We have now shifted our attention to exploring the contribution of equatorially coordinated ligand substitution concerning the reactivity pattern of Fe-oxo species, specifically examining how carboxylate-rich macrocycles impact their reactivity capabilities. McDonald *et al.*[107] synthesized the BuP2DA macrocycle by swapping the two pyridine groups of N4Py with

carboxylates, leading to carboxylate-bound complexes that show enhanced reactivity. Some research has emphasized the importance of adding heteroatoms to the equatorial framework of nonheme complexes. The reactivity pattern of Fe-centered oxo compounds is enhanced more by incorporating oxygen or sulfur donors, along with carboxylates, than by using nitrogen-based ligands..[108]

Que and colleagues[109] demonstrated that the reactivity pattern for the Fe=O unit is significantly increased when coordinated to a trans-carboxylate ligand when contrasted to a ligand having a neutral acetonitrile. This finding underscores the crucial role of heteroatom substitution, such as carboxylate, in regulating the reactivity pattern for the Fe=O species. According to Que and colleagues,[109] the addition of a trans-coordinated carboxylate ligand, rather than a neutral acetonitrile ligand, considerably amplifies the Fe-oxo moiety's reactivity pattern. This finding underscores the crucial role of heteroatom substitution, such as carboxylate, in altering the Fe-oxo species' reactivity trend. Table 1.1 consolidates the findings of these studies, detailing their structures, ligation modes, and the nature of the complexes.

Table 1.1: Summary of various metal-oxo complexes and their distinct properties.

Oxidants	Metal-atom	Nature of Study	References
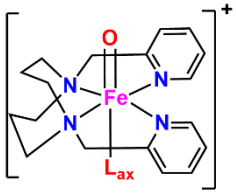 $[Fe^{IV}(O)(LPy_2)(L_{ax})]^+$	Iron (Fe)	Experimental + Computational	86

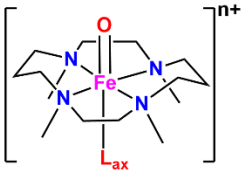 $[Fe^{IV}(O)(TMC)(L_{ax})]^{n+}$ L_{ax}=$NCCH_3$, CF_3COO^-, N_3, SR	Iron (Fe)	Experimental	87
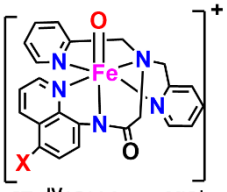 $[Fe^{IV}(O)(dpaq\text{-}X)]^{+}$	Iron(Fe)	Experimental	88
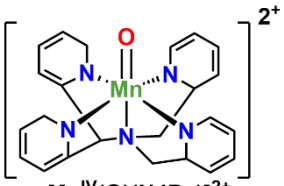 $Mn^{IV}(O)(N4Py)]^{2+}$	Manganese (Mn)	Experimental + Computational	95
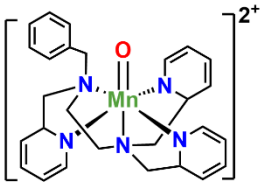 $Mn^{IV}(O)(BnTPEN)]^{2+}$	Manganese (Mn)	Experimental + Computational	98
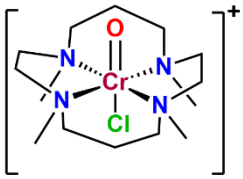 $[Cr^{IV}(O)(TMC)(Cl)]^{+}$	Chromium (Cr)	Experimental + Computational	101
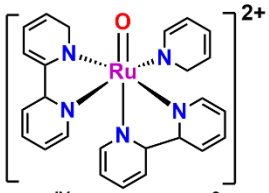 $[Ru^{IV}(O)(bpy)_2(py)]^{2+}$	Ruthenium (Ru)	Experimental	103

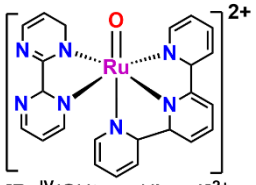 [$Ru^{IV}(O)(terpy)(bpm)]^{2+}$	Ruthenium (Ru)	Experimental + Computational	93
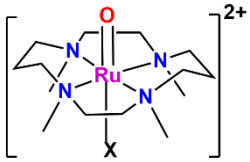 [$Ru^{IV}(O)(TMC)(X)]^{2+}$ X=$NCCH_3$, CF_3CO_2, N_3, SR	Ruthenium (Ru)	Experimental + Computational	106
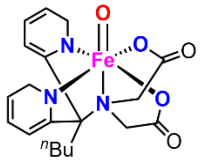 [$Fe^{IV}(O)(^n$Bu-P2DA)] ^{n}Bu=$-CH_2CH_2CH_2CH_3$	Iron (Fe)	Experimental	107
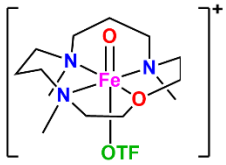 [$Fe^{IV}(O)(TMCO)(OTF)]^+$ OTF=trifluoromethane sulfonate anion	Iron (Fe)	Experimental	108
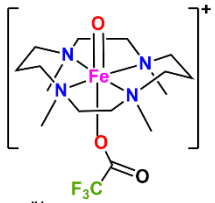 [$Fe^{IV}(O)(TMC)(O_2CCF_3)]^+$	Iron (Fe)	Experimental	109

1.4.5: Impact of Mediators on the Behavior of Fe-Oxo Complexes

Lately, redox mediators have drawn increased attention for their role as cocatalysts, especially for enhancing the trend of reactivity of M=O entity in activation reactions by C-H bonds. Redox activators like N-hydroxyphthalimide (NHPI) have demonstrated their ability to increase the efficiency of Fe(IV)-oxo complex-catalyzed C–H activation.[110-113] According to a study by

Barbieri *et al.*,[110] NHPI significantly enhances the C–H activation rate catalyzed by $[FeIV(O)(N4Py)]^{2+}$. As a catalyst, NHPI effectively oxidizes a wide range of organic compounds, such as aliphatic hydrocarbons, alkyl aromatic hydrocarbons, alcohols, amides, and amines.[114-116] The reaction generates the phthalimide-N-oxyl (PINO) radical, which is essential for hydrogen atom transfer (HAT) in the oxidation process. A follow-up study provided a kinetic analysis of HAT processes mainly driven by quinolinimide-N-oxyl radical (QINO).[117] The presence of QINO was found to enhance the HAT rate constants in a manner similar to PINO, stabilizing the transition state through enthalpic as well as polar effects, as shown in Scheme 1.3. Furthermore, NHQI was identified as a promising alternative to NHPI due to its lower C-H bond dissociation energy.

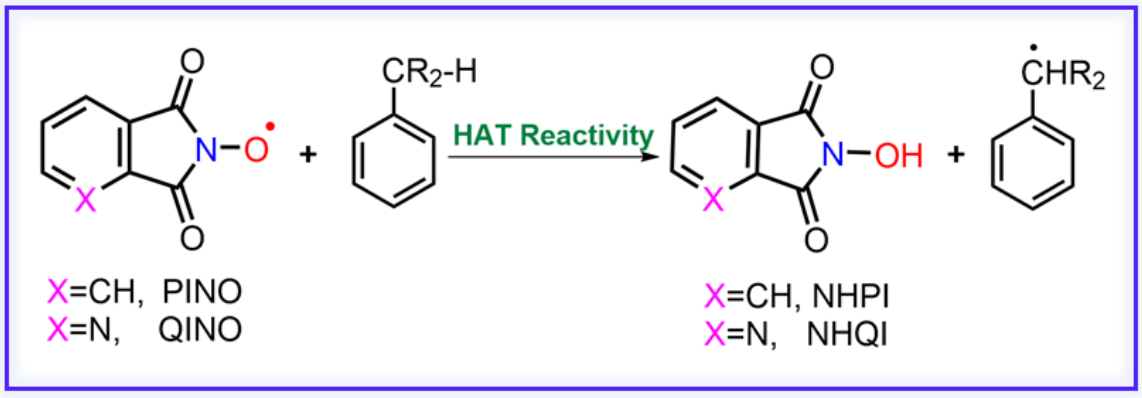

Scheme 1.3 HAT by PINO/QINO from an organic substrate (adapted from reference 117).

This mediator approach significantly broadens the scope of the metal-oxo entity in the C–H activation reactions, providing a promising avenue for enhancing the reactivity and selectivity of these catalytic processes.

CHAPTER 2

Computational Methodology

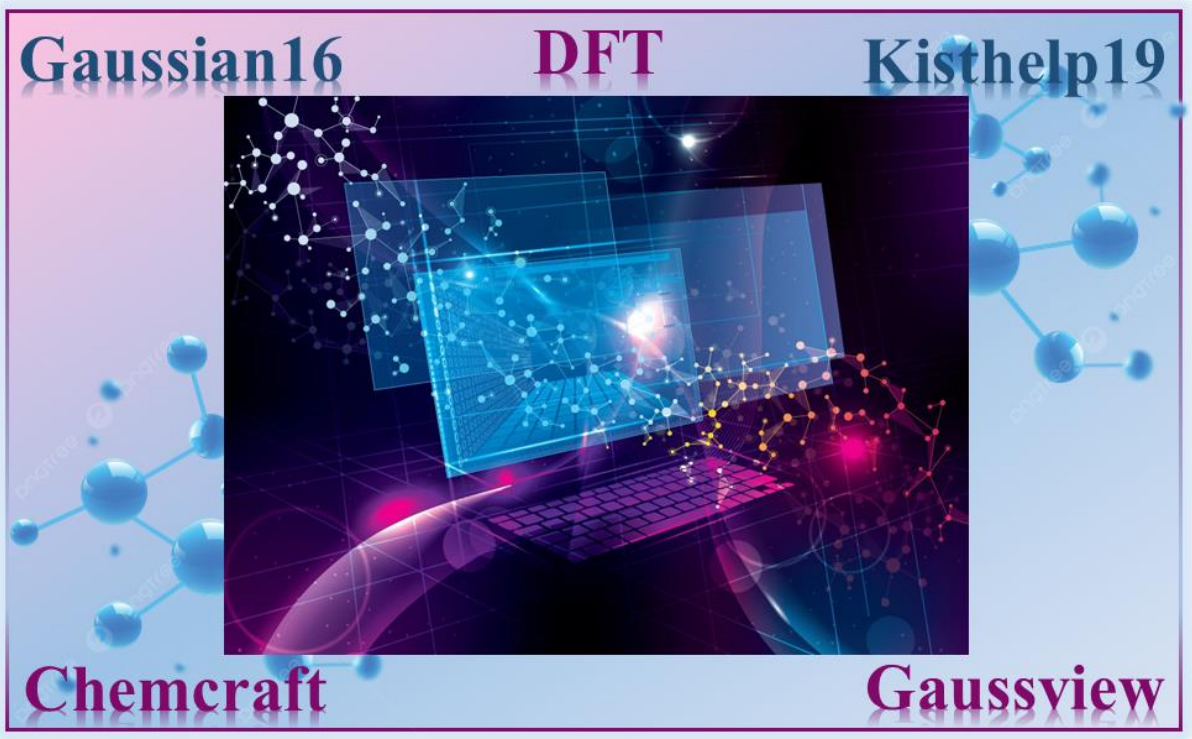

2.1: Computational Chemistry

A subfield of chemistry known as computational chemistry uses data systems and computational methods to solve challenging real-world chemical issues. It uses sophisticated mathematical techniques to make automation and computational implementation easier. This field lessens the need for conventional laboratory experiments by using advanced algorithms, mathematical models, and high-performance computational resources to predict molecular behavior, investigate reaction mechanisms, and create new materials and medications, as shown in Fig. 2.1.[1]

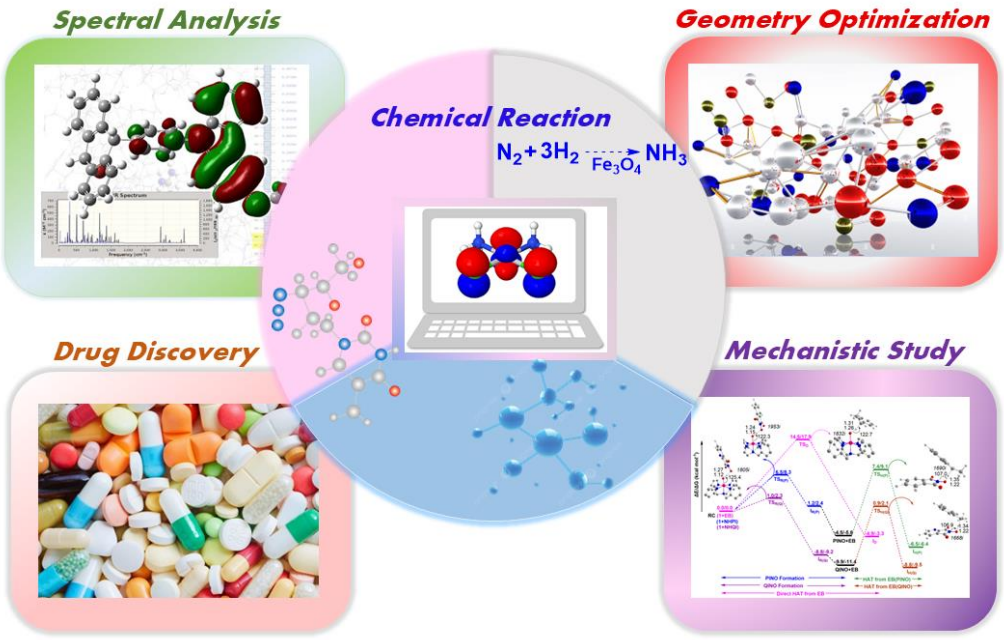

Fig. 2.1 Diverse applications of computational chemistry.

As an integral aspect of current scientific research, computational chemistry enables the study of intricate chemical systems with great precision, efficiency, and cost-effectiveness. The principles of quantum mechanics are fundamental to this area of study.[2] A wide range of literature offers detailed insights into these core ideas, with a selection of key points summarized here.[3-6]

2.2: Theoretical Details

This investigation relies on a computational technique rooted in QM, incorporating the findings from a prominent equation (Schrödinger Eq^{n}), which provides the system's energy, for analysis.[7-9]

The most straightforward way to present the aforementioned equation is:

$$\hat{H}\Psi = E\Psi \qquad \text{---------- Eq. 2.1}$$

Herein, this symbol representation: $\hat{H}$= the operator governing the Hamiltonian, whereas Ψ Is the symbol for the wave function, and E signifies the energy. This approach is suitable for the system containing solely 1 e^-; however, a system with multiple electrons cannot be exactly solved by it.[10] Accordingly, the subsequent approximations are considered for further analysis.

2.3: Distinct Methods of Approximations

2.3.1: The Born-Oppenheimer Approximation

Proposed in 1927,[11] this approximation relies on the notion that the electrons, traveling much faster than the nucleus, make it possible to treat them independently in molecules.[12] The logic behind this type of assumption is valid, as the nuclear mass, such as that of a hydrogen atom made up of a proton (single), is significantly more massive—approximately 1800 times—in terms of the electron's mass. Therefore, the e^-s navigate a field, produced by the nuclei in their stationary state, which imparts minimal kinetic energy.

It can be formulated as presented in Eq. 2.2.

$$\Psi_T = \Psi_e \Psi_n \text{ ---------- Eq. 2.2}$$

where "e" refers to the electronic component and "n" to the nuclear component.

2.3.2: The Hartree-Fock (HF) Approximation

As a central ab initio technique, approximates the electronic wavefunction, as designed by Ψ, and the energy associated with a molecular-based entity.[13]

It is hypothesized that each existing e^- resides within a field generated by the collective presence of the other e^-s, bypassing any direct interaction with them. Consequently, it models the multiple-electron-Ψ, as mentioned to be a Slater determinant constructed from the orbitals of individual electrons.[14]

This resulting mathematical expression is:

$$\hat{F}\phi_i(r) = \varepsilon_i\phi_i(r) \quad \text{---------- Eq. 2.3}$$

Here, $\hat{F}$, refers to the operator of Fock, $\phi_i(r)$, corresponds to the molecular orbitals, and ε_i symbolizes the energies of orbital.

Even though it is the reference point for the method (i.e., ab initio), lack of electron-electron correlation limits the precision of its outcomes, prompting the need for further investigation into other approaches.[15]

2.3.3: Post HF Approach

These methods, being more advanced, improve molecule-related computations, by resolving the drawbacks associated with the H-F approach, particularly its failure to account for e^--correlation, where e^- movements in pairs are interdependent in atomic or molecular species. The equation that describes this phenomenon is:

$$E_{cor} = E_T - E_{HF} \quad \text{---------- (Eq. 2.4)}$$

While this approach is more precise, it comes with higher costs, which are mitigated by the methods that follow.

2.3.4: Density Functional Theory (DFT)

Among the frequently applied methods for solving chemical problems is DFT. In this method, the electron density (ρ) is considered the primary variable rather than the wave function.[16] This would imply that DFT is not a quantum chemical method by not offering a coupled N-body wave function and relying on a non-interacting framework. The foundation of the theory rests on two essential theorems, as outlined below.

i) Hohenberg-Kohn Theorems

These core theorems provide the foundation for this approach. In line with this, the electron density in the ground state encodes mostly details concerning the potential external impact on the system, by extension, its Hamiltonian. Therefore, the wave function represents multiple e^- s and further ρ denotes to derive the detectable characteristics. It is stated as:

$$E_O = E_O[\rho] \quad \text{---------- (Eq. 2.5)}$$

Eo = Energy of the electron in its lowest state.

Additionally, the second theorem highlights that the correct electron density for the ground state reduces the functional at its minimum.

ii) Kohn-Sham Theorems

This theorem involves a non-interacting electron system that shares the same electron density in its G.S, as the interacting system in its original form, with simpler equations providing a practical route to solutions.[17] The central advantage of DFT is its efficient computational performance. Emphasizing the electron density instead of the many-body wave function, reduces the complexity and cost of calculations relative to traditional approaches.[18,19] In addition, it offers a solid compromise between precision and computational resources, which is why it has been adopted throughout this thesis.

2.4: Functionals

In the context of DFT, functionals are mathematical expressions that describe the relationship between the system's energy and ρ. These functionals are employed to estimate exchange-correlation-based energy, with different types designed to address various aspects of the correlation of electrons and their exchange interactions.[20] The predominant categories in use include:

2.4.1: Local Density Approximation (LDA)

LDA is a widely recognized and frequently employed approximation for more accurately describing the functional of exchange and correlation.[21] This assumes that the energy of exchange and correlation at a particular point is solely dependent on the electron density at that same location. It is frequently employed in scenarios where the ρ is approximately uniform.

2.4.2: Generalised Gradient Approximation (GGA)

GGA enhances the computation of the exchange-correlation functional by factoring in both the electron density (ρ) and its gradient, providing superior accuracy for systems with fluctuating electron density distributions.[22,23] Compared to LDA, these functionals tend to offer improved accuracy across a wider spectrum. Two well-known functionals in this category include the Becke (B) exchange functional[24] and the Lee-Yang-Parr (LYP) correlation functional.[25] While these functionals improve the description over LDA, they still face challenges in modelling dispersion interactions and systems where electron correlation plays a significant role.

2.4.3: Hybrid functionals

DFT calculations were carried out using three density functionals[26]:

1. **LSDA** (local spin density approximation): This uses the standard local exchange functional and the local correlation functional of Vosko, Wilk, and Nusair (VWN).[27]

2. **BLYP:** This combines the standard local exchange functional with the gradient correction of Becke and uses the Lee-Yang-Parr correlation functional (which also includes density gradient terms).[28]

3. **Becke3LYP:** This functional is a hybrid of exact (Hartree-Fock) exchange with local and gradient-corrected exchange and correlation terms, as first suggested by Becke.[24] (J. Chem. Phys. 1993, 98, 1372, 5648) The exchange-correlation functional proposed and tested by Becke was:

$$E_{XC} = (1-a_0)\, E_X^{LSDA} + a_0\, E_X^{HF} + a_x \Delta E_X^{B88} + E_C^{LSDA} + a_C \Delta E_C^{PW91}$$

Here ΔE_X^{B88} is Becke's gradient correction to the exchange functional, and ΔE_C^{PW91} is the Perdew-Wang gradient correction to the correlation functional. Becke suggested coefficients $a_0 = 0.2$, $a_X = 0.72$, and $a_C = 0.81$ based on fitting to heats of formation of small molecules. Only single-point energies were involved in the fit; no molecular geometries or frequencies were used.

B3LYP, a popular hybrid functional, consistently aligns well with experimental results in numerous cases.[29,30] This function has been particularly effective in modeling C-H activation reactions catalyzed by Fe-oxo entities,[31-33] especially with the TMC-ligated macrocycle.[34-36] Additionally, rigorous benchmarking studies show that B3LYP delivers superior performance compared to other functionals,[37] which is why it has been chosen for our investigations.

2.5: Basis Sets

It is a group of functions utilized to characterize molecular orbitals. These form the groundwork for expanding molecular orbitals and allow for the approximation of the wavefunction representing the electron.[38] The accuracy of a basis set increases as more basis functions are added, though this also escalates the computational cost. Achieving the right balance between

accuracy and computational effort is essential. In addition, it incorporates two different categories of orbitals, as illustrated below.

2.5.1: STOs

The outline of functions of radicals modelled after hydrogen atoms are precisely captured by STOs, which contain a factor of $e^{-\zeta r}$, with ζ signifying the nucleus's effective charge and r being the distance.[39,40] Every atomic orbital in a basis set is represented by a single STO or, alternatively, by a CGF. For instance, a single 1s function represents an H-atom, whereas a carbon atom requires five basis functions: 1s, 2s, and three 2p orbitals.

2.5.2: GTOs

It is described by a Gaussian function, $e^{-\zeta r^2}$.[41] While these functions decay in a Gaussian manner with increasing distance relative to the nucleus, this decay is less precise than the orbital type mentioned earlier.

As the orbital-type (slater) is more accurate in representing AOs, they are computationally expensive due to the complexity of integral molecules. While orbital-type (Gaussian), is being simpler computationally, albeit less precise. To improve accuracy, these are typically combined linearly to approximate STOs in QM computations.

2.5.3: Split Valence Basis Set

These are most commonly utilized, were formulated by Pople and his team. The name of each basis set encapsulates all important details, including the contraction scheme, the number of basis functions, and the number of primitive Gaussians.[42] A simple visual representation of this is outlined in Fig. 2.2 below.

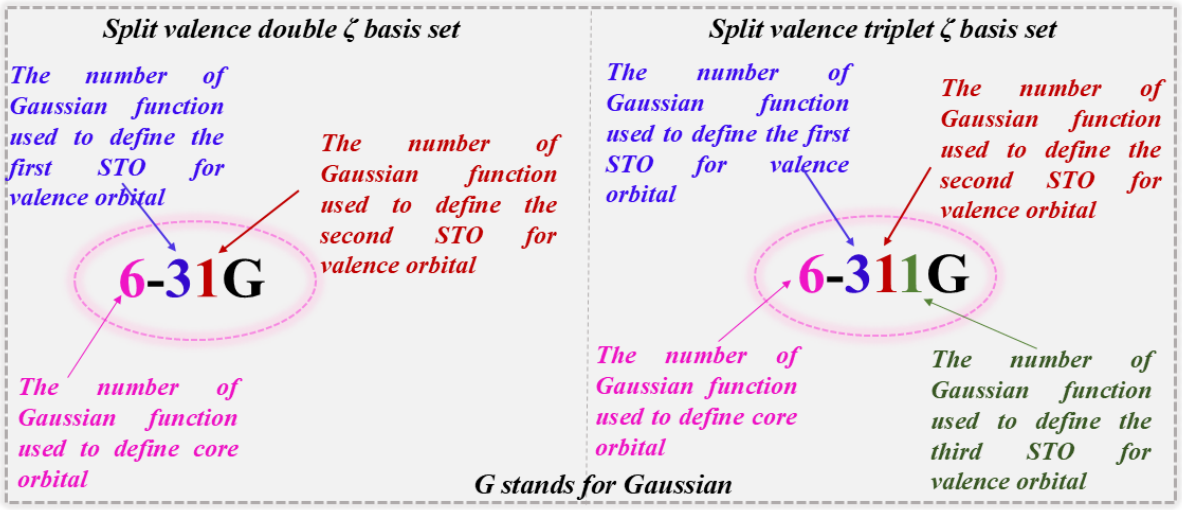

Fig. 2.2 General representation for split-valence basis sets.

2.6: Additional Functions

2.6.1: Polarisation Functions

The basis functions must be sufficiently adaptable because molecular orbitals, which are eigenfunctions of the Schrödinger equation involving several nuclei at different spatial locations, demand greater mathematical flexibility than atomic orbitals. To achieve this flexibility, AO-like GTOs are typically modified by incorporating these functions. The most commonly used such functions are d GTOs are commonly used for heavier elements, while p-type is utilized for H. Moreover, Pople and his colleagues developed a straightforward naming system to signify the inclusion of these functions, using the symbol * (pronounced "star").[43] For example, 6-31G* basis set implies a set of d-functions added to polarize the p-functions in 6-31G. Further, a 2nd star denotes the inclusion of p functions for hydrogen and helium, as seen in 6-311G**.

2.6.2: Diffuse Functions

E$^-$s in core orbitals, which participate in bonding, are generally more strongly attached to the nuclei. On the other hand, lone-pair e$^-$s are weaker bound and tend to be positioned further from the nuclei than bonding e$^-$s.[44,45] The "+" notation is frequently used for these functions.

For example, 6-31+G(d) refers to heavier atoms, extended by adding s as well as p functions with smaller exponents, further "+", in this context indicates the presence of diffuse s functions on H, as exemplified by 6-311++G(3df,2pd).

2.6.3: Basis Set Partitioning for Transition Metals and Main Group Elements

In this study, different basis sets were applied to main group and transition metal atoms to balance computational efficiency and accuracy.

For main group elements (e.g., H, C, N, O), a Pople-type all-electron basis set such as 6-31G or 6-311++G(d,p)* was used. These basis sets include polarization and diffuse functions as discussed above, ensuring a flexible and accurate description of electron distribution around lighter atoms.

For transition metals (Fe and Ru), relativistic effective core potential (ECP) basis sets were used to reduce computational cost and account for core-electron effects:

LANL2DZ (Los Alamos National Laboratory 2 Double-Zeta) was employed for Fe and Ru during geometry optimizations (B1 level). This basis set replaces the chemically inert core electrons with an ECP while explicitly treating the valence electrons.[46]

For single-point energy refinements (B2 level), we used the **SDD** (Stuttgart/Dresden) basis set and its associated ECP for transition metal atoms (Fe/Ru). The SDD includes scalar relativistic corrections and is designed for accurate treatment of transition metals.[47]

2.7: Solvation Models

Solution-phase processes, as opposed to the gaseous phase, position this model as a crucial element within the scope of this specialized area of chemistry.[48-50] These methods accurately simulate molecular behavior in solvent-dominated environments. Computational solvation can be approached through both explicit as well as implicit methods[51] (in Fig. 2.3).

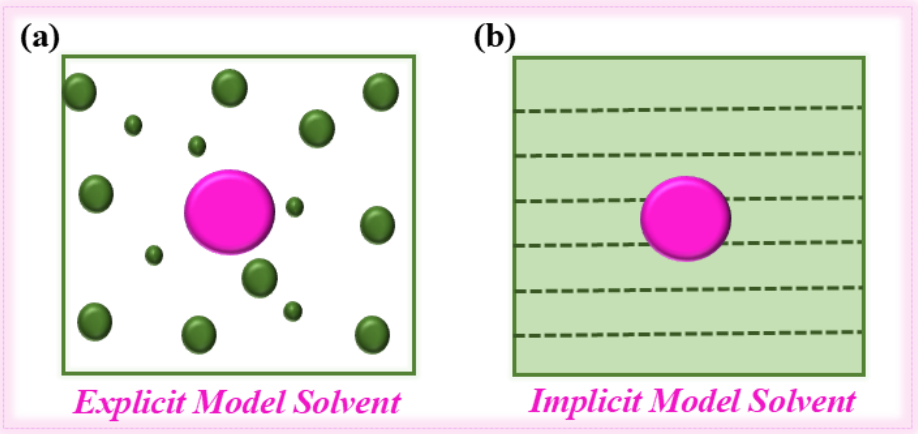

Fig. 2.3 Depiction of solvent models.

The process of explicit solvation refers to the process where solvent particles individually surround the solute, while it has been found that implicit solvation treats the solvent as a uniform, continuous entity, rather than discrete molecules.[52] These models are frequently employed alongside QM calculations and are less computationally intensive. SCRF models were employed in this thesis to facilitate the analysis of such studies.[53] The solute is contained within a cavity in CPCM, and a polarisable surface simulates the solvent's action.[54] SMD models solvation effects using empirical data based on the densities of the solute and solvent.[55]

2.8: Dispersion Corrections

Dispersion interactions (London forces) are critical for accurately describing non-covalent interactions,[56] especially in transition-metal complexes and supramolecular systems. However, standard DFT functionals generally fail to capture these non-local effects.

To overcome this, empirical dispersion corrections such as Grimme's D3(BJ)[57] have been developed. This correction was employed in this work to improve the reliability of computed energies and geometries, particularly for systems involving weak interactions.

2.8.1: Grimme's D3(BJ) Dispersion Correction

The D3(BJ) model is a third-generation dispersion correction that adds atom-pairwise dispersion terms to the DFT energy. It uses Becke–Johnson damping to avoid overestimating dispersion at short interatomic distances.

The dispersion energy is given by:

$$E_{disp}^{D3(BJ)} = - \Sigma_{i<j} \left[C_{6,ij}/R_{ij}^{6} + f_{damp,6,}(R_{ij}) + C_{8,ij}/R_{ij}^{8} + f_{damp,8}(R_{ij}) \right]$$

Where:

- $C_{6,ij}$ and $C_{8,ij}$ are environment-dependent dispersion coefficients,
- R_{ij} is the interatomic distance,
- f_{damp} is the Becke–Johnson damping function.

D3(BJ) is computationally efficient and tailored to specific functionals (e.g., B3LYP), offering enhanced accuracy in modelling non-covalent interactions. It has been widely validated and is especially effective in systems with significant weak or long-range interactions.

2.9: Quantum Mechanical Tunneling (QMT) and Kinetic Isotope Effect (KIE)

In the domain of quantum mechanics, particles such as protons or atoms like hydrogen can penetrate potential barriers that would be inaccessible according to classical energy constraints. Arising from the wave nature of particles, this phenomenon enables them to behave probabilistically rather than adhering to fixed trajectories. Therefore, particles can "pass through" energy walls, evading the classical prerequisite to have enough KE, leading to break through the constraint.[58-60] Referred to as tunneling, this quantum mechanical effect (illustrated in Fig. 2.4), enables particles to cross barriers that the classical approach would prevent them from crossing.

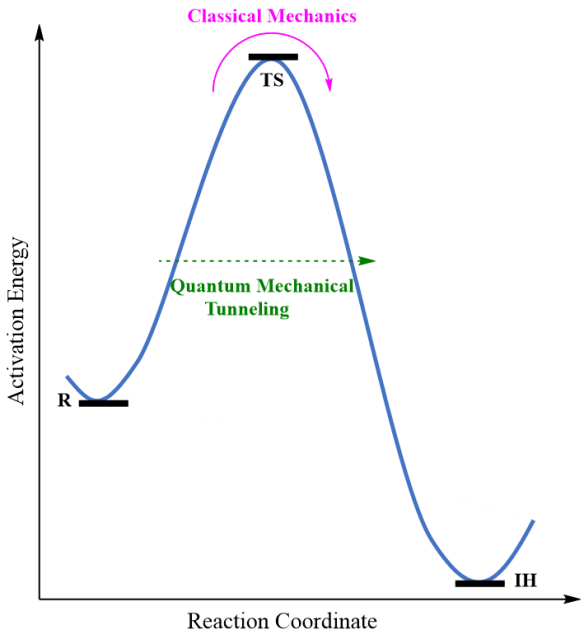

Fig. 2.4 Classical representation of tunneling, where R, TS, and IH represent Reactant, Transition State and Intermediate along the reaction coordinate.

Consistent with this phenomenon, the rate constants are calculated using the approach outlined in Eyring's transition state theory (Eq. 2.6).

$$k = \kappa\sigma \frac{k_b T}{h} \exp\left(-\frac{\Delta G^{\ddagger}}{RT}\right) \qquad \text{---------- Eq. 2.6}$$

Here, κ and σ stand for the transmission coefficient and reaction symmetry, respectively. A one-dimensional (1-D) asymmetric Eckart approach, commonly used for H-transfer or migration processes, is employed to assess tunneling.[61] The equation below determines how the transmission coefficient affects the activation barrier.

$$\Delta\Delta E^{\ddagger}_{tun} = -\,RT \ln \kappa\,(T) \qquad \text{---------- Eq. 2.7}$$

This equation represents the quantitative reduction of activation energy resulting from tunneling ($\Delta\Delta E^{\ddagger}_{tun}$), where κ(T) is the temperature-dependent transmission coefficient, R is the universal gas constant, and T is the absolute temperature.

To confirm quantum mechanical tunneling, the KIEs of all reactions are determined. The KIE computations used the frequency of stationary states and their deuterium-replaced counterparts, calculated after tunneling influence using equation 2.8.

$$KIE_{TC} = (\kappa_H / \kappa_D).\ KIE_{EY} \quad \text{------- Eq. 2.8}$$

The transmission coefficients of hydrogen are symbolized by κ_H while its deuterated isotopomers are represented by κ_D. The tunneling contribution for a reaction is contributed using the following Eq. 2.9:

$$\%\ \text{tunneling} = 100[(\kappa_{Eckart} - 1)/ \kappa_{Eckart}] \text{ ------- Eq. 2.9}$$

Here, κ_{Eckart} denotes the transmission coefficient using the Eckart method. Consequently, the numerator in Equation 2.8 reflects the difference between a reaction that includes tunneling and one where the transmission coefficient is unity, $\kappa = 1$, indicating no tunneling effect. Therefore, the ratio $[\kappa_{Eckart} - 1)/ \kappa_{Eckart}]$ quantifies the extent of tunneling contribution.

2.10: Tools

Advancements in software technology and the increasing availability of tools have generated significant interest in this field of chemistry. The selection of these tools is influenced by factors such as cost, features, ease of use, and processing speed. In the studies presented here, key steps like geometry optimization, frequency calculations, and thermochemical analysis are carried out using Gaussian 16 software.[62] It utilizes DFT methods to conduct various electronic structure analyses. To render images, display results, and facilitate analysis, the GaussView[63] and Chemcraft[64] software were employed. Similar computational analyses can also be carried out using other software packages, including GAMESS, ORCA, TURBOMOLE, and others. Each tool comes with its specific set of features and functionalities, while Kisthelp software

was applied to investigate tunneling.[65] A concise summary of these tools can be found in Fig. 2.5 below.

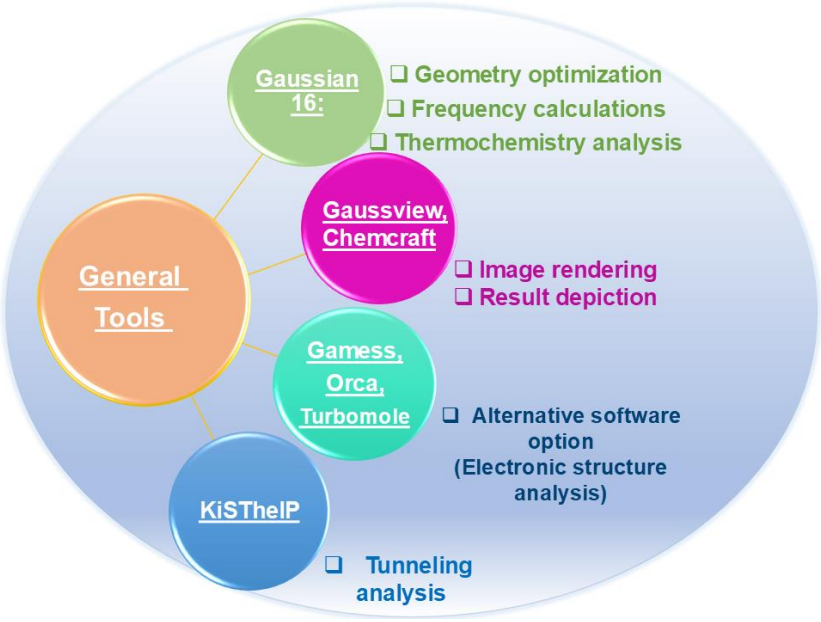

Fig. 2.5 An Overview of the computational tools applied throughout the research.

CHAPTER 3

Effect of Substituent on C-H Activation Catalysed by a Nonheme Fe(IV)O Complex: A Computational Investigation of Reactivity and Hydrogen Tunneling

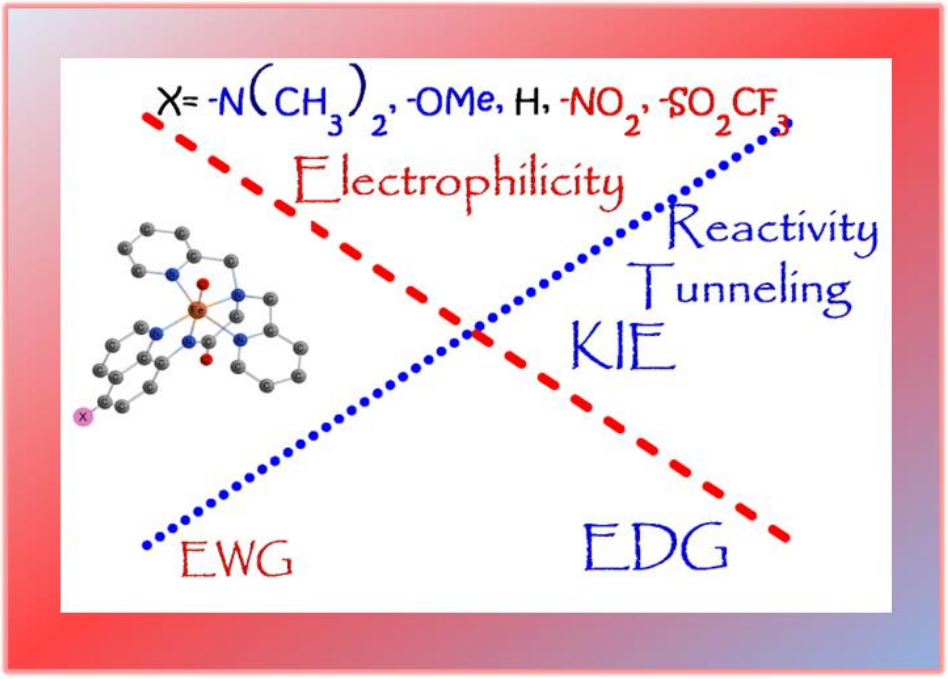

3.1: Introduction

Synthetic iron(IV)oxo complexes serve as bio-inspired models for active mononuclear nonheme iron enzymes which are now one of the prime interests in bioinorganic chemistry due to their roles in critical metabolic processes, toxin neutralization, DNA repair, etc.[1-5] These complexes have also been found to be very effective in the chemistry of C-H bond activation/functionalization.[6-9] Because of the close interrelations of various reactivity factors e.g., the axial or equatorial ligand connectivity to central metal,[10,11] general ligand architecture,[12,13] energy of the acceptor orbital,[14,15] spin state (which leads to a single-state, two-state or multi-state reactivity),[15-17] quantum mechanical tunneling, etc.,[15,18,19] that can all play vital roles, characterizing and comprehending the reactivity patterns of these bond-activation processes is extremely difficult.

High-valent metal oxo chemistry, specifically Fe(IV)O, is extremely rich due to its effectiveness in catalysis and for allowing significant mechanistic insights into the reactivity. The seemingly never-ending journey into investigating this chemistry was started through the synthesis of $[Fe^{IV}(O)(TMC)(L_{ax})]^{n+}$ complexes[20,21] and is still continuing today with full enthusiasm.[2,3,5,22-27] Other than iron-oxo several other metal-oxo complexes e.g., Mn, Co, Cr, and Ru have also been found to be efficient catalysts.[28-32] A few high-valent metal-nitrido complexes have also been reported along with the oxo complexes.[33]

A few particular remarkable theoretical perceptions were developed to enlighten the insights into the C-H activation reactivity of these complexes. Among others, the most promising one is the two-state reactivity (TSR).[34] In TSR, the excited high spin state surface in the reactant crosses the low spin ground state surface towards the transition state. The driving force behind this phenomenon is the exchange-enhanced reactivity (EER), which implies that the greater number of unpaired electrons in the transition states and intermediates provides extra stability, which is considered as the Hund's rule analogue in bioinorganic chemistry.[35,36]

The TSR concept is able to explain plenty of observed reactivity patterns.[15,18,19,37,38] This is also found useful in various cases other than iron-oxo.[39,40]

TSR can be explicitly verified by comparing the observed and calculated kinetic isotope effects (KIEs). In the C-H activation mechanism, the first H-abstraction step is considered as the rate-determining step. Consequently, H/D KIE can work as a sensitive spin state probe as it will depend on the spin state pathway.[15,16,18,19,38]

The C-H activation catalysed by Fe(IV)O complexes follows a one-electron transfer mechanism and it can be presented using a very simplistic push-pull diagram (Fig. 3.1).

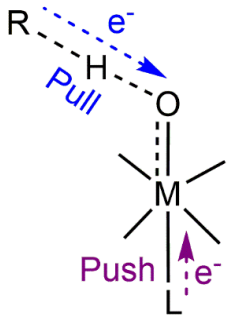

Fig 3.1 Schematic diagram of the 'push-pull' effect on the H-abstraction mechanism by metal-oxo complexes.

The electrophilicity of the central metal depends on the amount of electron density shifting from the ligands. In the classical sense, the reaction should follow an electrophilic trend, i.e., the more electron-deficient metals in the complex should be more reactive, as has been observed in some investigations.[41]

However in a few cases, opposite type of reactivity pattern was observed, e.g., an investigation performed by Sastri *et.al.,* with a series of $[Fe^{IV}(O)(TMC)(L_{ax})]^{n+}$ complexes, where L_{ax} is different axial ligands (Scheme 3.1a) established anti-electrophilicity controlled hydrogen-atom transfer.[10]

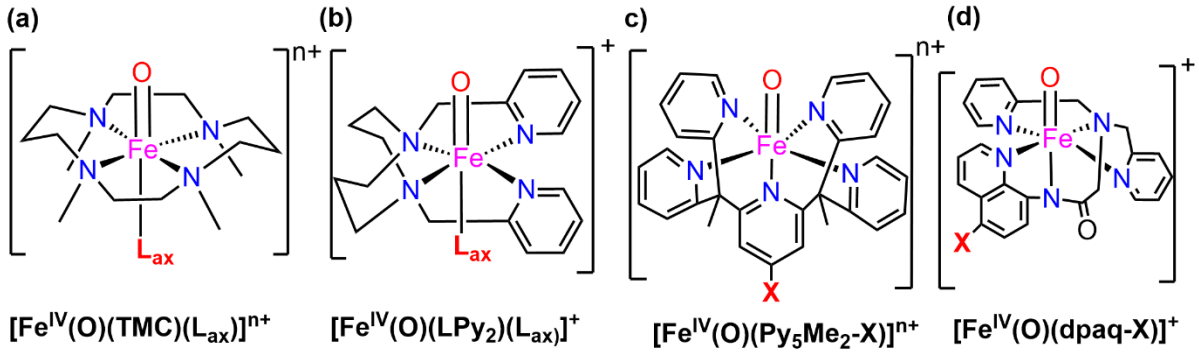

Scheme 3.1 A few reported iron-based complexes with ligand/substituent tuning for C-H activation: (a) $[Fe^{IV}(O)(TMC)(L_{ax})]^{n+}$, (b) $[Fe^{IV}(O)(LPy_2)(L_{ax})]^{2+}$, (c) $[Fe^{IV}(O)(Py_5Me_2\text{-}X)]^{n+}$ and (d) $[Fe^{IV}(O)(dpaq\text{-}X)]^{+}$. L_{ax} and L represent various axial ligands to the Fe and different substituents, respectively.

In a complementary theoretical investigation, it was found that the reason behind the anti-electrophilic reactivity was quantum mechanical tunneling, which increased with the presence of more electron-releasing groups.[10,15] Several other efforts were also focused on trying to understand the effect of electron tuning by different substitutions to the macrocyclic ligand that is indirectly connected to the central metal atom.[27,42] Que and co-workers[43] reported an investigation that included a series of $[Fe^{IV}(O)(LPy_2)(L_{ax})]^{2+}$ (Scheme 3.1b) complexes, where L_{ax} represented differently substitutions at the 4-position of axial pyridine of N-oxide ligands. In this case, the hydrogen atom transfer (HAT) rates were also accelerated with more electron-donating ligands, like $[Fe^{IV}(O)(TMC)(L_{ax})]^{n+}$ complexes.[10] Chang and co-workers[44] reported a series of Fe(IV)O complexes (Scheme 3.1c), with a penta-pyridine macrocyclic ligand substituted at the para-position of a pyridine axial ligand. In contrast to the aforementioned pattern, here the electrophilic reactivity pattern was observed, i.e., electron-poor ligands showed faster rates compared to their electron-rich ligands. Hitomi *et al.,*[45] also synthesized a $[Fe^{IV}(O)(dpaq\text{-}X)]^{+}$ complex, where dpaq was a macrocycle with monoamido ligation (Scheme 3.1d) which was found to be more reactive than the popularly investigated iron-oxo complexes, e.g., $[Fe^{IV}(O)(N4Py)]^{2+}$ complex.[46]

In this article, our focus is dedicated to establishing the mechanism of hydrogen-atom abstraction catalyzed by a series of nonheme $[Fe^{IV}(O)(dpaq\text{-}X)]^{+}$ complexes formed by variable substitution at the 5 position of the quinoline ring of dpaq, which represents 2-[bis(pyridine-2-yl-methyl)]amino-N-quinolin-8-yl-acetamido, and where X is a substituent group at the 5-position of a quinoline moiety in the parent ligand dpaq-H. Both electron-donating groups (EDGs) e.g., ($-N(CH_3)_2$, -OMe), and electron-withdrawing groups (EWGs) e.g., ($-NO_2$, $-SO_2CF_3$), were used as substituents other than the unsubstituted parent compound. Quantum mechanical tunneling is now believed to be the third reactivity-controlling factor.[47,48] So, the presence of quantum mechanical tunneling and its variation with an electron-donating tendency of the substituents were also investigated here to verify the anti-electrophilic tunneling as well as the reactivity proposition reported earlier.[15] Tunneling corrected KIEs were calculated and compared with experiments to determine the spin state reactivity. The percentage tunneling contributions towards the total reactions were also calculated.

The reactivity of the parent compound was also compared with other popular non-heme Fe(IV)O compounds. The investigated reactions are presented in the following Scheme 3.2.

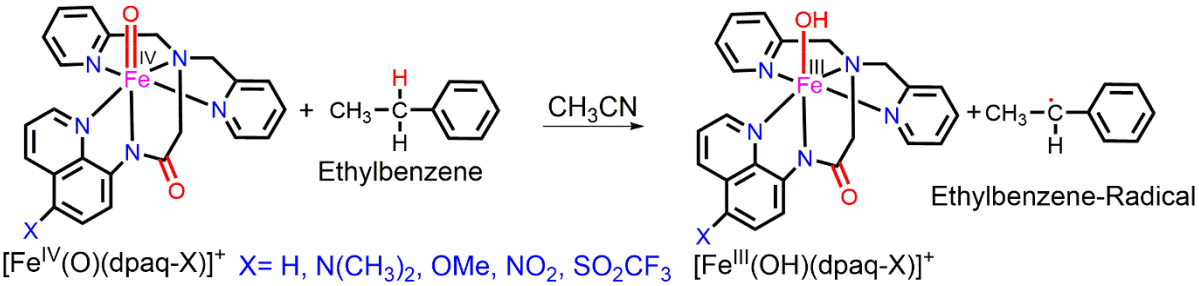

Scheme 3.2 Schematic representation of the hydrogen-abstraction from ethylbenzene by a series of $[Fe^{IV}(O)(dpaq\text{-}X)]^{+}$ complexes, with CH_3CN used as a solvent.

In the following discussion, the compound's names will be mentioned by their group of substitution, e.g., OMe, NO_2, etc., and H for the parent compound. A general substrate ethylbenzene (EB) is used for all reactions.

3.2: Computational Details

All the computations related to geometry optimization, frequency, and thermochemistry were performed using DFT-B3LYP methods. B3LYP is a function developed by Lee-Yang-Parr[49,50] that is quite frequently used in organometallics, especially in the case of FeO complexes.[15,18,51] The LANL2DZ basis set[52] with its electrostatic potential was used for Fe and Pople's split valence double zeta 6-31G** basis set[53] was used for all the atoms. The ClO_4^- counter ion was also used to neutralize the charge of the system to overcome the self-interaction error in DFT.[54] The geometry was also optimized in the presence of implicit acetonitrile solvent using the self-consistent reaction field (SCRF)[55] procedure with Truhlar's solvation model density approximation (SMD).[56] This level of theory is represented here as B1.

The transition states were verified from the frequency calculations. Local minima corresponded to no imaginary frequency whereas transition states corresponded to one imaginary frequency. Thermal and entropic corrections to the Gibbs free energy at T = 298 K were made. The energies were further refined at the higher basis 6-311++G(d,p) for all atoms, and for Fe, SDD with its ECP was used.[57] This level of theory is counted as B2. The Gaussian 16 program package was used for all computations mentioned above.[58]

The accurate identification of the electronic state was determined using spin densities, mulliken charges, and natural spin orbitals. For result analysis, visualization, and drawing images Chemcraft software has been used.[59] Mainly zero-point corrected energy at the B2 level was used for further discussion unless otherwise mentioned.

3.3: Tunneling Corrections and Kinetic Isotope Effect (KIE) Calculations

The rate constants calculations were performed using Eyring's transition state theory (Eq. 3.1) approach.[60]

$$k = \kappa\sigma \frac{k_b T}{h} \exp\left(-\frac{\Delta G^{\ddagger}}{RT}\right) \qquad \text{Eq. 3.1}$$

Where, κ and σ imply the transmission coefficient and reaction symmetry, respectively. The

quantum mechanical tunneling factor, i.e., transmission coefficients, were computed using one--dimensional asymmetric Eckart Method,[61] which has been successfully used in several H-transfer/migration processes.[15,18,19,62-64] This method used the ZPE-corrected energy of the reactant, transition states, and products along with the imaginary frequency, which builds up the mass-weighted intrinsic reaction coordinate (IRC).[65,66] The transmission coefficient's influence on the barrier was computed using the following Eq 3.2:

$$\Delta\Delta E^{\ddagger}_{tun} = -RT \ln \kappa (T) \qquad \text{Eq…3.2}$$

Where R is the universal gas constant, T is the absolute temperature, and $\Delta\Delta E^{\ddagger}_{tun}$ implies the quantitative reduction of a barrier of activation due to the tunneling.

To validate the presence of the tunneling factor, kinetic isotopic effects (KIEs) for all the compounds were also computed. The frequency of the stationary states belonged to the reaction between Fe(IV)O complexes with EB and its deuterium substituted equivalents were used in the KIE calculations, which were calculated after incorporation of the contribution of tunneling using the following Eq 3.3:

$$KIE_{TC} = (\kappa_H / \kappa_D).\ KIE_{EY} \qquad \text{Eq……3.3}$$

where κ_H and κ_D are the transmission coefficients of hydrogen and its deuterated isotopomers. The Wigner method has also been used to find and compare the tunneling effect.[67] But this method expressively provides low values of tunneling. All the kinetics and tunneling were computed using the kisthelp2019 program.[68]

3.4: Result and Discussion

3.4.1: Spin-State Preference and Two-State Reactivity (TSR)

Fe(IV)O complexes may possess two close-lying spin states, namely *S*=1(two unpaired electrons) and *S*=2 (four unpaired electrons). Here, we observed the same Table 3.1, with *S*=1 as the ground state and *S*=2 as a very close-lying excited state.

Table 3.1 The relative energies (in kcal mol^{-1}) for all the investigated reactions computed at

different level of theory.

Reactions	Spin state	Species	B1+ZPE	B2+ZPE	B2+G^{corr}(298K)
H	*S*=1	^{3}R+S	0.0	0.0	0.0
		^{3}TS	17.3	14.6	26.9
		^{3}I	-0.2	-5.3	4.2
	S=2	^{5}R+S	5.8	1.7	-0.01
		^{5}TS	21.1	10.6	18.6
		^{5}I	5.4	-9.3	-2.3
$N(CH3)_2$	*S*=1	^{3}R+S	0.0	0.0	0.0
		^{3}TS	17.3	14.7	26.7
		^{3}I	-0.2	-5.1	4.1
	S=2	^{5}R+S	5.4	1.5	-0.6
		^{5}TS	21.0	10.7	19.1
		^{5}I	5.0	-8.8	-3.3
NO_2	*S*=1	^{3}R+S	0.0	0.0	0.0
		^{3}TS	16.5	13.8	25.4
		^{3}I	-0.6	-5.6	3.2
	S=2	^{5}R+S	6.6	2.4	0.6
		^{5}TS	19.3	10.3	18.5
		^{5}I	6.6	-8.8	-1.8
OME	*S*=1	^{3}R+S	0.0	0.0	0.0
		^{3}TS	17.3	14.7	26.7
		^{3}I	-0.4	-5.2	3.9
	S=2	^{5}R+S	5.5	1.6	-0.2
		^{5}TS	20.9	10.6	18.8
		^{5}I	6.6	-7.7	-0.7
SO_2CF_3	*S*=1	^{3}R+S	0.0	0.0	0.0
		^{3}TS	16.5	13.9	26.1
		^{3}I	-0.8	-5.3	4.3
	S=2	^{5}R+S	6.4	2.7	1.3
		^{5}TS	20.5	10.6	18.6
		^{5}I	6.5	-7.8	0.3
N4PY	*S*=1	^{3}R+S	0.0	0.0	0.0
		^{3}TS	16.5	13.9	26.1
		^{3}I	-0.5	-5.5	3.2
	S=2	^{5}R+S	10.4	5.4	3.3
		^{5}TS	20.2	11.3	18.7
		^{5}I	4.5	-9.7	-2.7

The ΔE_{TQ} for H is 1.7 kcal mol^{-1}, which was slightly increased in the case of electron-

withdrawing substituent ~2.4-2.7 (NO_2 and SO_2CF_3) and was found to be almost constant for electron-donating substances ($N(CH_3)_2$ and OMe). As ΔE_{TQ} was found to be similar, even smaller, compared to the other Fe(IV)O complexes showing two-state reactivity (TSR),[38] these complexes also might exhibit the same. Therefore, we computed both the *S*=1 and *S*=2 pathways. The geometries of the oxidants were almost unaffected by these substitutions as presented in Fig. 3.2.

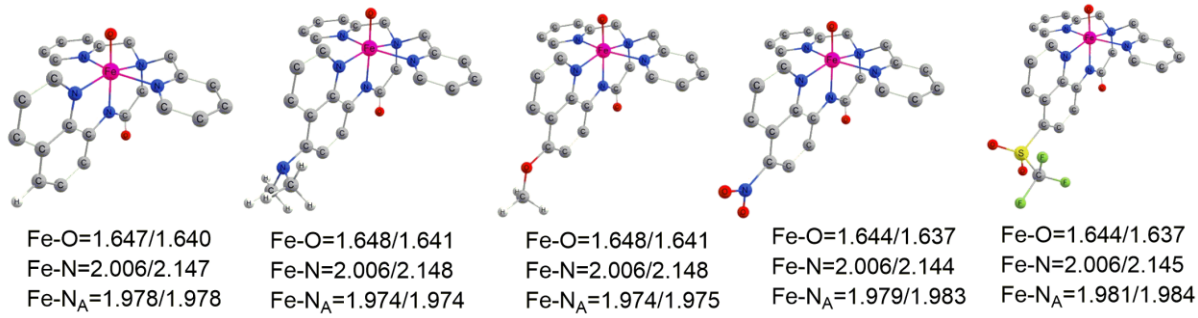

Fig. 3.2 Optimized geometries of the oxidants with key geometrical parameters computed at B1 level of theory (distances are in Å and angles are in degree).

3.4.2: Electron Shifting Diagram

This was a one-electron transfer process from the substrate to the oxidant, with the spin of the shifting electron and the acceptor orbital of the oxidant depending on the spin state pathways. An electron shifting diagram is presented in Fig. 3.3.

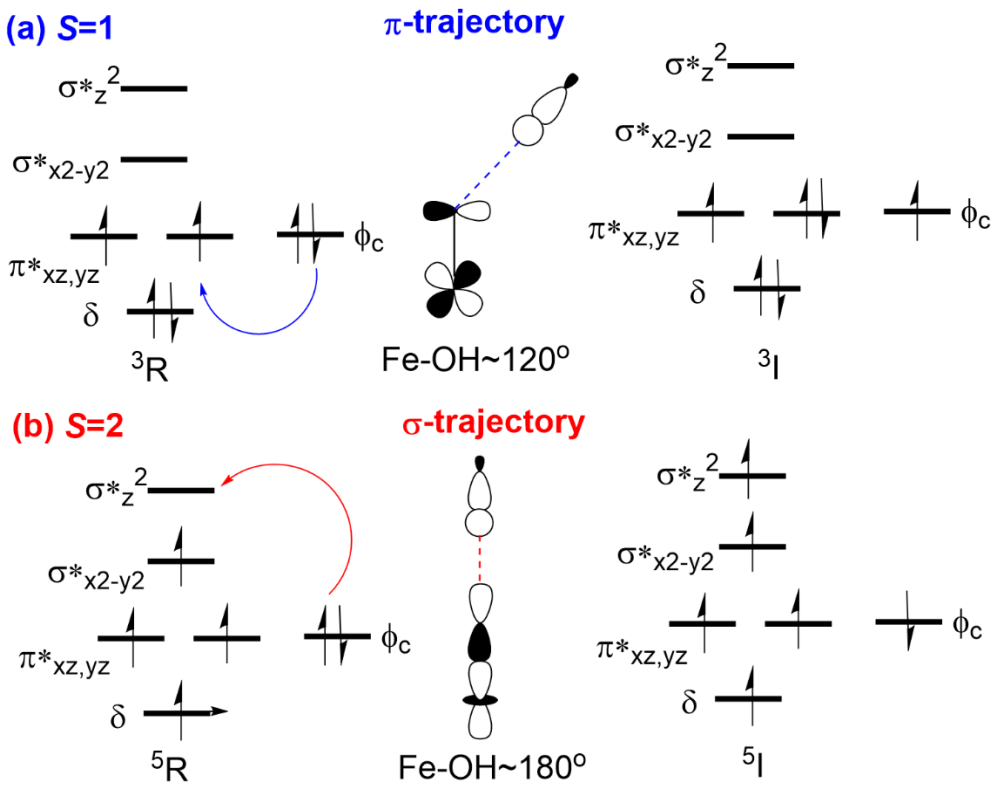

Fig. 3.3 Electron shifting diagram for HAT: the upper panel represents *S*=1 and the lower panel represents *S*=2 state.

It was shown that in the *S*=1 path, a β electron transfer to the π anti-bonding orbital took place, which promotes the H-transfer through a π trajectory with the ~FeOH angle of ~120°, while if it follows the *S*=2 path, then α electron shifts to the $\sigma^*_{z^2}$ orbital through σ trajectory with FeOH angle ~180°.

Here the quintet transition state was found to be lower in energy than the triplet transition state, due to the favourable increase in exchange interactions (due to higher number of unpaired electrons in the *S*=2 transition state compared to *S*=1) on the quintet energy surface throughout the reaction, which was a manifestation of the exchange-enhanced reactivity (EER) concept.[35] Consequently, as the reaction proceeds, the quintet surface (initially the excited state) crosses the triplet surface (initially the ground state) and produces a more stable triplet intermediate.

3.4.3: Electrophilicity

Classically, electron transfer should be favoured with the electrophilicity of the central metal

atom, which can be further influenced by the EDG/EWG substitution. The energy of the $\sigma^*_{Z^2}$ acceptor orbital in the *S*=2 state, i.e., the LUMO orbital energy poor proxy for the electrophilicity. An expected qualitative picture can be obtained from Fig. 3.4, i.e., with EDG substituent, the energies of the LUMO increased (-5.36 eV for $N(CH_3)_2$ and -5.39 eV for OMe), whereas it decreased for EWG substituent (-5.96 eV for NO_2 and -5.98 eV for SO_2CF_3) compared to the unsubstituted parent compound (-5.56 eV for H).

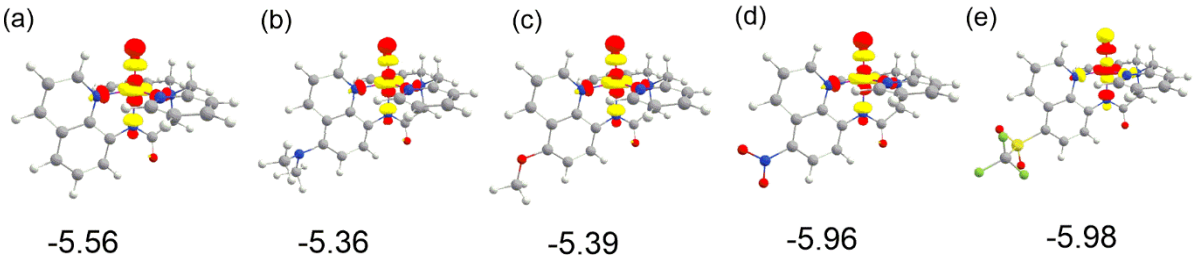

Fig. 3.4 Shapes of the lowest unoccupied molecular orbital (electron acceptor orbital in *S*=2) (a) H, (b) $–N(CH_3)_2$, (c) OMe, (d) NO_2 and (e) SO_2CF_3. The energies are given in electron volts (eV).

However, this electrophilicity did not affect the reactivity much, as reflected by the classical energy of activation presented in Fig. 3.5.

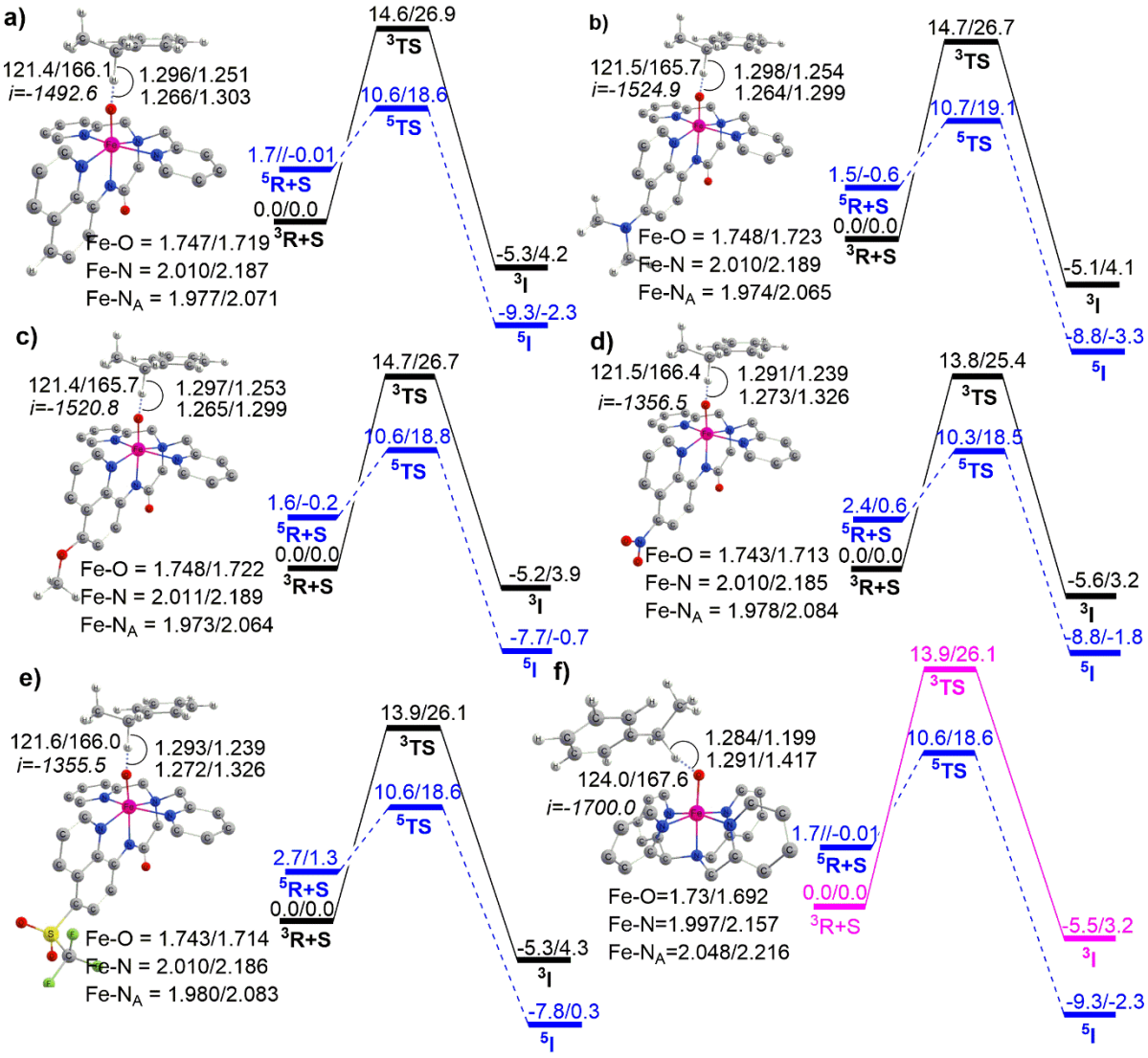

Fig. 3.5 Potential energy profiles for HAT from EB catalysed by Fe(IV)O complexes, where a) X=H, b) X=N(CH$_3$)$_2$, c) X=OMe, d) X= NO$_2$ and e) X=SO$_2$CF$_3$. The profiles were drawn with respect to the separated reactant, and energies are presented in kcal mol^{-1} in B2+ZPE/B2+G$^{corr}_{298K}$ format. The *S*=2 state TS geometry and imaginary frequencies along with the parameters for both *S*=2 and *S*=1, are given here. In Fig. 3.5f blue line is for the *S*=2 path of [Fe^{IV}(O)(dpaq-X)]$^+$ and the pink line is for the *S*=1 state of the [Fe^{IV}(O)(N4Py)]$^{2+}$ complex.

The barrier of activation for all compounds was within ±0.3 kcal mol^{-1}, which could be counted as being within the error limit of DFT. In the case of free energy barriers also, this ranged within

±0.6 kcal mol^{-1}.

Next, we attempted to find out the presence and implications of quantum mechanical tunneling. All the computed tunneling-related parameters are summarized in Table 3.2.

Table 3.2 Imaginary frequencies of the transition states ($\nu^{\ddagger}_{H}$), transmission coefficients for H (κ_H) and D (κ_D), kinetic isotope effect at 298K, tunneling correction values ($\Delta\Delta E^{\ddagger}_{tun}$, in kcal mol^{-1}) at 298 K and tunneling corrected barrier (ΔE-$\Delta\Delta E^{\ddagger}_{tun}$, in kcal mol^{-1})) at the B2+ZPE level and the tunneling contribution (%tunneling) of the overall reaction for H-abstraction from EB.

Reactions	$\nu^{\ddagger}_{H}$	κ_H	κ_D	KIE_{Eck} (298K)	$\Delta\Delta E^{\ddagger}_{tun}$	ΔE-$\Delta\Delta E^{\ddagger}_{tun}$	%tunneling
H	1493	20.8	5.2	22.0 (68.8)**(32)***	1.8	8.8	95.4
$N(CH_3)_2$	1525	25.0	5.7	23.5 (71.2)	1.9	8.8	96.0
OMe	1521	23.7	5.6	22.6 (70.6)	1.9	8.7	95.8
NO_2	1357	10.1	3.8	13.3 (55.2)	1.4	10.2	90.0
SO_2CF_3	1356	10.4	3.8	13.7 (56.5)	1.4	9.9	90.4

* Experimental value at 298K

It is stimulating to appreciate that quantum mechanical tunneling is influenced by the substituent. The value of transmission coefficients (κ_H) for the $N(CH_3)_2$ (25.0) and OMe (23.7) increases compared to the base compounds (20.8). Whereas for electron-withdrawing substituents, it significantly decreases, e.g. for NO_2 and SO_2CF_3 the values of κ_H were 10.1 and 10.4, respectively. Therefore, the anti-electrophilic tunneling trend was followed at this point. This can be comprehended by looking at the trend of imaginary frequencies of the transition states, which reduced for EWGs and increased for EDGs. The quantum mechanical tunneling is a path function and the imaginary frequencies control the reaction potential energy surface (PES). The higher the imaginary frequencies, the sharper PES becomes, i.e., H has to pass a lesser distance, which makes tunneling more favourable.[15] The narrowness of the PES occurs due to the electrostatic contribution created by the more EDG substituents.[38] To get further insight into the tunneling, we plotted in Fig. 3.6, the transmission coefficients and KIE's verses

the imaginary frequencies of the transition state.

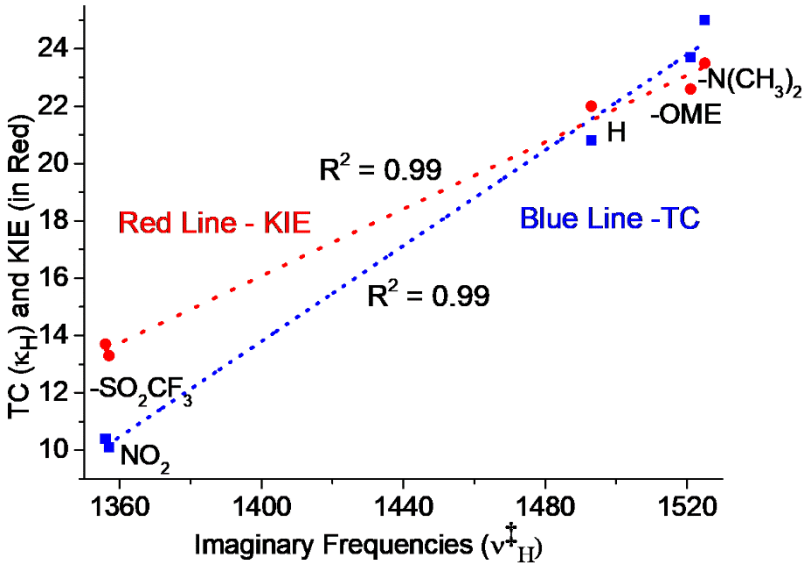

Fig. 3.6 Plot of transmission coefficients for hydrogen and tunneling corrected KIE (298K) versus the imaginary frequencies of the transition states.

This graph clearly shows a distinctive pattern of the variations of the tunneling contribution (TC) and KIE with the imaginary frequency. The unsubstituted compound occupies the intermediate position in the graph, whereas the EDG- and EWG-substituent compound are at the higher and lower ends, respectively. This can be explained by the structure of the transition states. For EWGs, reactant-like and for EDG, more symmetric transition state structures (concerning breaking C-H and forming O-H bond) were obtained, which increased the value of imaginary frequencies from $–SO_2CF_3$ to $N(CH_3)_2$. The images of transition state structures are also depicted along with the PES in Fig. 3.5.

To get the influence of quantum mechanical tunneling on the barrier of activation, a plot of the classical energy of activation (ΔE_{act}) and tunneling corrected activation energy is presented in Fig. 3.7.

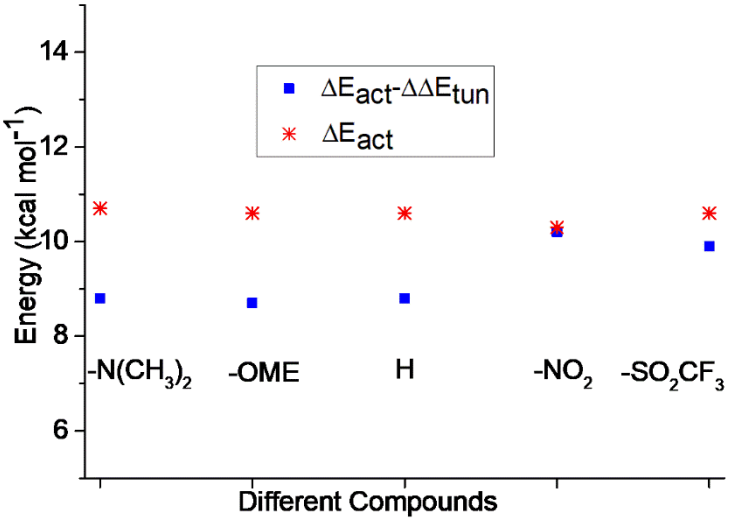

Fig. 3.7 Plot of classical energy of activation (ΔE_{act}) and tunneling corrected activation energy with all the oxidants.

The red star in the figure implies the classical activation energy, which has neither an effect on the reactivity nor the reactivity trend. After subtraction of the barrier reduction quantity due to tunneling (calculated using Eq. 3.2) we got the points depicted as a blue square in Fig. 3.7. These points verified the tunneling contributed to the anti-electrophilic reactivity trends as the activation energy increased in the case of EWG substituents, whereas for EDGs, the effect was not so prominent. Therefore, from the aforesaid discussion, it can be concluded that electron tuning by the substituent can alter the reactivity by tunneling and the effect will be more prominent in the case of more potent EDG or EWG substituents. From the values of Table 3.2 it is also clear that more than 90% of the reactions were performed through tunneling even at room temperature 298K. Again, in the case of EDG, this percentage reaches up to 96% whereas for EWG it was lower at 90%.

3.4.4: TSR and KIE

The KIE can be a direct proof to classify the spin state reactivity. We computed KIE for all reactions in both *S*=1 and *S*=2 states and presented them in Table 3.2. It is clear from the table that for the base compound (unsubstituted), the reported KIE (298K) was 32, which was closer

to *S*=2 (22) but far away from the value (71) at the *S*=1 state, which proves the existence of two-state reactivity.

3.4.5: Discussion of the Reactivity with N4Py

We extended our investigation to verify the reactivity of unsubstituted $[Fe^{IV}(O)(dpaq\text{-}X)]^{+}$ (1) with $[Fe^{IV}(O)(N4Py)]^{2+}$ (2). The related potential energy surface is presented also in Fig. 3.5(f). Experimentally, it was reported that the first one was more reactive as compared to the second one by ~1.5 kcal mol^{-1} in MeCN.[46] We compared next the energy of activation of *S*=2 state for 1 with *S*=1 state for 2, as the earlier reported KIE for 2 with EB suggested the *S*=1 state was the reactive spin state. The classical energy of activation difference between 1 and 2 was ~3.3 kcal mol^{-1}, which could be further improved to 1.9 kcal mol^{-1} by the integration of the tunneling effect, which showed very good agreement with the experiment (~1.5 kcal mol^{-1}). The value of $\Delta\Delta E_{tun}$ for 2 was considered to be ~3.2 kcal mol^{-1} from the previous investigation, which may slightly be altered in the current level of theory but will not change the fact.

3.5: Conclusion

We investigated here the hydrogen-abstraction reactivity of a series of nonheme $[Fe^{IV}(O)(dpaq\text{-}X)]^{+}$ complexes towards ethylbenzene as a substrate. Four substituted dpaq compounds (including two electron-withdrawing and two electron-donating groups) were considered here along with the unsubstituted one.

We showed that the available experimental KIE value (32) for an unsubstituted compound was consistent with the value of theoretical (tunneling corrected) KIE (22) only if the H-abstraction reactions proceeded through the quintet state (*S* = 2), whereas the *S* = 1 state, KIE (71) were very high compare to the experiment. Consequently, these outcomes provide a valid justification of the two-state reactivity (TSR) premise driven by the exchange-enhanced reactivity (EER) concepts.

The energies of the acceptor orbitals, $\sigma^*_{Z^2}$, define the electrophilicity trend for the substituent,

but the reactivity was not much influenced classically by this. The barrier height varied only within ±0.3 kcal mol^{-1}; though, notable impacts of the substituents were found on the transmission coefficient and the energy of activation.

We observed that tunneling was enhanced with strong EDGs. Although the effect was not so strong as with axial ligand alteration, where tunneling showed the anti-electrophilic propensity in H-abstraction by cutting more of the corresponding energy of activation when the substitution was for a stronger electron donor.[15] Finally, after combining the tunnel effect, we got a pattern that established the anti-electrophilic reactivity. More than 90% of the reactions were performed through tunneling, which was boosted to up to 96% for $N(CH_3)_2$.

Further comparison of the reactivity of $[Fe^{IV}(O)(dpaq\text{-}X)]^+$ with $[FeIV(O)(N4Py)]^{2+}$ also provided very good agreement with the experimental outcomes. This also might be due to the EER effect applicable on dpaq as it followed the *S*=2 surface, whereas there was no EER facilitation for N4Py as it followed the *S*=1 state.

Finally, from the aforementioned discussion, we can claim that this investigation strongly demonstrated the effect of electron tuning on quantum mechanical tunneling. These predictions certainly inspire the bioinorganic community to synthesize the oxidants with strong electron-donating groups.

CHAPTER 4

High-Valent Nonheme Fe(IV)O/Ru(IV)O Complexes Catalyze C–H Activation Reactivity and Hydrogen Tunneling: A Comparative DFT Investigation

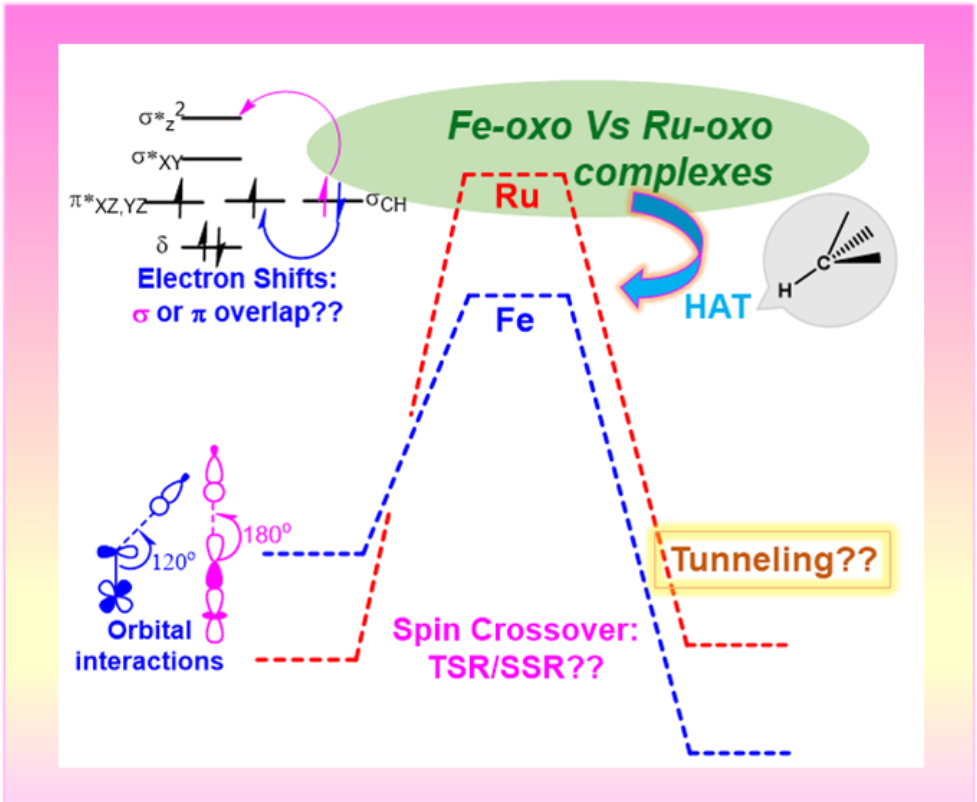

4.1: Introduction

The cofactor of metalloenzymes and their synthetic equivalents mostly consists of high-valent metal oxo species that catalyze various organic (bio)transformations.[1-5] The reactivity of various such synthetic metal-oxo complexes in C-H bond activation and oxygen atom transfer processes has been widely studied.[6-10] To comprehend the chemical and physical properties, as well as the mechanistic actions, of these complexes, a variety of experimental, spectroscopic, and computational approaches have been employed.[11] Several parameters influencing the reactivity have been also identified, e.g., the central transition metal atom, their oxidation state, and spin,[12,13] the connective macrocycles,[14,15] axial and equatorial ligands, etc.[16,17] High-valent iron-oxo species have attracted the greatest attention in this field when used as the central metal in metal-oxo complexes.[18-21] A seemingly never-ending search to understand this chemistry began with the synthesis of $[Fe^{IV}(O)(TMC)(L_{ax})]^{n+}$ complexes (L_{ax}- axial ligand),[22,23] and it is still continuing strong today.[24-30] Besides iron, several high-valent metal-oxo complexes such as those containing Mn, Cr, and Ru have also been found as effective catalysts for C-H activations.[28,31-34] Mn-oxo compounds are known to play a significant role in enzymatic and catalytic oxidation reactions, such as in an oxygen-evolving complex (OEC) in Photosystem II.[35,36] Many biomimetic mononuclear heme and nonheme Mn(IV)O complexes have also been reported as powerful C-H activation catalysts.[37-45] Few investigations are also available related to chromium-oxo complexes and their catalysis.[46,47] High-valent metal-oxo complexes for d^7 and more are rare due to the oxo-wall effect.[32]

Several investigations have been reported where Ru has been used as the central metal instead of iron in biomimetic metal-oxo complexes.[48,49] Shaik and his coworkers reported a comparative electronic structure analysis of the iron-oxo porphyrin and its Ru analog.[50,51] Various experimental investigations were also reported on the mechanistic insight into the C-H activation catalyzed by Ru(IV)O complexes.[52-54] A few instances have shown that the

reactivity of Fe(IV)O complexes follows a counterintuitive trend, i.e., anti-electrophilicity of Fe.[12,16] In contrast, the reactivity Ru(IV)O complexes follows the reverse, i.e., electrophilicity pattern.[55] However, even though considerable attention has been paid to the mechanistic insights and reactivity of Fe and Ru-oxo complexes, a full examination of them with respect to other critical reactivity-regulating factors, such as steric, electronic, hydrogen tunneling, and so on, has yet to be accomplished.

Here, an in-depth DFT analysis was conducted in order to compare the C-H activation reactivity of Fe(IV)O complexes and their Ru counterpart with two ligand macrocycles. The oxidant and substrate details are presented in Fig. 4.1.

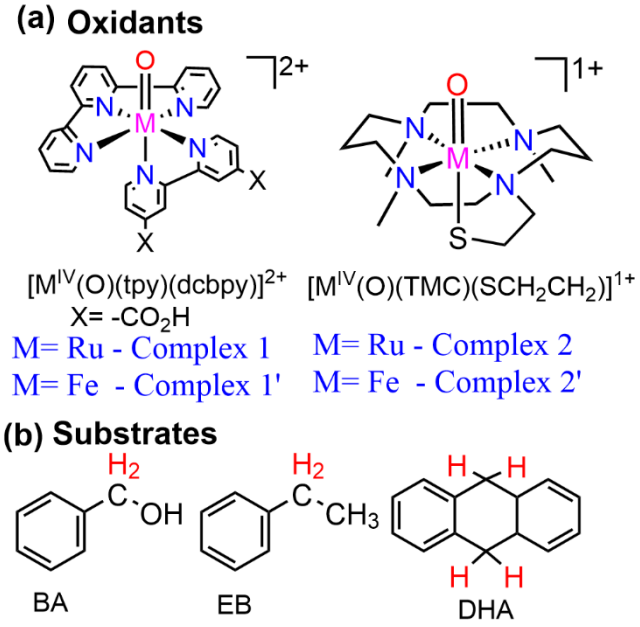

Fig. 4.1 The investigated (a) metal-oxo complexes and (b) substrates for H-abstraction reactions.

Two alternative macrocyclic ligand frameworks were chosen for this purpose: tpy(dcbpy) [(tpy=2,2':6',2''-terpyridine, dcbpy=5,5'-dicarboxy-2,2'-bipyridine)] and TMC with an axially tethered -SCH_2CH_2 group (referred to as TMCS). Macrocyclic tpy(dcbpy) is a well-liked ligand that forms the Ru(IV)O complex[56], whereas TMCS is the standard macrocyclic ligand that stabilises the Fe(IV)O moiety.[16] To facilitate discussion, we numbered the oxo complexes of

Ru and Fe with tpy(dcbpy) as 1 and 1' and with TMCS as 2 and 2'. Three distinct substrates, e.g., dihydroanthracene (DHA), ethylbenzene (EB), and benzyl alcohol (BA) are also used as the source of the C-H bond. Their reactivity may be immensely controlled by quantum mechanical tunneling, as great pieces of evidence have been shown with unusual kinetic isotope effects (KIE).[12,57-59] As a result, we also looked into the role of KIE and hydrogen tunneling effects in reactions mentioned in Fig. 4.1.

4.2: Computational Details

Using DFT-B3LYP techniques, all computations related to geometry optimization, frequency, and thermochemistry have been performed. DFT investigations of the organometallic complexes mostly employ the Becke-Lee-Yang-Parr developed functional B3LYP.[60,61] The Pople's split valence double zeta 6-31G* basis set[62] was used for all atoms except metal ions Fe and Ru, where LANL2DZ[63] basis set with its electrostatic potential was used. This level of theory is designated as B1. To address undesired self-interaction errors in DFT, the total positive charge of the systems was neutralised using the ClO_4^- and $SO_3CF_3^-$ counterions.[64] At the same level of theory, vibrational frequency calculations were done to validate the transition states, where the existence of one imaginary frequency denotes the transition state, and the absence of imaginary frequencies indicates minima. The thermal and entropic corrections to the Gibbs free energy were performed at 298 K.

The single-point energy corrections were also conducted in the same method using 6-311++G(2d,2p) (for all atoms except metals) and SDD-ECP (for Fe/Ru) basis set,[65] named B2. The effect of acetonitrile solvent is also considered implicitly using the self-consistent reaction field (SCRF)[66] approach with Truhlar's solvation model density (SMD) approximation. All the computations mentioned above were performed using the Gaussian 16 software package.[67] The calculation of the percentage of buried volumes and free space was performed using the SambVca 2.1 software.[68] Spin densities, mulliken charges, and natural spin orbitals were used

to identify the electronic state accurately. Chemcraft software was utilized for the result analysis, visualization, and drawing of images.[69] Unless otherwise specified, zero-point corrected energy at the B2 level is mainly considered for further discussion.

4.3: Tunneling Corrections and Kinetic Isotope Effect (KIE) Calculations

The rate constants were computed using Eyring's transition state theory[70] as given in Eq. 4.1.

$$k = \kappa\sigma \frac{k_b T}{h} \exp\left(-\frac{\Delta G^{\ddagger}}{RT}\right) \qquad \text{---------- Eq. 4.1}$$

Where κ denotes the transmission coefficient and σ denotes reaction symmetry. The tunneling calculation was performed using a one-dimensional asymmetric Eckart Method[71], popular in numerous H-transfer/migration processes.[12,57,72-74] This approach constructs the mass-weighted intrinsic reaction coordinate using the zero-point energy (ZPE)-corrected energy of the reactant, transition states, and products with the imaginary frequency of transition states.[75,76] The following equation is used to calculate the transmission coefficient's impact on the activation barrier.

$$\Delta\Delta E^{\ddagger}_{tun} = -\,RT \ln \kappa\,(T) \qquad \text{---------- Eq. 4.2}$$

Where $\Delta\Delta E^{\ddagger}_{tun}$ implies the quantitative reduction of an activation barrier caused by tunneling, whereas R and T represent the universal gas constant and absolute temperature, respectively. Kinetic isotopic effects (KIEs) for all reactions were calculated to verify the existence of the quantum mechanical tunneling. In the KIE calculations, the frequency of the stationary states and their deuterium-substituted equivalents were employed, obtained after accounting for the impact of tunneling using the following Eq. 4.3.

$$KIE_{TC} = (\kappa_H / \kappa_D).\ KIE_{EY} \qquad \text{------- Eq. 4.3}$$

Where κ_H and κ_D symbolize the transmission coefficients of hydrogen and its deuterated isotopomers. The tunneling effect has also been compared with the Wigner approximation.[77] The kisthelp2019 software[78] was used to compute all the kinetics and tunneling.

4.4: Results and Discussion

4.4.1: Spin-State Preferences

Due to degenerate orbitals, unpaired electrons, the strength of the ligand, and other factors, transition metal complexes, primarily those with d^4 to d^7 electron configurations, may have distinct spin states (high or low spin). Here, the Fe(IV) and Ru(IV) complex species are in d^4 configuration and can have possible triplet and quintet spin states. The estimated spin state energy gap ($\Delta E_{Q\text{-}T}$) for Fe(IV)O is approximately 10 kcal mol^{-1}, but Ru(IV)O complexes with the same ligand framework have a very high $\Delta E_{Q\text{-}T}$ of 35 kcal mol^{-1}. Therefore, the quintet state is accessible in Fe(IV)O and may include two-state reactivity (TSR), whereas Ru(IV)O cannot access the quintet state, which offers single-state reactivity (SSR). This was predicted in previous theoretical calculations.[55] The interplay between orbital-promoting energy and exchange interaction, which depends on the number of unpaired electrons and the energy difference across orbitals, largely determines the preferred spin state. In Fe(IV) complexes, the orbital promotion energy is typically lower than the exchange interaction energy, whereas in Ru(IV), the reverse is true.[79] We therefore examined both spin state pathways for Fe(IV)O in the current study as well as only the triplet ground state for Ru(IV)O complex.

4.4.2: Electron Shift Diagram

The hydrogen atom abstraction follows the transfer of one electron from the substrate to the π* or σ^*_{z2} of the metal-oxo moiety depending on its spin state as depicted in Fig. 4.2.

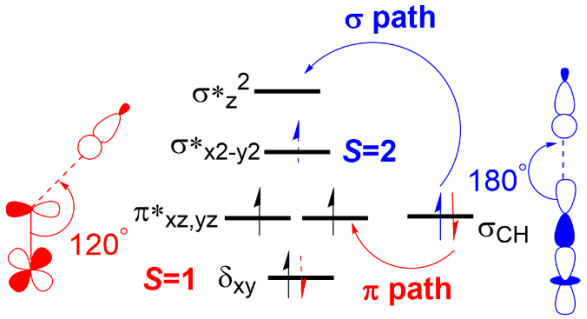

Fig. 4.2 Electron shift diagram during the HAT catalyzed by M(IV)O complexes (M = Ru, Fe).

The transfer of a β electron to the π* of M=O depicted in red occurs in the triplet state, generally called the π trajectory, with the M−O−H angle in the transition state being ∼120°. The blue arrow indicates the shifting of an α electron to the σ^*_{z2} orbital, which occurs in the quintet state called the σ pathway with an ideal M−O−H angle of ∼180°, occurs mainly in cases involving small symmetric substrates and non-bulky ligands. Therefore, in accordance with $\Delta E_{Q\text{-}T}$, the Fe(IV)O catalyzed pathway follows an exchange-mediated σ trajectory, although it possesses a triplet ground state in the reactant, which is usually known as two-state reactivity (TSR).[80] Due to the inaccessibility of higher states in the case of Ru(IV)O, only the π trajectory is possible.

4.4.3: Reactivity

In this section, we have compared the C-H activation reactivity of Ru (1 and 2) with Fe (1' and 2') complexes. The potential energy surface for reactions involving the substrates BA and EB catalysed by the complexes of 1 and 1' is shown in Fig. 4.3.

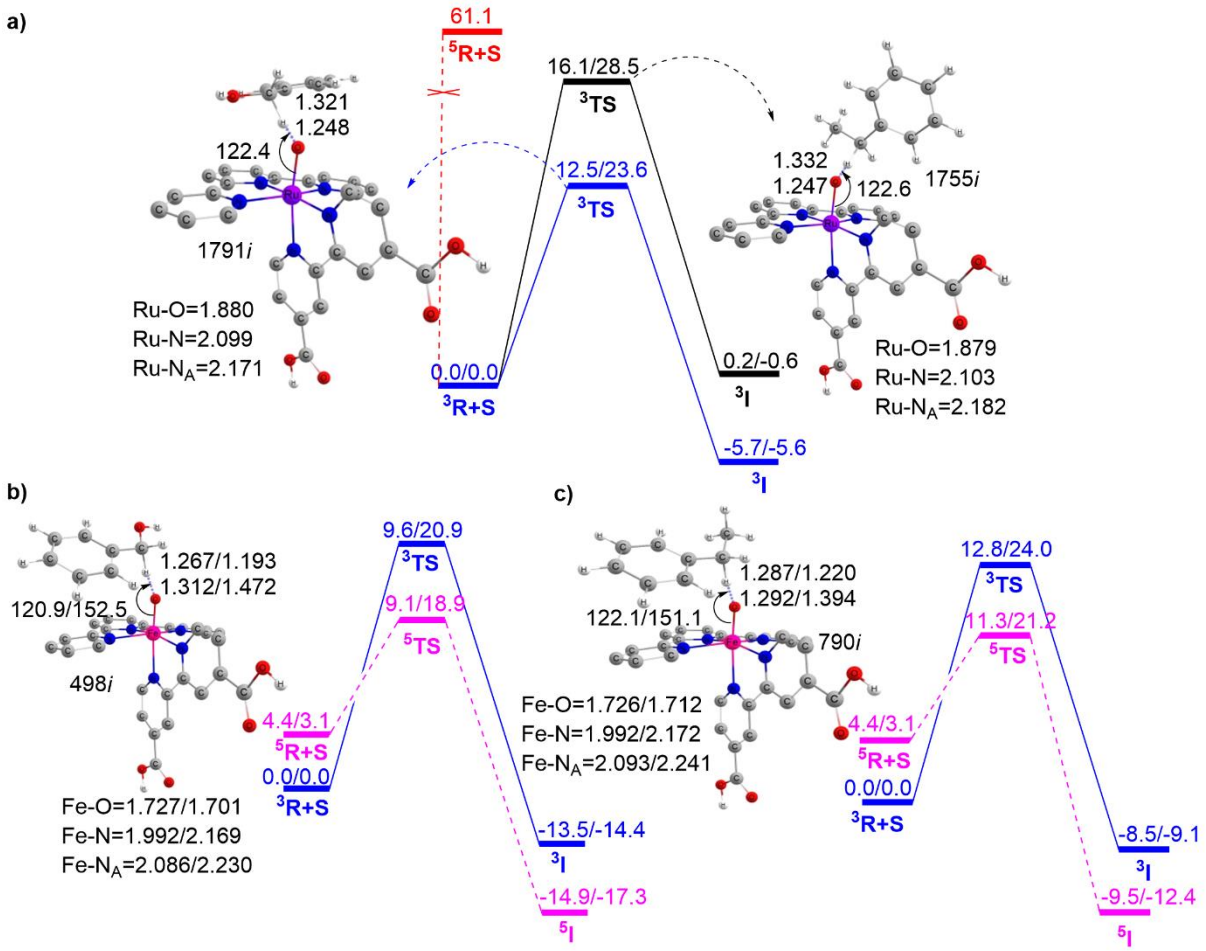

Fig. 4.3 The computed potential energy profile and the involved transition states for the C-H activation reactions of BA and EB catalyzed by (a) 1+BA (b) 1'+BA (c) 1'+EB. The energies (kcal mol^{-1}) are given as B2+ZPE/B2+G^{corr}_{298K}. The distances are in angstrom and angles are in degrees and both triplet /quintet state parameters are given in (b) and (c).

The red line of Fig. 4.3a makes evident that 1 cannot exhibit two-state reactivity as the quintet state possesses 61.1 kcal mol^{-1} higher energy than that of the triplet state, which is itself even four times higher compared to the triplet transition state. For H-abstraction catalysed by 1, the activation energies for BA and EB are found to be 12.5 and 16.1 kcal mol^{-1}, respectively. This is quite expected as EB possesses quite a high bond dissociation energy (85.4 kcal mol^{-1}) compared to BA (79.0 kcal mol^{-1}).[81,82] Our calculated BDE values of 78.1 kcal mol^{-1} for BA and 84.2 kcal mol^{-1} for EB were highly congruent with the experimental BDE value mentioned.

As previously stated, the 1' has two-state reactivity in which the quintet state (the excited state at reactant) crosses the triplet path and becomes lower in transition state and product as presented in Fig. 4.3b. The activation energy of 1'-catalysed processes is 9.1 kcal mol^{-1} for BA and 11.3 kcal mol^{-1} for EB, which is significantly lower than that of the Ru counterpart. This also illustrates the trend of rising energy of activation with C-H BDE.

In order to establish two significant findings, we have expanded our investigation using a second macrocycle, TMCS, with two distinct substrates, such as EB and DHA. The substrate EB is utilised to compare the C-H activation reactivity of macrocyclic ligands tpy-dcbpy and TMCS. The substrate DHA will strengthen facts to understand the C-H activation reactivity versus the substrate's bond dissociation energy. The Ru(IV)O and Fe(IV)O complexes with TMCS ligands are represented as 2 and 2' as shown in Fig. 4.1. The potential energy surface for the reaction of 2 and 2' with EB is presented in Fig. 4.4.

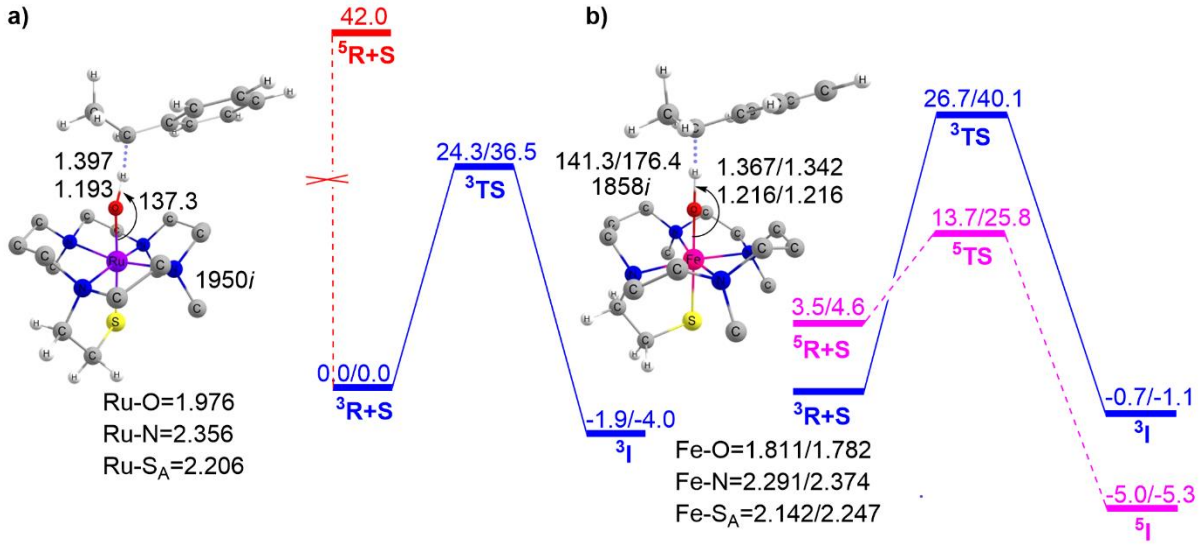

Fig. 4.4 The computed potential energy profile and the involved transition states for the C-H activation reactions of EB catalyzed by (a) 2 (b) 2'. The energies (in kcal mol^{-1}) are given as B2+ZPE/B2+G^{corr}_{298K}. The distances are in angstrom and angles are in degrees and both triplet/ quintet state parameters are given in (b).

Fig. 4.4 shows that the activation barrier for the H-abstraction reaction catalyzed for 2 (24.3 kcal mol^{-1}) vs. 1 (16.1 kcal mol^{-1}) (Fig. 4.3a), there is a 8.2 kcal mol^{-1} difference (barrier 2 is 150% of barrier 1), while for 2' vs. 1' the differences are much smaller (13.7 vs 11.1 kcal mol^{-1}). This fact unequivocally proves the superior catalytic power of tpy-dcbpy over that of the macrocycle TMCS. Next, the potential energy surface for the reaction of 2 and 2' with DHA is presented in Fig. 4.5.

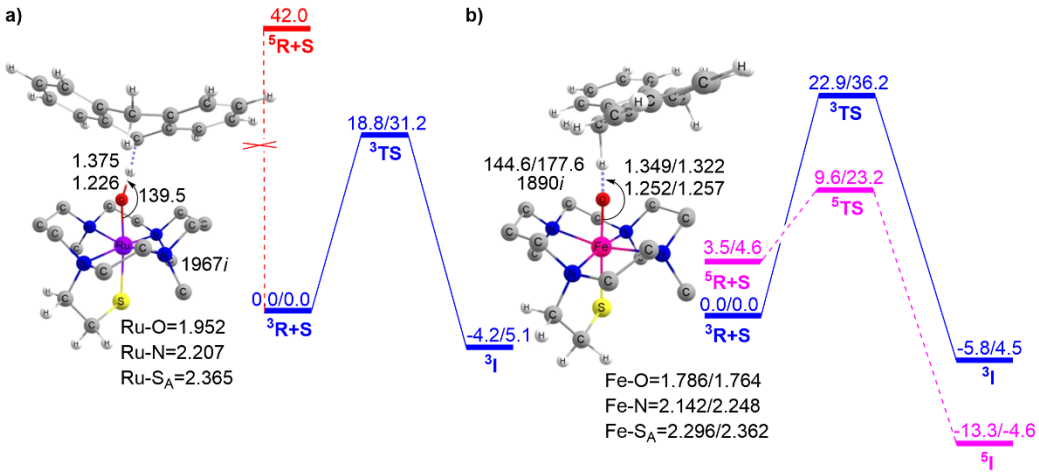

Fig. 4.5 The computed potential energy profile and the involved transition states for the C-H activation reactions of DHA catalyzed by (a) 2 (b) 2'. The energies (kcal mol^{-1}) are given as B2+ZPE/B2+G^{corr}_{298K}. The distances are in angstrom and angles are in degrees and both triplet/ quintet state parameters are given in (b).

The C-H activation barriers of DHA catalysed by 2 and 2' are 18.8 kcal mol^{-1} and 9.6 kcal mol^{-1}, respectively, which are significantly lower than the barrier shown in Fig. 4.4. Fig. 4.4 and 4.5 make it abundantly evident that Fe(IV)O complexes, regardless of the ligand macrocycle or substrate, are far more reactive than their Ru counterparts.

4.4.4: Aliphatic vs. Aromatic Hydroxylation

In an investigation, de Visser *et. al.,*[83] have shown that the axial ligand of a heme-type Fe(IV)O complex has a quantitative impact on the regioselective hydroxylation of EB. With this as a

motive, we were also curious to see if the metal modification affected the selective hydroxylation in EB. We have considered the complex 1 and 1' for this purpose. The activation energies and the transition states for aromatic hydroxylation are presented in Table 4.1 and Fig. 4.6.

Table 4.1 Calculated energy of activation and free energy of activation (kcal mol^{-1}) are given as B2+ZPE/B2+G^{corr}_{298K} level of theory.

Complex	Aliphatic hydroxylation $\Delta E/\Delta G^{\ddagger}$	Aromatic hydroxylation $\Delta E/\Delta G^{\ddagger}$
1+EB	16.1/28.5	27.9/39.8
1'+EB	11.3/21.2	15.2/24.5

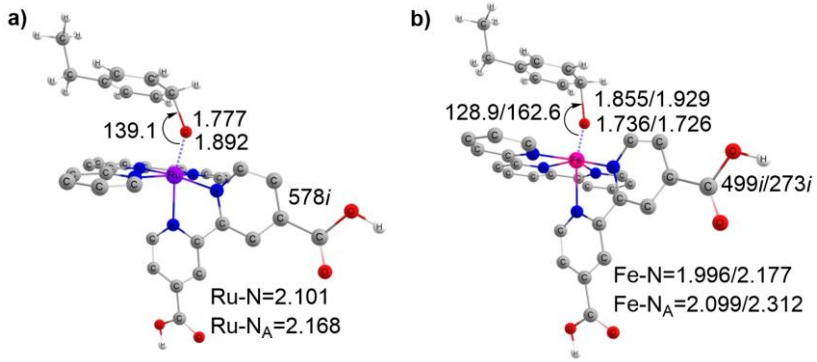

Fig. 4.6 Optimized geometries of (a) $^{3}TS_{O}$ (b) $^{5}TS_{O}$ with key geometrical parameters computed at B1 level of theory (distances are in Å and angles are in degree).

The activation energies for the aromatic hydroxylation of EB catalysed by 1 and 1' are 27.9 and 15.2 kcal mol^{-1}, respectively, (in Table 4.1), which is significantly higher than C-H activation energy barriers (16.1 and 11.3 for 1 and 1' respectively), as shown in Fig. 4.3. These energies offer two intriguing pieces of evidence: first, in accordance with aliphatic hydroxylation, the Fe(IV)O complex is more reactive in aromatic hydroxylation than its Ru counterpart, and second, regardless of the central metal ion, aliphatic hydroxylation is more favourable than aromatic hydroxylation. This is well reflected by the corresponding C-H bonds.[84] Therefore, it was decided not to investigate the aromatic hydroxylation reactions any further. We can now

proceed to explore the insight into the greater C-H activation reactivity (aliphatic hydroxylation) of the Fe(IV)O complex.

4.4.5: Steric Factor

In the context of the accessibility of the abstractor, M=O, towards the substrate, the value of free space has been reported in Table 4.2. The values e.g., 10.9% and 10.4% for ^{3}1 and ^{5}1', respectively, indicate that the free spaces are not much dependent on the metal atom. The same trend of available space is observed for ^{3}2 (2.8%) and ^{5}2' (3.4%). This evidence allows us to confidently state that while the steric factors do not prefer one metal over another, they can contribute to the higher reactivity of the tpy-dcbpy complex.

Table 4.2 Calculated % Volume buried and %free space for oxidants computed on the geometry optimized at B1 level of theory

Oxidants	Spin state	% Volume buried	% Free space
1	*S*=1	89.6	10.4
1'	*S*=2	89.1	10.9
2	*S*=1	97.2	2.8
2'	*S*=2	96.6	3.4

4.4.6: Distortion Energy

We then proceeded to check the essential distortion energy required to achieve the transition states and the corresponding values are given in Table 4.3.

Table 4.3 Distortion energy ($\Delta E^{\ddagger}_{dis}$, kcal mol^{-1}) and the contribution from substrate (ΔS) and oxidant (ΔO).

Reaction	ΔS	ΔO	$\Delta E^{\ddagger}_{dis}$
1+BA	13.0	2.9	15.9
1'+BA	4.0	4.6	8.6
1+EB	15.8	2.0	17.8
1'+EB	6.8	5.6	12.4
2+EB	21.2	6.9	28.1
2'+EB	15.8	4.2	20.0
2+DHA	17.1	5.4	22.5
2'+DHA	12.9	3.2	16.1

The table clearly shows that the distortion energies for the Ru complexes are around 5-7 kcal mol^{-1} higher than those for the comparable Fe complexes, perfectly depicting the pattern of the reaction's activation energies. It is also worth noting that substrate deformation is frequently noted as the primary contributor to overall distortion energy, and that it is substantially higher in the case of Ru complexes when compared to Fe complexes. This could be as a result of mostly early transition states for Fe and late transition states for Ru.

4.4.7: Energy of the Electron Acceptor Orbital in Oxidant (E_{AO})

The electron transfer from substrate to oxidant is essentially followed by this C-H activation procedure. Therefore, in this process, oxidants with low-lying acceptor orbitals will be more reactive. In accordance with this rationale, we further examined and contrasted the acceptor orbital energies of the Ru complexes 1 and 2 with those of their Fe counterparts 1' and 2'. Continuing from the electron shift diagram Fig. 4.2, the $\pi^*_{xz/yz}$ orbital is thought of as the acceptor orbital for Ru complexes while the σ^*_{z2} orbital is thought of as being that for Fe, and the corresponding images with their energy values are presented in Fig. 4.7.

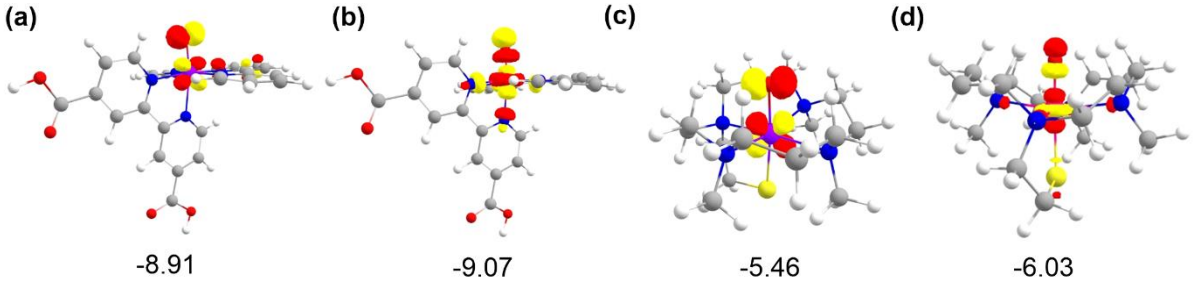

Fig. 4.7 The image and energy (in eV) of the electron acceptor orbital (E_{AO}) oxidant: (a) 1 ($\pi^*_{xz/yz}$), (b) 1' (σ^*_{z2}), (c) 2 ($\pi^*_{xz/yz}$) and (d) 2' (σ^*_{z2}).

It shows that the acceptor orbitals of Ru complexes 1 (-8.91 eV) and 2 (-5.46 eV) have higher energies than those of their equivalent Fe counterparts 1' (-9.07 eV) and 2' (-6.03 eV). This also explains why the Fe complexes have a higher C-H activation reactivity than those of the Ru

complexes. It is also important to note that, regardless of the metal atom, the energy of E_{AO} is substantially lower in the case of the tpy-dcbpy macrocycle when compared to TMCS.

4.4.8: Hydrogen Tunneling

The investigation of Myeong *et.al*., and Johaness *et.al*.,[59,85] reported extraordinarily high kinetic isotope effect (k_H/k_D) values for the H-abstraction reaction of the 1+BA (54.5 at 298K) and 2'+DHA (80 at 253K) systems, respectively, clearly signifies the presence of H-tunneling in the reaction. Therefore, in order to generalise the reactivity pattern, a thorough comparison of the extent of the tunneling impact on the C-H activation reactivity catalysed by Ru complexes and their Fe counterpart has been taken into account and the corresponding outcomes are outlined in Table 4.4.

Table 4.4 The imaginary frequencies of the transition states ($\nu^{\ddagger}_H$), transmission coefficients for H (κ_H) and D (κ_D), kinetic isotope effect at 298K, tunneling correction on activation ($\Delta\Delta E^{\ddagger}_{tun}$, kcal mol^{-1}) at 298 K, and tunneling-corrected activation barrier (ΔE-$\Delta\Delta E^{\ddagger}_{tun}$, kcal mol^{-1}) at the B2+ZPE level and the tunneling contribution (%tunneling) of the overall reaction for all the investigated H-abstraction processes.

Reactions	$\nu^{\ddagger}_H$	κ_H	κ_D	KIE	$\Delta\Delta E^{\ddagger}_{tun}$	ΔE-$\Delta\Delta E^{\ddagger}_{tun}$	%tunneling
1+BA	1791	69.9	9.4	48.3	2.5	10.0	97.9
1'+BA	498	1.3	1.2	3.6	0.2	8.9	72.2
1+EB	1755	43.6	8.1	27.6	2.2	13.9	96.4
1'+EB	790	2.0	1.6	4.6	0.4	10.9	78.3
2+EB	1950	487.9	21.4	127.6	3.7	20.6	99.2
2'+EB	1858	184.7	14.9	73.2	3.1	10.6	98.6
2+DHA	1967	1059.9	27.0	253.8	4.1	14.7	99.6
2'+DHA	1890	217.8	17.1	80.6	3.2	6.4	98.8

Our estimated values for 1+BA (48.3) show a very near match with the experiment. However, the computed values for 2'-DHA show a variation as the experimental KIE has been reported at very low temperature, which is typically a concern with the Eckart method. An intriguing characteristic is found from the table that Ru compounds have very high transmission

coefficients (69.9, 43.6, 487.9 and 1059.9 for the reaction of 1 + BA, 1 + EB, 2+EB and 2 + DHA, respectively) when compared to their Fe equivalent (1.3, 2.0, 184.7 and 217.8 for the reaction of 1'+BA, 1'+EB, 2'+EB and 2'+DHA, respectively). This could be due to the narrow potential energy surface represented by the imaginary frequency ($\nu^{\ddagger}_{H}$) and high activation energy. According to the transmission coefficient, Ru has a higher barrier-lowering energy than Fe (column 5), but this does not change the pattern (column 6); rather, it minimises the difference in their activation energies. It is also crucial to note that tunneling contributes more than 96% of the reactions overall, with the exception of 1'+BA and 1'+EB, where it contributes more than 72%.

4.5: Conclusion

A number of significant conclusions can be drawn from the extensive DFT data presented here, which compare the C-H activation reactivities of mononuclear nonheme Fe(IV)O and Ru(IV)O complexes containing two similar macrocyclic ligand frameworks, namely tpy-dcbpy, and TMCS. It was found that compared to their Ru-oxo counterparts, Fe-oxo complexes are more reactive towards HAT reactions. Regardless of the metal atom, the tpy-dcbpy complexes are shown to be significantly more reactive than the TMCS complexes. It was also found that aliphatic hydroxylation is advantageous irrespective of the oxidant's central metal atom. Several important insights into this reactivity pattern have been identified. In contrast to Ru(IV)O, which lacks an exchange-enhanced transition state because of the inaccessible quintet state, Fe(IV)O exhibits two-state reactivity as usual, where exchange interaction between unpaired electrons stabilises the transition states and increases the reactivity. In addition, compared to Ru(IV)O, deformation energies favour the formation of transition states in the case of Fe(IV)O. The energy of the LUMO, or an electron acceptor orbital of the oxidants, which is found to be lower in Fe(IV)O compared to its Ru equivalent, is the next crucial factor for reactivity. Furthermore, it is notably lower in the tpy-dcbpy macrocycle than

that in its TMCS counterpart, which adds to the tpy-dcbpy macrocycle's higher reactivity. More than 72% of each reaction is carried out by the H-atom's quantum mechanical tunneling, which has a considerable effect on the reaction. The tunneling contribution as well as KIE's are significantly higher in HAT catalysed by Ru complexes than that in Fe complexes. This is because Ru has a narrow potential energy surface, which is implied by the high imaginary frequency in the transition state. However, the reactivity pattern has not changed noticeably even after the quantum influence on the activation energy was taken into account. Finally, it is evident from this analysis that ruthenium-oxo is less reactive than the high-valent iron-oxo complex, suggesting that Fe is one of the important cofactors of metalloenzymes that catalyse C-H activation. This finding may indicate that Fe is the natural choice for cofactor in metalloenzymes.

CHAPTER 5

Impact of Carboxylate Ligation on the C-H Activation Reactivity of Non-Heme Fe(IV)O Complex: A Computational Investigation

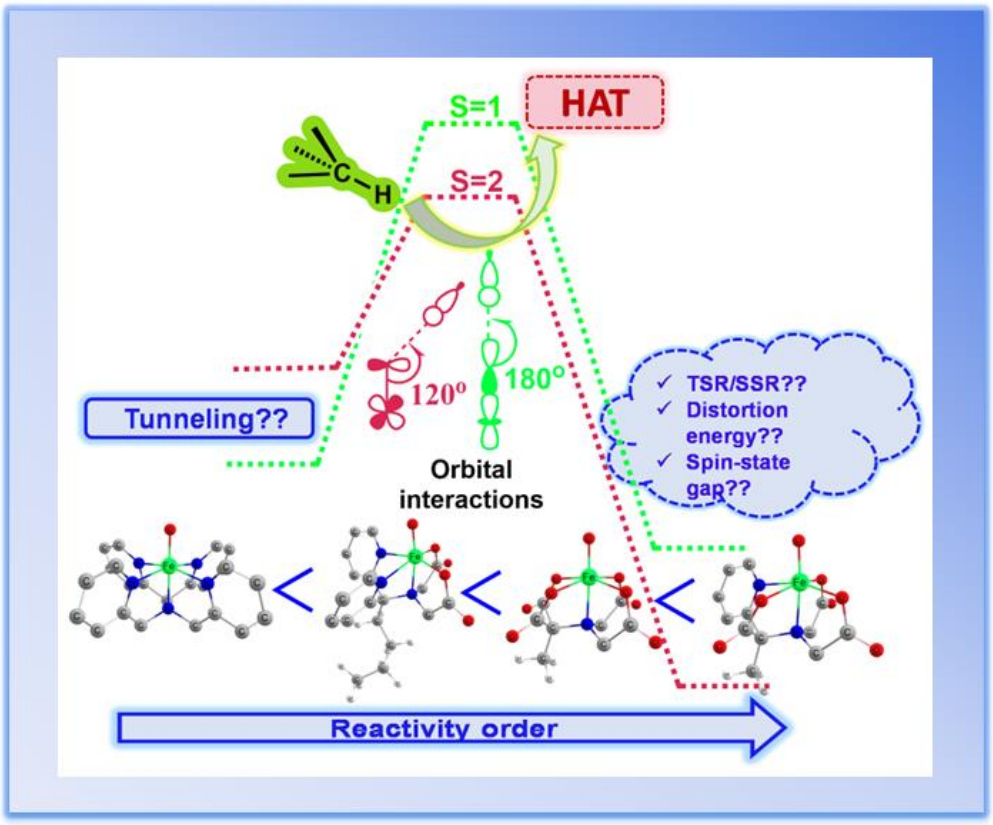

5.1: Introduction

Currently, synthetic iron(IV)-oxo complexes, which serve as bio-inspired models for active mononuclear non-heme iron enzymes, are gaining interest for their potential in catalyzing C-H activation reactions.[1-9] These oxygen-activating metalloenzymes are involved in vital metabolic activities, toxin inactivation, DNA repair, and more. The structural and electronic characteristics of their metal-binding active sites are significantly influenced by relatively weak field carboxylate ligation which facilitates a diverse array of oxidative transformations.[10-13] The 2-His-1-carboxylate facial triad[14-18] has been mostly identified as the associated structural motif for the active sites of these enzymes such as (i) α-ketoglutarate (α-KG) dependent-taurine dioxygenase (TauD), (ii) 1-aminocyclopropane-1-carboxylic acid oxidases (ACCO), (iii) phenylalanine hydroxylase (PheH), a pterin-dependent hydroxylase) as presented in Fig. 5.1.[19-31]

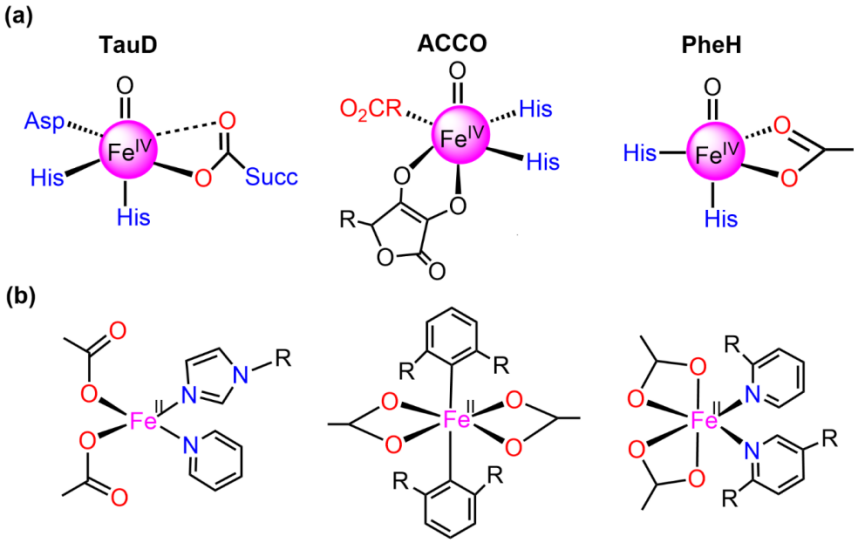

Fig. 5.1 Structures of (a) 2-His-1-carboxylate facial triad superfamily of non-heme iron enzymes and (b) mononuclear Fe(II) carboxylate ligated complexes.

Numerous mononuclear Fe(II) complexes linked with two carboxylate donors have also been extensively characterised (in Fig. 5.1).[32-39] In line with this McDonald *et al.*,[40] synthesized the macrocycle BuP2DA by substituting the two pyridine donors N4Py with carboxylate. They

also demonstrated that the C-H activation reactivity of the Fe(IV)O-BuP2DA complex was found to be 6-fold larger than that of the N4Py counterpart. Several investigations have shown that enrichment with oxygen or sulfur donors in the macrocycle, in addition to carboxylate, increases the reactivity of Fe(IV)O compared to nitrogen.[41,42] Que and co-workers[43] reported that the reactivity of the Fe(IV)O unit is increased by the presence of a trans-carboxylate ligand in comparison to a neutral acetonitrile ligand. While considerable research has been dedicated to the mechanistic insights and reactivity of carboxylate-ligated Fe-oxo complexes,[44] there remains a dearth of comprehensive investigations concerning other crucial reactivity-regulating factors, including steric, electronic, hydrogen tunneling, and so forth.

Here, the main objective is to ascertain whether carboxylate-substituted iron-oxo complexes may provide us with an improved C-H activation reactivity and how well these enhancements would occur sequentially. For this purpose, two alternative macrocyclic ligand frameworks were selected. In Fig. 5.2a, a non-heme iron oxo complex consisting of four nitrogen atoms and comprising the equatorially connected macrocyclic framework $[Fe^{IV}(O)(N4Py)]^{2+}$, (N4Py = N,N-(bis(2-pyridyl)methyl)N-bis(2-pyridylmethyl)amine)) (1), has been taken as a primary compound, as previously reported.[40] By substituting two pyridine donors of the N4Py ligand with carboxylate ligands in the equatorial plane namely, $[Fe^{IV}(O)(^{n}Bu\text{-}P2DA)]$, where ^{n}Bu-P2DA = N-(1',1'-bis(2-pyridyl)pentyl)iminodiacetate) (2), the influence of carboxylate ligated substitution on reactivity catalysed by the HAT mechanism was investigated.[40] Furthermore, this investigation has been broadened by incorporating derivative compounds (3 and 4, as illustrated in Fig. 5.2b), which are produced by successively substituting N with the carboxylate group.

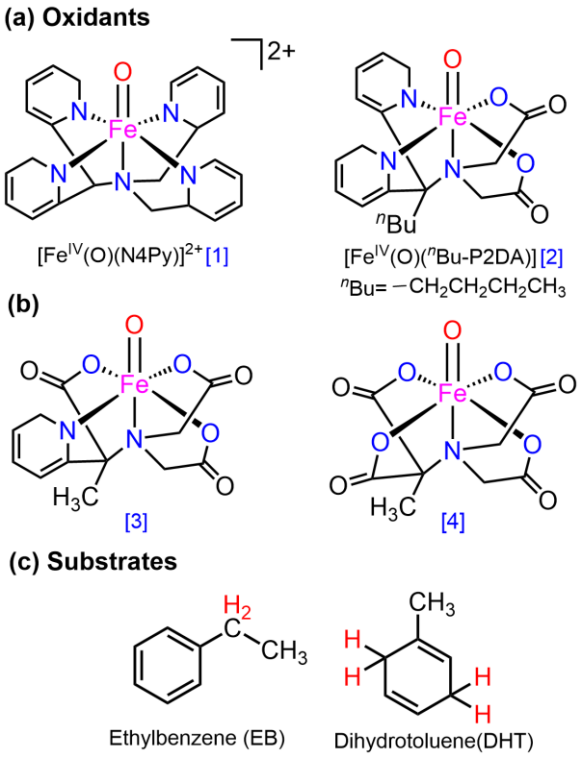

Fig. 5.2 The investigated (a) [Fe^{IV}O(N4Py)] (**1**, left) and [Fe^{IV}(O)(^{n}Bu-P2DA)] (**2**, right); (b) complexes with sequential replacement of carboxylate group at equatorial position; c) substrates for HAT reactions.

As the source of the C–H bond, two distinct substrates, such as ethylbenzene (EB) and dihydrotoluene (DHT), are employed. Numerous potential factors could influence the reactivity such as the possible spin-state pathway, deformation energy to acquire the transition states, the triplet-quintet energy gap, and so forth, which have been extensively investigated. Quantum mechanical tunneling and the H/D kinetic isotope effect[45,46] have also been examined in the context of carboxylate-ligated macrocycles.

5.2: Computational Details

The DFT-B3LYP methodologies, which have been implemented in Gaussian 16,[47] were utilised to perform all computations related to optimization, frequency, thermochemistry, etc. The B3LYP functional developed by Lee-Yang-Parr is successfully employed in many organometallic reaction chemistry.[48-58] The following basis sets are utilised here: (i)

LANL2DZ[59] basis and ECP for Fe and Pople's double zeta 6-31G*[60] for all other atoms, which are conveniently termed as B1 for the presentation. To validate the transition states, vibrational frequency calculations were performed; the presence of an imaginary frequency signifies the transition state, while the absence of such frequencies indicates minima. At 298 K (25 °C), the thermal and entropic corrections to the Gibbs free energy were carried out.

Additional single-point calculations were accomplished to refine the energy using (ii) 6-311++G(2d,2p) for all atoms and SDD-ECP[61] for Fe, classified as B2. The implicit impact of the solvent, acetonitrile (CH_3CN) was evaluated by utilisation of the self-consistent reaction field (SCRF)[62] approach in conjunction with Truhlar's solvation model density approximation (SMD). Using the perchlorate (ClO_4^-) counterions, the systems' overall positive charge was neutralised to resolve unwanted self-interaction problems in DFT.[63] The determination of the percentage of concealed volumes and available capacity was accomplished by using the SambVca 2.1 software.[64] With the aid of spin densities, mulliken charges, and natural spin orbitals, the electronic state was precisely identified. The Chemcraft software was employed to perform image rendering, result depiction, and analysis.[65] For the purpose of further discussion, zero-point corrected energy at the B2 level is predominantly used, unless otherwise specified. Using the KisthelP2019 software,[66] the kinetic isotope effect (KIE) and quantum mechanical tunneling have been performed. Eq. 5.1 illustrates how the rate constants were calculated via Eyring's transition state theory.[67]

$$k = \kappa\sigma \frac{k_b T}{h} \exp\left(-\frac{\Delta G^{\ddagger}}{RT}\right) \qquad \text{---------- Eq. 5.1}$$

Here, the transmission coefficient and reaction symmetry are designated by κ and σ, respectively. A one-dimensional (1-D) asymmetric Eckart approach, which has become prevalent in a variety of transfer or migration of H-processes,[45,46,68-70] was used to assess the tunneling. The subsequent equation generates the effect of the transmission coefficient on the barrier of activation.

$$\Delta\Delta E^{\ddagger}_{tun} = -RT \ln \kappa (T) \quad \text{---------- Eq. 5.2}$$

This equation denotes, the quantitative reduction of an activation barrier resulting from tunneling ($\Delta\Delta E^{\ddagger}_{tun}$), the universal gas constant (R), and absolute temperature (T).

To prove quantum mechanical tunneling, all reactions' (H/D) KIEs were determined. The KIE computations used the frequency of stationary states and their deuterium-replaced counterparts, calculated after tunneling influence using Eq. 5.3.

$$KIE_{TC} = (\kappa_H / \kappa_D).\ KIE_{EY} \quad \text{------- Eq. 5.3}$$

The transmission coefficients of hydrogen are symbolised by κ_H while its deuterated isotopomers are represented by κ_D. The tunneling contribution for a reaction can be contributed using the following Eq. 5.4:[71]

$$\% \text{ tunneling} = 100[(\kappa_{Eckart} - 1)/ \kappa_{Eckart}] \text{ ------- Eq. 5.4}$$

Here, κEckart denotes the transmission coefficient in Eq. 5.1, which is determined using the Eckart method. Consequently, the numerator in Eq. 5.4 reflects the difference between a reaction that includes tunneling and one where the transmission coefficient is unity, $\kappa = 1$, indicating no tunneling effect. Therefore, the ratio $[\kappa_{Eckart} - 1)/ \kappa_{Eckart}]$ quantifies the extent of tunneling contribution.

Furthermore, distortion energies have been evaluated for the transition state, defined by the following equation:

$$\Delta E^{\ddagger}_{dist} = (E^{\ddagger}_R + E^{\ddagger}_S) - (E_R - E_S) \quad \text{------- Eq. 5.5}$$

The substrate and reactant equivalents are signified by S and R, in their structure of transition state. Here, E(S) and E(R) are defined as the energies of the substrate and reactant in their undistorted state whereas E‡(S) and E‡(R) are the single-point energies of the separated substrate and oxidant fragments in the transition state.

5.3: Result and Discussion

5.3.1: Spin-State Preferences and Two-State Reactivity (TSR)

Complexes of Fe(IV)O may manifest two close-lying spin states: triplet state (S = 1, two unpaired electrons) and quintet state (S = 2, four unpaired electrons). The same was observed in this study (in Table 5.1), with S = 1 representing the ground state and S = 2 implying the higher energy state.

Table 5.1 The relative energies and free energies at 298K (kcal mol^{-1}) for all the species involved in the investigated reactions computed at different levels of theory.

Reactions	Spin state	Species	B1+ZPE	B2+ZPE	B2+G^{corr}
1-EB	S=1	^{3}RC	0.0	0.0	0.0
		^{3}TS	17.5	14.9	26.3
		^{3}IH	1.7	-4.5	5.1
	S=2	^{5}RC	9.9	6.5	3.8
		^{5}TS	21.3	12.0	21.5
		^{5}IH	7.9	-6.9	0.5
2-EB	S=1	^{3}RC	0.0	0.0	0.0
		^{3}TS	10.8	14.2	25.8
		^{3}IH	-4.3	-4.3	5.6
	S=2	^{5}RC	1.6	2.9	3.7
		^{5}TS	9.8	9.2	18.6
		^{5}IH	-10.1	-14.2	-6.4
1-DHT	S=1	^{3}RC	0.0	0.0	0.0
		^{3}TS	11.6	10.5	22.3
		^{3}IH	-11.2	-16.6	-7.2
	S=2	^{5}RC	9.9	6.5	3.8
		^{5}TS	15.4	7.5	17.1
		^{5}IH	1.6	-18.6	-10.4
2-DHT	S=1	^{3}RC	0.0	0.0	0.0
		^{3}TS	6.3	9.9	21.0
		^{3}IH	-16.7	-16.0	-6.8
	S=2	^{5}RC	1.6	2.9	3.7
		^{5}TS	5.4	3.6	13.0
		^{5}IH	-23.0	-25.3	-17.0
3-EB	S=1	^{3}RC	0.0	0.0	0.0
		^{3}TS	14.3	13.4	24.7
		^{3}IH	-2.3	-3.7	9.4
	S=2	^{5}RC	2.1	2.0	3.6
		^{5}TS	9.5	7.8	17.5
		^{5}IH	-12.1	-15.4	-3.5
4- EB	S=1	^{3}RC	0.0	0.0	0.0
		^{3}TS	14.9	11.4	22.3

		^{3}IH	-3.6	-1.5	10.3
	S=2	^{5}RC	3.9	1.5	2.7
		^{5}TS	6.0	5.7	16.1
			-17.4	-12.3	-1.2

The $\Delta E_{T\text{-}Q}$ for complex 1 was 6.5 kcal mol^{-1}, which was reduced to approximately 2.9, 2.0, and 1.5 kcal mol^{-1}, in complexes 2, 3, and 4, respectively (in Fig. 5.3). This is expected because replacing a nitrogen-containing pyridine group with an oxygen-containing carboxylate group weakens the ligand field, making the high-spin state more accessible. As compared to the other Fe(IV)O complexes that exhibit the TSR,[53] here, also $\Delta E_{T\text{-}Q}$ was found to be smaller, hence it may possess the ability to access the quintet state. Consequently, we have computed both triplet and quintet reaction pathways.

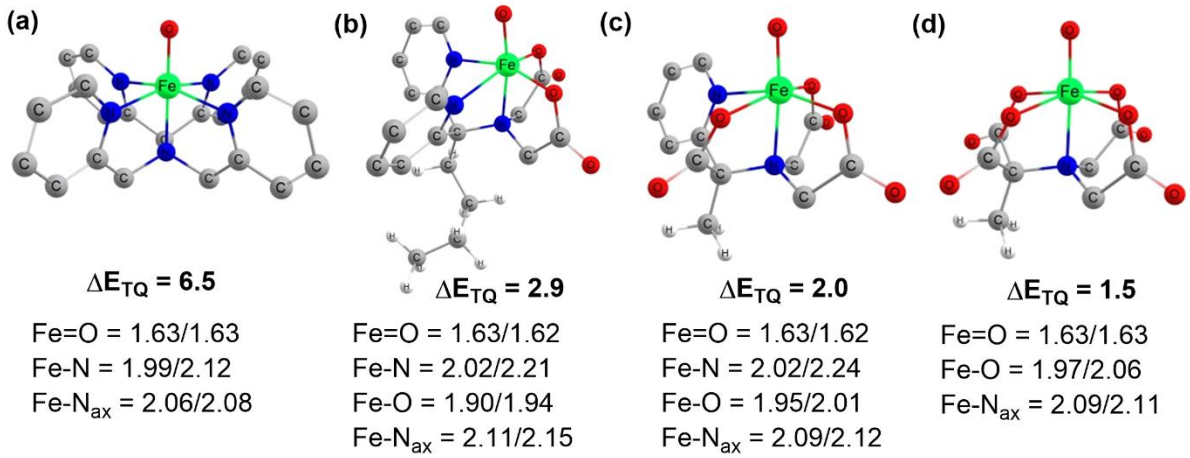

Fig. 5.3 Optimized geometries with geometry parameters (distances are in Å), and $\Delta E_{T\text{-}Q}$ (in kcal mol^{-1}) (a) 1 (b) 2 (c) 3 (d) 4 for both triplet/quintet spin states at B1 level of theory.

The sequential addition of carboxylate groups had minimal impact on the geometries of the oxidants, as illustrated in Fig. 5.3. There are slight alterations in the parameters: however, the bond lengths of the axially connected Fe=O and Fe–N$_{ax}$ remain nearly identical across all four oxidants.

5.3.2: Electron Shift Diagram

In the C-H activation reaction, the abstraction of hydrogen occurs with the movement of one electron from the substrate to the acceptor orbital, which may be either anti-bonding orbital π* (for *S*=1) or σ^*_{z2} (*S*=2) of the Fe(IV)oxo complex as presented in Fig. 5.4.

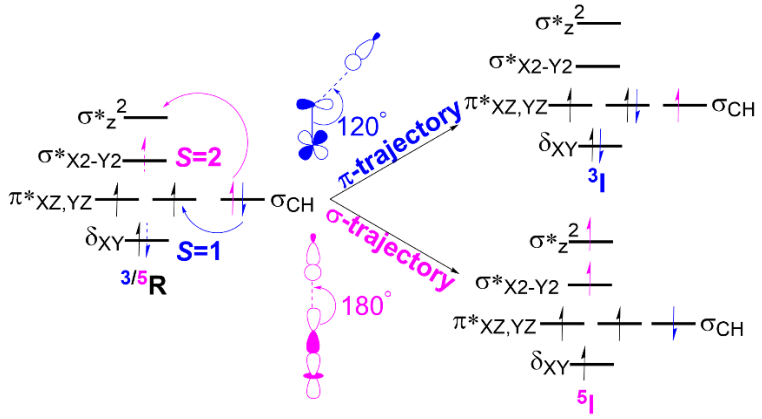

Fig. 5.4 The electron transfer diagram for spin states S = 1 (blue) and S = 2 (pink) during hydrogen atom transfer facilitated by Fe(IV)O complexes.

In the triplet state (*S*=1), the π trajectory, with a Fe-O-H angle of about 120°, involves the transfer of a β-electron to the acceptor orbital (π*) of the Fe-oxo moiety (shown in blue). Conversely, in the quintet state (*S*=2), the transfer of an α-electron via the σ route to the acceptor orbital (σ^*z^2) is depicted by the pink arrow, with an ideal Fe-O-H angle of around 180°, only observed for highly symmetric small substrates and non-bulky ligands. This study also follows the exchange-enhanced reactivity (EER)[72] as the transition state on the quintet surface has lower energy than that on the triplet surface due to increased exchange interactions (the *S* = 2 transition state has more unpaired electrons than the *S* = 1 state). Consequently, during the reaction, the quintet state exhibits a more stable intermediate as it crosses the triplet state.

5.3.3: Reactivity Analysis

This section outlines the comparison of the HAT reactivity between complexes 1 and 2 with EB and DHT. The corresponding potential energy surface is presented in Fig. 5.5.

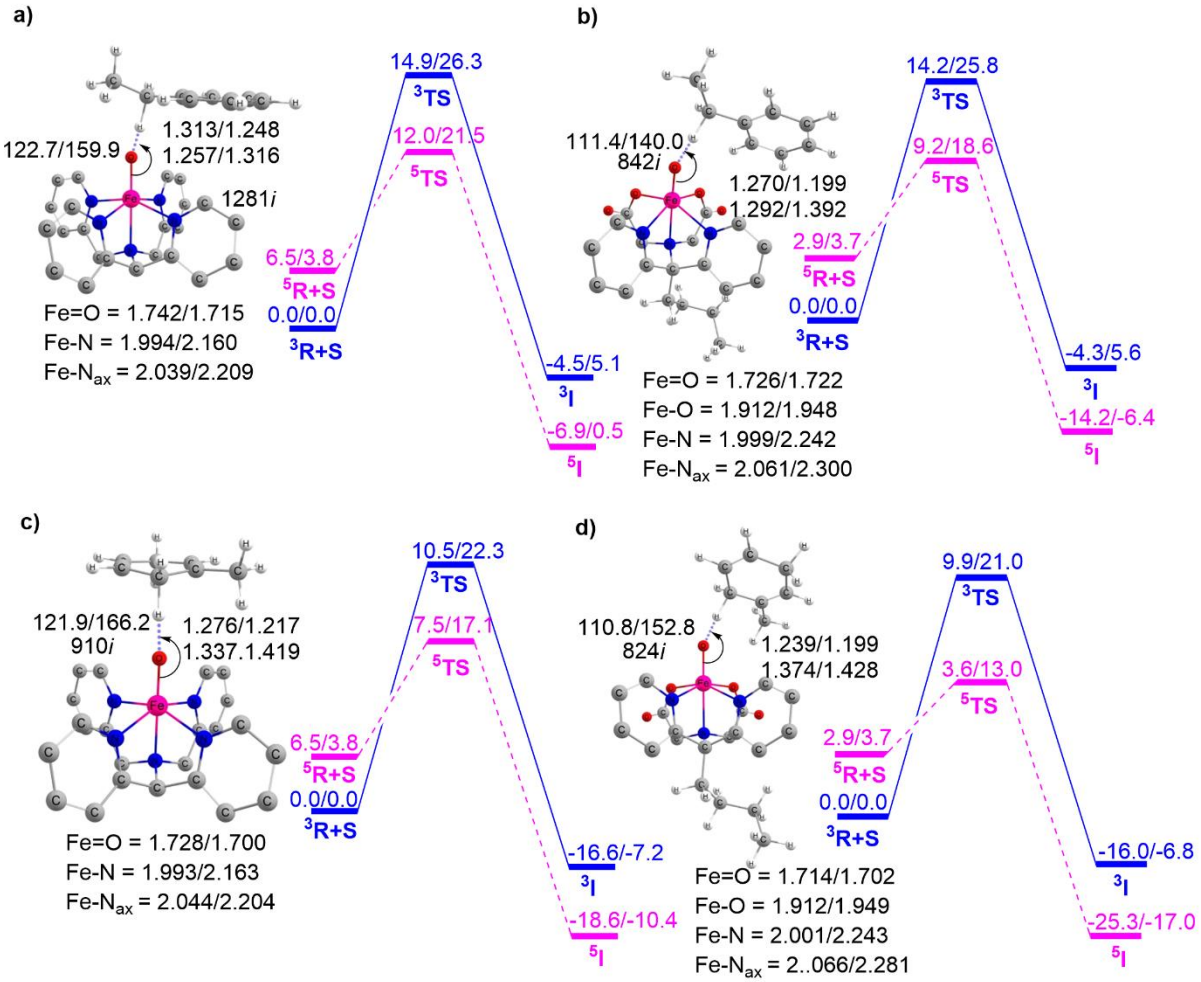

Fig. 5.5 The potential energy profile computed for C–H activation reactions (a) 1+EB (b) 2+EB, (c) 1+DHT (d) 2+DHT, with the associated transition states. The energies are represented as ΔE (B2+ZPE)/ ΔG (B2+ G^{corr}_{298K}) in kcal mol^{-1}. Both triplet/quintet spin state parameters are provided along with the lengths and angles expressed in angstroms and degrees, respectively.

As previously mentioned, the PES shows the TSR pattern for these Fe(IV)O complex-catalyzed HAT reactions. Fig. 5.5a and 5.5b indicate that the H-abstraction from EB catalyzed by complex 1 has an activation barrier of approximately 12.0 kcal mol^{-1}. This value is considerably higher compared to the identical reaction catalyzed by complex 2, which has an activation barrier of 9.2 kcal mol^{-1}. This clearly demonstrates that the Fe(IV)O complex BuP2DA ligand has a greater catalytic potential than the macrocycle N4Py. We then proceed to discuss Fig.

5.5c, and d which provide the potential energy surface for the HAT reaction of complexes 1 and 2 with a different substrate DHT.

These figures again demonstrate the higher reactivity of BuP2DA over N4Py, regardless of the substrate. The activation barrier for DHT catalyzed by complex 1 is 7.5 kcal mol^{-1}, while for complex 2 it is 3.6 kcal mol^{-1}. Furthermore, the facts about the C-H activation reactivity concerning the substrate's bond dissociation energy (BDE) will also be amplified by the substrates EB and DHT. The C–H activation barriers of EB catalysed by complexes 1 and 2 are 12.0 and 9.2 kcal mol^{-1}, respectively, which is significantly higher than the activation barrier of the same complexes with DHT 7.5 kcal mol^{-1} and 3.6 kcal mol^{-1}. This finding is anticipated as EB has high bond dissociation energy (85.4 kcal mol^{-1}) compared to DHT (77 kcal mol^{-1}).[73,74] The computed BDE values for EB and DHT, 84.2 kcal mol^{-1} and 75.2 kcal mol^{-1}, respectively, are also in close proximity to the previously reported experimental BDE values. To further demonstrate the effect of sequential carboxylate ligation at the equatorial position, the potential energy surfaces for H-abstraction from EB catalyzed by complexes 3 and 4 are illustrated in Fig. 5.6.

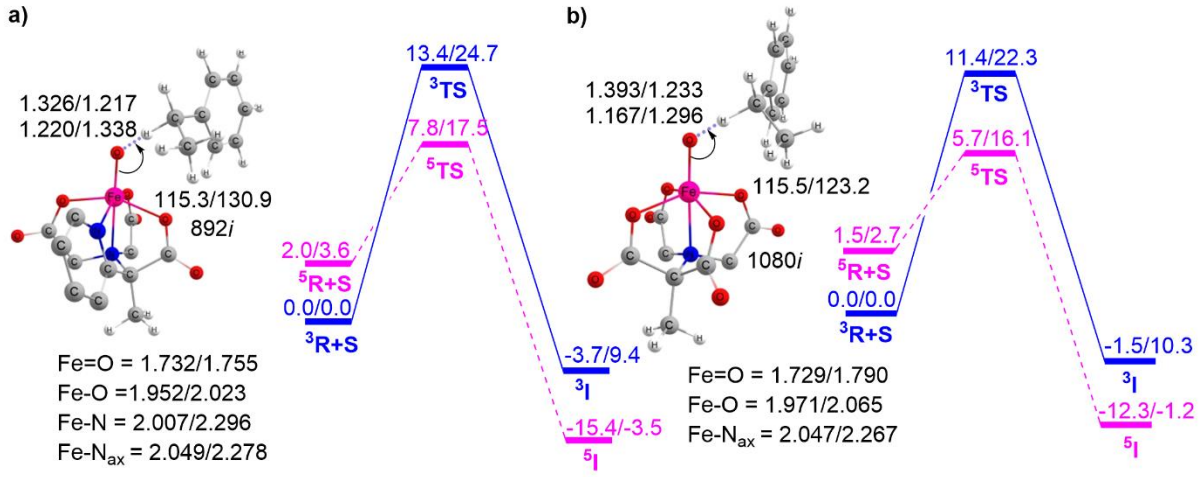

Fig. 5.6 The potential energy profile computed for C–H activation reactions (a) 3+EB (b) 4+EB, with the associated transition states. The energies are represented as ΔE (B2+ZPE)/ ΔG

(B2+ G^{corr}_{298K}) in kcal mol^{-1}. Both triplet/quintet spin state geometric parameters are provided along with the lengths and angles expressed in angstroms and degrees, respectively.

Fig. 5.5, and 5.6 clearly show that enhancing carboxylate ligation at the equatorial position of the Fe(IV)O complexes provides the sequential reduction of the energy of activation. The corresponding pattern is as follows: 1 (12.0 kcal mol^{-1}) < 2 (9.2 kcal mol^{-1}) < 3 (7.8 kcal mol^{-1}) < 4 (5.7 kcal mol^{-1}). We can now investigate the factors that provide this new finding of increased C-H activation reactivity in carboxylate-ligated Fe-oxo complexes.

5.3.4: Steric Factor

The free space related to the H-atom abstractor (Fe=O) being accessible to the substrates is detailed in Table 5.2, available in the supporting information.

Table 5.2 Calculated % volume buried and % free space for oxidants computed on the geometry optimized at B1 level of theory.

Oxidants	Spin state	% Volume buried	% Free space
1	*S*=1	92.4	7.6
	S=2	91.4	8.6
2	*S*=1	87.1	12.9
	S=2	86.9	13.1
3	*S*=1	86.5	13.5
	S=2	84.2	15.8
4	*S*=1	84.6	15.4
	S=2	81.9	18.1

The free space values—8.6%, 13.1%, 15.8%, and 18.1% for complexes 1, 2, 3, and 4, respectively—suggest that the sequential addition of ligand carboxylate groups at the equatorial position increases the accessibility of the abstractor to the substrate. Fig. 5.7's plot of activation energy against the percentage of free space shows a strong linear relationship, with an R^2 value close to unity (0.985). This indicates with certainty that the steric factor can enhance reactivity in line with the increase in carboxylate groups.

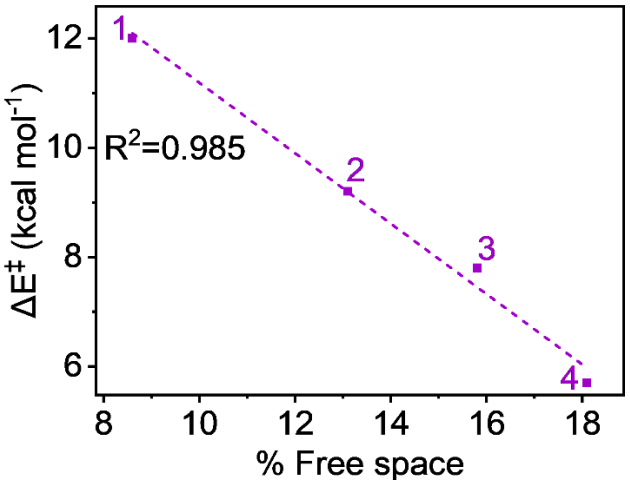

Fig. 5.7 Plot of activation energy ($\Delta E^{\ddagger}$) vs % free space at S=2 pathway for all complexes.

Therefore, % free space affects how easily the substrate can approach the reactive Fe=O center; increased space reduces steric hindrance, thereby lowering the activation barrier.

5.3.5: Distortion Energy

Next, we analyse the distortion energy required to reach the transition states, as this significantly contributes to the activation energy. The corresponding values have been collected in Table 5.3 presented below.

Table 5.3 The distortion energy ($\Delta E^{\ddagger}_{dis}$) in kcal mol^{-1}, along with the substrate's (ΔS) and oxidant's (ΔO) contribution.

Reaction	Spin states	ΔS	ΔO	$\Delta E^{\ddagger}_{dis}$
1+EB	*S*=1	13.1	5.2	18.4
	S=2	8.4	6.0	14.4
2+EB	*S*=1	10.2	4.0	14.2
	S=2	5.1	6.1	11.2
3+EB	*S*=1	7.8	4.2	12.0
	S=2	2.5	6.9	9.4
4+EB	*S*=1	6.1	4.1	10.2
	S=2	1.4	5.6	7.0

The values demonstrate that the distortion energies for complex 1 is 14.4 kcal mol^{-1} and it decreases sequentially for 2 (11.2 kcal mol^{-1}), 3 (9.4 kcal mol^{-1}), and 4 (7.0 kcal mol^{-1}) complexes. Notably, the deformation energy of the oxidant is not significant, whereas the

substrate distortion mainly contributes to the total distortion energy, decreasing progressively from complex 1 to complex 4. The distortion energy values also show an excellent correlation with the pattern of energy of activation of the reaction. The plot in Fig. 5.8 shows a remarkable linear correlation between the activation energy and distortion energy, with an R^2 value close to unity. We can therefore conclude that the qualitative control of reactivity can be attributed to the distortion energy.

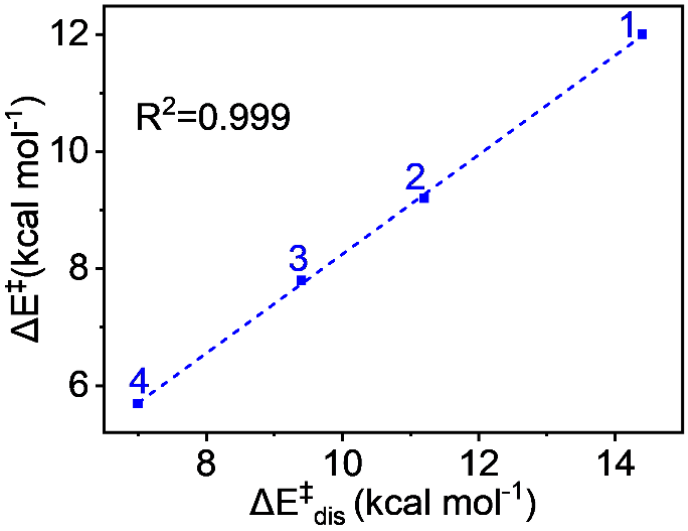

Fig. 5.8 Plot of activation energy ($\Delta E^{\ddagger}$) vs distortion energy ($\Delta E_{dis}{}^{\ddagger}$) for the *S*=2 pathway for all complexes.

Hence, distortion energy reflects the structural strain required to reach the transition state; lower distortion energies suggest a more favourable reaction pathway with less energetic cost.

5.3.6: Electrophilicity of the Central Metal Fe

The hydrogen atom transfer mechanism essentially involves an electron transfer process from the substrate to the central iron metal. Therefore, it is appropriate to examine the atomic charge on Fe, as it directly reflects the electrophilicity of the metal within the ligand framework of complexes 1 to 4, and relates to the reaction barrier. The natural charges, computed using the NBO method, show a continuous increase with carboxylate ligation as follows: 0.841, 0.861, 0.884, and 0.894 from 1 to 4, respectively. This trend is logical because oxygen, being more

electronegative than nitrogen, attracts more electron density from the metal. A plot of charge versus activation barrier, shown in Fig. 5.9, also provides a linear correlation, indicating that the metal's electrophilicity may control the reactivity.

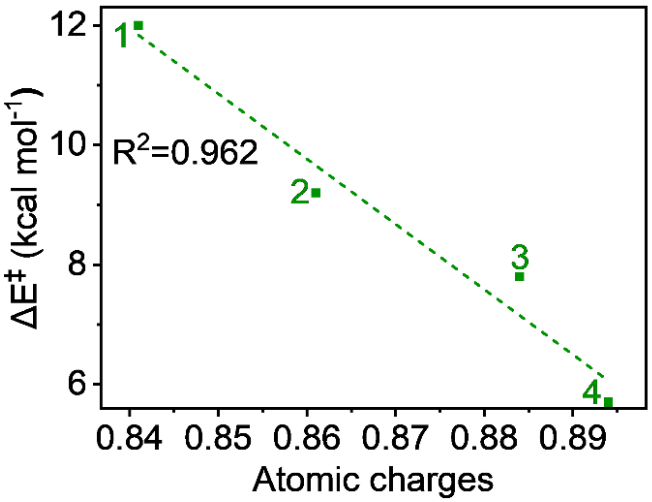

Fig. 5.9 Plot of activation energy ($\Delta E^{\ddagger}$) vs. atomic charges (in au) for the *S*=2 pathway for all complexes.

The electrophilicity of the central Fe, indicated by the increasing positive charge, enhances its ability to accept electron density during the HAT process, thereby facilitating the reaction.

5.3.7: Triplet-Quintet Energy Difference

Since the reaction follows the two-state reactivity (TSR) model, the spin inversion probability is significant and plays a crucial role in understanding surface crossing phenomena. The probability of spin inversion is influenced by the energy gap (ΔE_{T-Q}) between the *S*=1 ground state and the *S*=2 excited state oxidants. Smaller ΔE_{T-Q} values generally increase the probability of spin inversion because the spin states are closer in energy, making transitions more feasible. The outcome indicates that the ΔE_{T-Q} values continuously decrease from 1 to 4 due to carboxylate ligation as follows: 6.5, 2.9, 2.0, and 1.5 kcal mol^{-1} for 1 to 4, respectively, which facilitates a higher probability of spin inversion. Fig. 5.10 shows the plot of the energy of activation and the energy gap between spin states shows quite a linear correlation with

R^2=0.979, which supports the TSR model's prediction that spin inversion probability increases with decreasing energy gaps, aligning with the observed data.

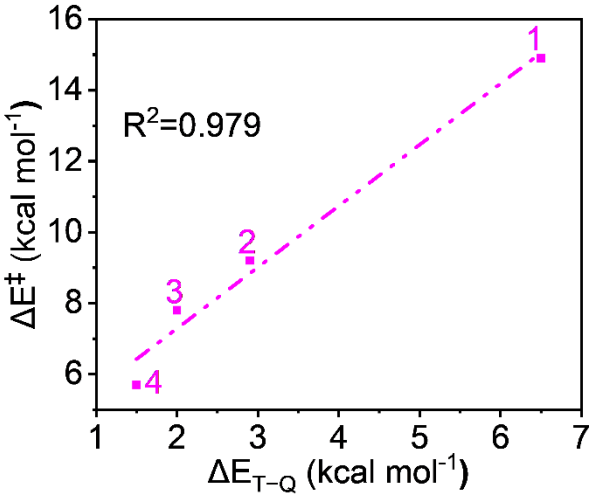

Fig. 5.10 A Plot of activation energy ($\Delta E^{\ddagger}$) vs. the triplet−quintet energy difference (ΔE_{T-Q}).

From the aforementioned discussion, it is evident that all reactivity-controlling factors contribute to the increased reactivity of the carboxylate-rich complexes, providing a comprehensive explanation for the overall reactivity.

5.3.8: Quantum Mechanical Tunneling

As several studies[42,45,46,55-58,75] have reported that hydrogen tunneling can be an important factor in metal-oxo-catalyzed C-H activation, we have conducted similar computations here, with the results presented in Table 5.4.

Table 5.4 The imaginary frequencies of the TS ($\nu^{\ddagger}_H$), transmission coefficients for H (κ_H) and D (κ_D), KIE at 298 K, tunneling correction ($\Delta\Delta E^{\ddagger}_{tun}$, kcal mol^{-1}), classical barrier ($\Delta E^{\ddagger}/\Delta G$, kcal mol^{-1}) and tunneling-corrected activation barrier ($\Delta E^{\ddagger}$–$\Delta\Delta E^{\ddagger}_{tun}$, kcal mol^{-1}) at the B2 + ZPE level and the tunneling contribution (%tunneling) of the overall reaction for all the reactions.

Reactions	Spin state	$\nu^{\ddagger}_H$	κ_H	κ_D	KIE_{Eck} (298K)	$\Delta\Delta E^{\ddagger}_{tun}$	$\Delta E^{\ddagger}/\Delta G$	$(\Delta E^{\ddagger}/\Delta G)$-$\Delta\Delta E^{\ddagger}_{tun}$	%tunneling
1+EB	*S*=1	1832	154.27	12.17	66.0 (44)[a]	3.0	14.9/26.3	11.9/23.3	98.5
	S=2	1281	7.33	3.16	11.6	1.2	12.0/21.5	10.8/20.3	91.5
2+EB	*S*=1	1571	22.57	5.23	22.4	1.8	14.2/25.8	12.4/24	95.6
	S=2	842	2.16	1.74	4.6	0.5	9.2/18.6	8.7/18.1	78.3

3+EB	*S*=1	1854	102.36	11.69	52.5	2.7	13.4/24.7	10.7/22	98.1
	S=2	892	2.41	1.76	6.3	0.5	7.8/17.5	7.3/17	84.1
4+EB	*S*=1	1801	67.14	10.06	46.1	2.5	11.4/22.3	8.9/19.8	97.8
	S=2	1080	3.42	2.09	9.9	0.7	5.7/16.1	5/15.4	89.9
1+DHT	*S*=1	1677	45.71	7.38	34.1	2.3	10.5/22.3	8.2/20	97.1
	S=2	910	2.40	1.81	5.7	0.5	7.5/17.1	7/16.6	82.5
2+DHT	*S*=1	1282	5.77	2.85	10.5	1.0	9.9/21.0	8.9/20	90.5
	S=2	824	1.93	1.64	4.6	0.4	3.6/13.0	3.2/12.6	78.3

[a]KIE in the parenthesis are computed at 313K to compare with experiment[75]

The experimentally reported KIE is approximately 45 at 313 K, which closely matches our calculated KIE (44) when considering the *S*=1 pathway. It is important to note that the kinetic isotope effect can also indicate the reactive spin state[46,53,75], suggesting that the reaction of EB with 1 likely proceeds via the *S*=1 state. Energetically, both pathways appear almost degenerate after tunneling correction ($\Delta E^{\ddagger}$ = 11.9 and 10.8 kcal mol^{-1} for the *S*=1 and *S*=2 paths, respectively). This prediction is consistent with earlier research[46]. For other reactions, we have no data for comparison, but the tunneling-corrected barrier for the *S*=2 pathway appears significantly lower compared to the *S*=1 pathway, suggesting the reactive state is likely *S*=2. Considering the tunneling-corrected activation energy ($\Delta E - \Delta\Delta E^{\ddagger}_{tun}$) presented in column 8 of Table 5.4, it is clear that the reactivity pattern remains consistent with the classical trend as discussed earlier, regardless of the spin state considered for 1+EB. The experimental observation of higher reactivity in complex 2 compared to complex 1 is also replicated here, along with a suitable explanation.

The % tunneling results in Table 5.4 also demonstrate a significant contribution of tunneling to the C–H activation reactivity facilitated by the Fe-oxo complexes. Notably, tunneling accounts for over 98% of the total reactions, except for 2 + EB and 2 + DHT, where it still accounts for over 78%.

5.4: Conclusion

Several significant conclusions can be drawn from this extensive DFT investigation, including

insights into the C-H activation reactivity of the non-heme Fe(IV)O complex linked with a carboxylate-rich macrocycle. In this study, four Fe(IV)O oxidants were examined, starting with the macrocycle N4Py ligand and sequentially replacing pyridine groups with carboxylates to produce three additional oxidants. The complexes of oxidant 2, containing the ^{n}Bu-P2DA macrocyclic ligand, were previously synthesized and exhibited higher reactivity than complex 1. Two more oxidants (3 and 4) were designed by further replacing pyridine with carboxylate groups.

Regarding C-H activation reactivity, a noteworthy pattern is observed: 1 < 2 < 3 < 4, indicating that reactivity increases with the addition of equatorially enriched carboxylate groups. These findings are in excellent agreement with available experimental results for complexes 1 and 2. Several important insights into this reactivity pattern were identified, including: spin inversion probability: accessibility of the *S*=2 state decreases with carboxylate enrichment, free space for the abstractor: increases in carboxylate-rich macrocyclic complexes, deformation energies: consistently decrease from 1 to 4, and electrophilicity of the metal centre. Hydrogen tunneling contributes in each case but does not significantly influence the observed reactivity pattern. This investigation establishes that enhancing carboxylate content on C-H activation reactivity should encourage the bioinorganic community to synthesize more oxidants with carboxylate-rich ligated macrocyclic compounds.

CHAPTER 6

Computational Insights into Hydrogen Atom Transfer Mediators in C-H Activation Catalysis of Nonheme Fe(IV)O Complexes

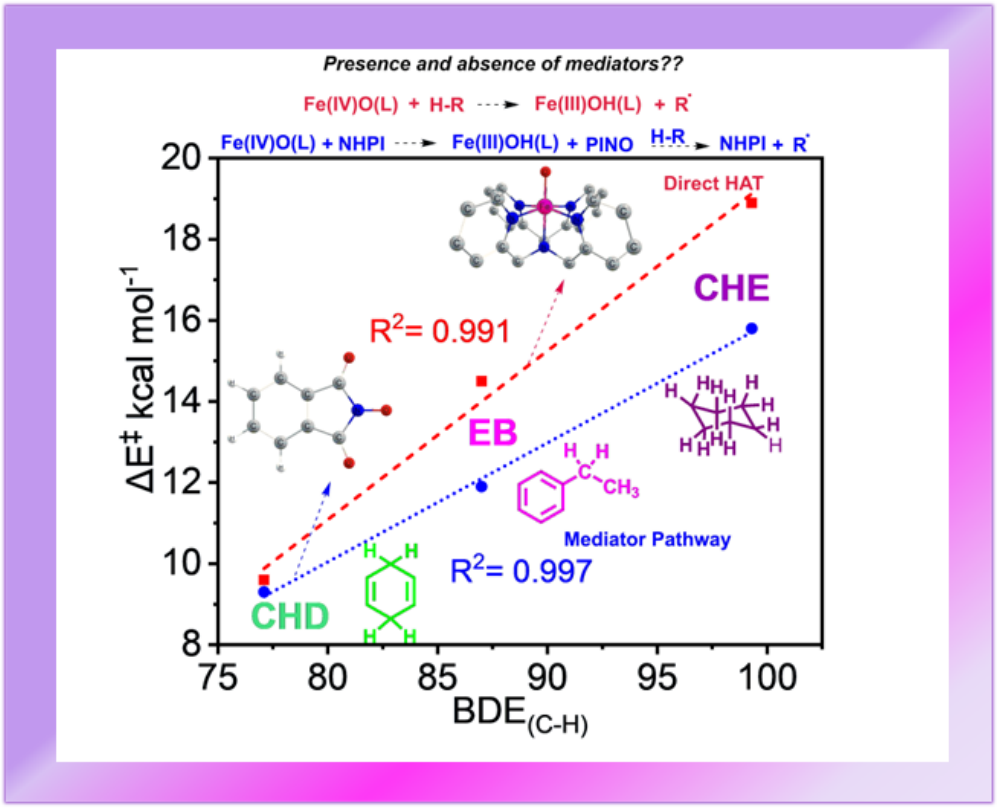

6.1: Introduction

The synthetic mimics of cofactors in oxidative metalloenzymes are primarily high-valent transition metal oxo-species.[1-6] These analogues effectively catalyze a wide range of organic and biotransformation reactions, particularly in C-H bond activation and oxygen atom transfer processes.[7-11] Numerous experimental, spectroscopic, and computational methods have been employed to understand the chemical and physical characteristics and mechanistic reactivity patterns of these species.[12-16] In this field, the high-valent Fe(IV)-oxo species, in particular, has garnered considerable attention and due to their relatively high stability, several Fe(IV)-oxo compounds with various ligand macrocycles have already been synthesized.[17-21]

These Fe(IV)-oxo complexes are generally capable of activating weak C-H bonds, and significant efforts such as the synthesis of reactive *S*=2 complexes, modification of geometry,[22,23] ligand architecture, etc.,[24-28] have been dedicated to improving their reactivity and selectivity. In the past few years, an approach using redox mediators as cocatalysts for C-H activation alongside Fe(IV)-oxo complexes has been gaining significant attention.[29-32] Recently, Barbieri *et. al.,*[29] showed that in the presence of a redox activator e.g., *N*-hydroxyphthalimide (NHPI), the rate of $[Fe(IV)O(N4Py)]^{2+}$ catalyzed C-H activation can be enhanced. NHPI is an effective catalyst for the oxidation of various organic compounds, such as aliphatic and alkyl aromatic hydrocarbons, alcohols, amides, and amines.[33-36] It generates the phthalimide-N-oxyl (PINO) radical, which is responsible for the crucial hydrogen atom transfer (HAT) reactions during the oxidation process. NHPI has also been found advantageous in various other reactions such as the oxidation of alcohols by Fe-oxo complexes $[Fe(bpc)Cl_2][Et_4N]$ and $[Fe(Me_2bpb)Cl_2][Et_3NH]$ in the presence of t-BuOOH.[32] As proposed the C-H activation mechanism catalyzed by $[Fe(IV)O(N4Py)]^{2+}$ in the presence of NHPI is shown below in Scheme 6.1.[29]

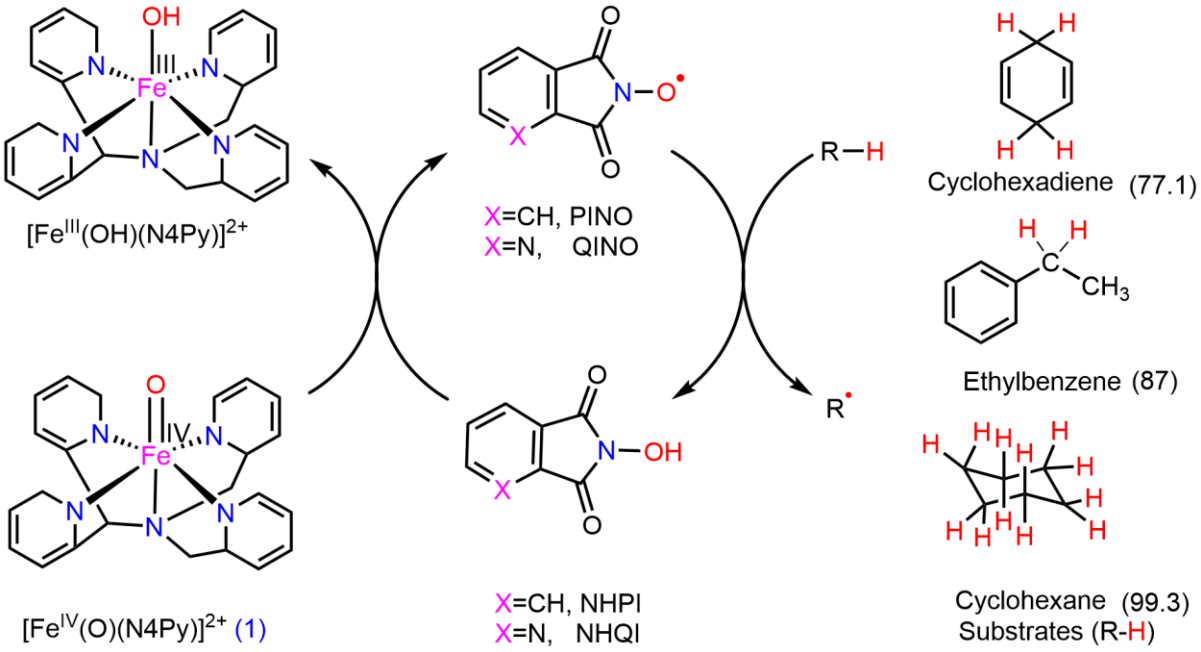

Scheme 6.1 HAT from hydrocarbons promoted by $[Fe^{IV}(O)(N4Py)]^{2+}$ (1) in the presence and absence of mediators and also the investigated substrates and their experimental BDE (C-H) in bold (in kcal mol^{-1}).

As shown in Scheme 6.1, $[Fe^{IV}(O)(N4Py)]^{2+}$ (1) first reacts with NHPI to produce the reactive radical PINO, which then abstracts a hydrogen atom from the substrate leading to the regeneration of the mediator in its reduced state. The hydrocarbon radical then goes through a rebound of –OH from the $[Fe(III)OH(N4Py)]^{2+}$ complex, providing the final product.

Although the mechanism of direct C-H activation catalyzed by *N*-oxyl radicals or by complex 1 has been extensively studied over the past several decades,[33,37-49] there is a lack of significant research on how and why NHPI can facilitate iron-oxo-catalyzed C-H activations. In line with this, a comprehensive density functional theory (DFT) investigation has been conducted to determine the insight into the enhancement of rate and validate the aforesaid mechanism. The nonheme complex 1, along with a series of substrates with varying bond dissociation energies, such as cyclohexadiene (CHD), ethylbenzene (EB), and cyclohexane (CHE), has been used. Additionally, another reactive mediator, NHQI, which is formed by replacing the phenyl group with an electron-withdrawing *N*-heteroaromatic ring, is also utilized in this study.[50] This

investigation includes a careful analysis of other crucial factors that influence the reactivity, such as electronic properties, distortion energy, and hydrogen tunneling.

6.2: Computational Details

The calculations associated with geometry optimization, frequency analysis, and thermochemistry were conducted using the DFT-B3LYP method. B3LYP, a method developed by Becke-Lee-Yang-Parr, is found to be one of the best DFT functionals for this type of typical problem.[13,14,51-53] To further validate our results, some other DFT methods, e.g., M06-L and TPSSH, have also been brought into practice, as these have been reported to be the most suitable functionals in this type of system as presented in Table 6.1.[53-54]

Table 6.1 The relative energies and free energies at 298K (kcal mol^{-1}) for all the species involved in the investigated reactions at different functionals (as listed in the table) are computed at B2 level of theory.

			TPSSH		M06-L		B3LYP
Reactions	Spin state	Species	B2+ZPE(B1)	B2+ G_{298K}(B1)	B2+ZPE(B1)	B2+ G_{298K}(B1)	B2+ G_{298K}(B1) + E_{dis}(B1)
1-EB	*S*=1	^{3}RC	0.0	0.0	0.0	0.0	0.0
		^{3}TS	15.5	18.9	15.3	18.8	16.7
		^{3}IH	0.6	2.2	3.8	5.4	-5.2
	S=2	^{5}RC	7.9	5.9	10.0	7.9	5.5
		^{5}TS	14.5	16.0	16.3	17.8	7.6
		^{5}IH	0.4	-0.2	5.8	5.2	-12.9
1-NHPI	*S*=1	^{3}RC	0.0	0.0	0.0	0.0	0.0
		^{3}TS	5.0	6.8	5.9	7.7	8.5
		^{3}IH	1.2	2.4	2.9	4.2	3.2
PINO-EB	*S*=1/2	^{2}RC	0.0	0.0	0.0	0.0	0.0
		^{2}TS	11.0	13.8	12.3	14.9	14.5
		^{2}IH	5.9	7.1	6.7	7.8	5.1
1-CHE	*S*=1	^{3}RC	0.0	0.0	0.0	0.0	0.0
		^{3}TS	21.0	25.5	23.1	27.6	19.7
		^{3}IH	14.1	16.0	16.9	18.8	8.5
1-NHPI	*S*=1	^{3}RC	0.0	0.0	0.0	0.0	0.0
		^{3}TS	5.0	6.8	5.9	7.7	8.5
		^{3}IH	1.2	2.4	2.9	4.2	3.2

PINO-CHE	*S*=1/2	^{2}RC	0.0	0.0	0.0	0.0	0.0
		^{2}TS	15.2	18.2	16.6	19.6	16.6
		^{2}IH	14.5	17.2	15.5	18.2	15.7
1-CHD	*S*=1	^{3}RC	0.0	0.0	0.0	0.0	0.0
		^{3}TS	10.0	12.3	10.6	12.9	10.4
		^{3}IH	-12.8	-13.2	-7.1	-7.5	-6.9
1-NHPI	*S*=1/2	^{2}RC	0.0	0.0	0.0	0.0	0.0
		^{2}TS	5.0	6.8	5.9	7.7	8.5
		^{2}IH	1.2	2.4	2.9	4.2	3.2
PINO-CHD	*S*=1	^{3}RC	0.0	0.0	0.0	0.0	0.0
		^{3}TS	4.1	8.3	2.1	6.3	9.8
		^{3}IH	-6.9	-4.9	-8.9	-6.9	-4.3
1-NHQI	*S*=1	^{3}RC	0.0	0.0	0.0	0.0	0.0
		^{3}TS	0.4	1.7	2.7	4.1	5.3
		^{3}IH	-3.6	-4.0	-0.7	-1.1	-5.0
QINO-EB	*S*=1/2	^{2}RC	0.0	0.0	0.0	0.0	0.0
		^{2}TS	10.3	12.9	12.3	14.9	13.6
		^{2}IH	5.1	6.2	6.7	7.8	6.1

*B2 is 6-31++G(2d,2p)(for all atoms)/SDD basis set and ECP(Fe)

Pople's split valence double-ζ 6-31G* basis set[55] is used for all nonmetal atoms, and the LANL2DZ basis set[56] along with its associated electrostatic potential, is used for Fe. In our presentation, this particular theoretical framework is classified as B1. In order to minimize undesirable self-interaction errors, present in DFT, the overall positive charge of the systems was effectively neutralized by counterion ClO_4^-.[57] The counterions are positioned in a way that ensures their role is limited to system neutralization, without influencing the reaction directly. To address this, we conducted several attempts to determine the optimal placement of counterions, ensuring no interference with the reaction. The most suitable orientation, as determined, is shown in Fig. 6.1.

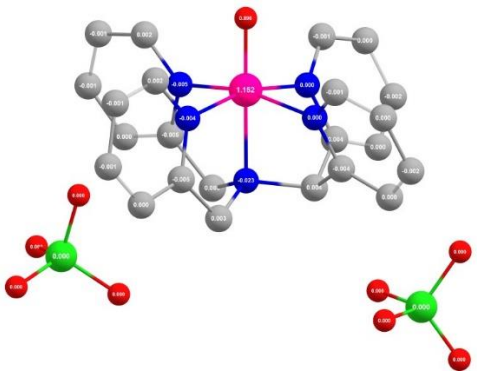

Fig. 6.1 Depiction of placement of counter ions in complex 1

To verify the transition states, vibrational frequency computations have been performed at the same level B1, where the presence of a single imaginary frequency indicates a transition state, and the absence of any imaginary frequencies denotes minima. At 298 K, the temperature and entropic changes in the Gibbs free energy were calculated.

The energies have been further refined by performing the single-point energy calculations using the triple-ζ valence polarized 6-311++G(2d,2p) basis set for all atoms, and the SDD-ECP basis set for Fe.[58] Dispersion correction employing the D3 version of Grimme's dispersion with Becke-Johnson damping (GD3BJ) has also been performed in the B1 level of theory. The impact of the acetonitrile (CH_3CN) solvent is also implicitly considered by employing the self-consistent reaction field (SCRF)[59] approach, using Truhlar's solvation model density approximation (SMD).[60] This level of theory is designated as B2 here. All the aforementioned computations have been performed using the Gaussian 16 software.[61] To precisely determine the electronic states the parameters including spin densities, Mulliken charges, and natural spin orbitals were obtained. The Chemcraft software was employed to analyze results, visualize data, and draw images.[62]

6.3: Tunneling Corrections and Kinetic Isotope Effect (KIE) Calculations

The rate constants have been calculated using Eyring's transition state theory[63] (Eq. 6.1).

$$k = \kappa\sigma \frac{k_b T}{h} \exp\left(-\frac{\Delta G^{\ddagger}}{RT}\right) \qquad \text{Eq. 6.1}$$

The symbols κ and σ are used to represent the transmission coefficient and reaction symmetry, respectively. The calculation of tunneling was conducted via the one-dimensional asymmetric Eckart method.[64] The impact of the transmission coefficient on the barrier was calculated by applying the formula in Eq. 6.2.

$$\Delta\Delta E^{\ddagger}_{tun} = -\,RT \ln \kappa\,(T) \qquad \text{Eq. 6.2}$$

Here, $\Delta\Delta E^{\ddagger}$ signifies the quantitative reduction in the activation barrier resulting from

tunneling, R represents the universal gas constant and T denotes the absolute temperature, The quantum mechanical tunneling corrected deuterium kinetic isotope effect ($\frac{k_H}{k_D}$) was also computed for all the investigated reactions. All the kinetics calculations were performed by utilizing the kisthelp2019 program.[65]

The tunneling contribution for a reaction can be contributed using Eq. 6.3:[66]

$$\% \text{ tunneling} = 100[(\kappa_{Eckart} - 1)/ \kappa_{Eckart}] \text{ ------- Eq. 6.3}$$

Here, κ_{Eckart} denotes the transmission coefficient in equation 6.1, which is determined by using the Eckart method. Consequently, the numerator in equation 6.3 reflects the difference between a reaction that includes tunneling and one where the transmission coefficient is unity, $\kappa = 1$, indicating no tunneling effect. Therefore, the ratio $[\kappa_{Eckart} - 1)/ \kappa_{Eckart}]$ quantifies the extent of tunneling contribution.

Further, distortion energies to achieve the transition states are computed using the following equation:[67]

$$\Delta E^{\ddagger}_{dist} = (E^{\ddagger}_S + E^{\ddagger}_O) - (E_S - E_O) \text{ ------- Eq. 6.4}$$

The substrate and oxidant equivalents are specified by the subscripts S and O, respectively. Here, E_S and E_O are defined as the energies of the substrate and oxidant in their undistorted state, whereas $E^{\ddagger}_S$ and $E^{\ddagger}_O$ are the single-point energies of the separated substrate and oxidant fragments in the transition state, respectively.

6.4: Result and Discussion

6.4.1: Spin-State Preferences

In C-H activation, many Fe(IV)-oxo complexes exhibit two-state reactivity (TSR) due to the presence of closely spaced triplet (*S*=1), characterized by two unpaired electrons, and quintet (*S*=2), characterized by four unpaired electrons, spin states.[68,21] Since the hydrogen atom transfer (HAT) is the rate-determining step (RDS) of these reactions, the primary H/D kinetic isotope effect (KIE) can serve as an indicator of the reactive spin state and it can be determined

by the comparison between experimental and computed KIEs.[69] The calculated KIE for the reaction of 1 with EB at 313 K (54.5) provides close agreement with the experimentally obtained value (45±2), whereas the calculated value for *S*=2 (~10) is far away from the experiment.[70,71] In an earlier investigation, the *S*=1 state KIE (47) also shows excellent agreement with the experiment, but not *S*=2 (~12).[72] Consequently, for the reaction of complex 1, only *S*=1 state energetics will be considered for the discussion unless otherwise specified.

6.4.2: Reactivity

In this section, we have analyzed the C-H activation reactivity of complex 1 using three different substrates (EB, CHE, and CHD) directly and via NHPI and NHQI-mediated pathways. The potential energy surface for the reaction of 1+EB in the absence and presence of NHPI and NHQI has been presented in Fig. 6.2. For the discussion, first we look for the direct H-abstraction and then the mediator pathways.

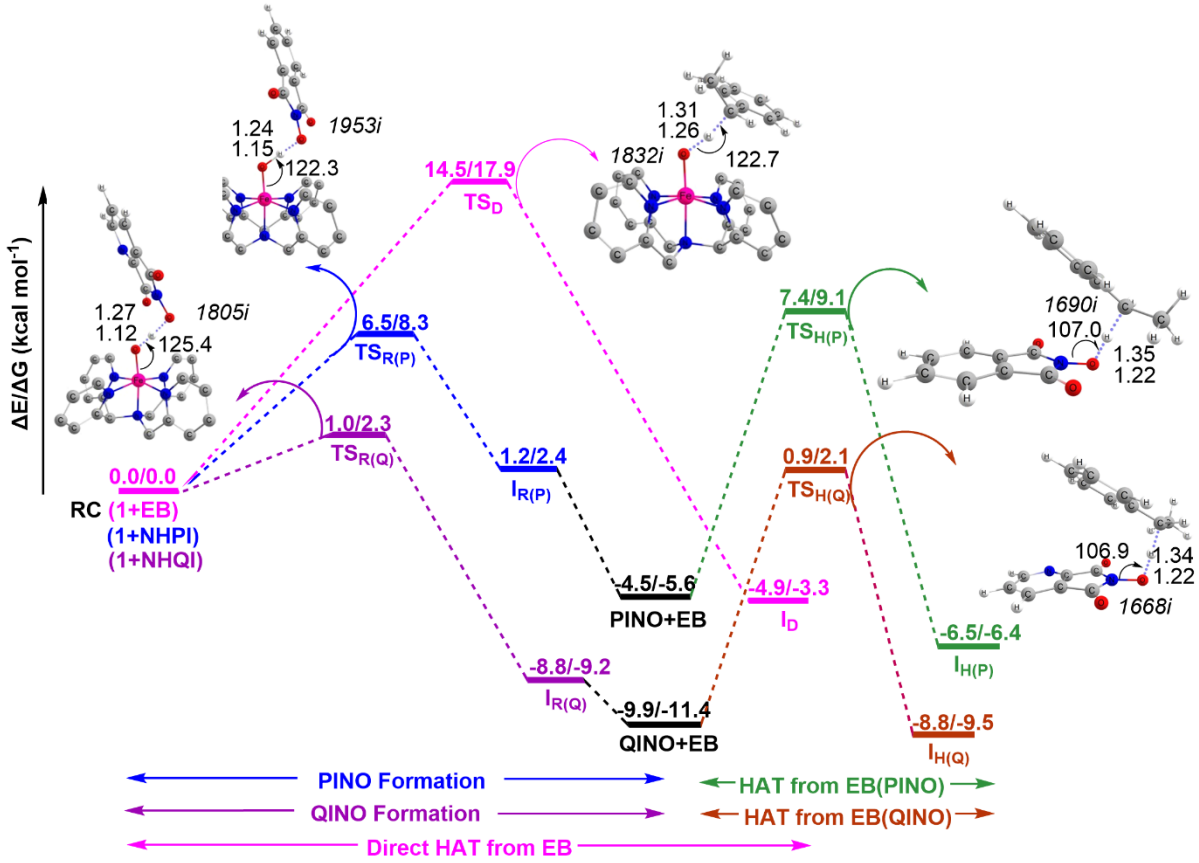

Fig. 6.2. Potential energy profile (kcal mol^{-1}), transition state structures with geometrical parameters (bond length in Å and angle in degrees), and imaginary frequencies for the C-H activation reaction of EB directly catalyzed by complex 1 and through the formation of PINO and QINO radicals. The energies are given as B2+ZPE/B2+G^{corr}_{298K}, using B3LYP as the functional.

Fig. 6.2 illustrates that the direct H-abstraction from EB by complex 1 (pink) has an activation energy of 14.5 kcal mol^{-1}, while the barrier for HAT from NHPI (blue) is only 6.5 kcal mol^{-1}. This indicates that generating the PINO radical is significantly easier than H-abstraction from EB, suggesting that cleaving the O-H bond is easier than the C-H bond, even though their bond dissociation energies are nearly the same (~88 kcal mol^{-1} for O-H and ~85 kcal mol^{-1} for C-H).[33] In the current theoretical prediction, the O−H BDE in NHPI is found slightly lower (~84 kcal mol^{-1}) which is consistent with earlier reports.[73]

The PINO abstracts a hydrogen atom from EB through the transition state TS_H, with activation energy of 7.4 kcal mol^{-1}, which is higher than that of the first step in the mediated mechanism. Similar, to the direct pathway, the hydrogen atom transfer (HAT) from the substrate is the rate-determining step in the PINO-mediated pathway as well. This observation is consistent with previously reported NHPI-mediated oxidation of alcohols.[33] Comparing the RDS of both steps, it is clear that the reaction gets benefited by 2.6 kcal mol^{-1} if it follows the mediator pathways. To ensure the robustness of this 2.6 kcal mol^{-1} difference, we also compared the results using different functionals, specifically TPSSH and M06-L as suggested by a benchmark study.[53] The results obtained (shown in Table 6.2) show a similar trend, further emphasizing our outcome.

Table 6.2 RDS calculation at different functionals (as listed in the table) where optimisation is done using SDD for Fe and 6-31++G(2d,2p) for rest of the atoms.

Complex	B3LYP	M06-L	TPSSH
1+EB	2.6 kcal mol^{-1}	3 kcal mol^{-1}	4.5 kcal mol^{-1}

To further validate the mechanism and the role of the mediator, the investigations were extended to two additional substrates: cyclohexane (CHE), with a very high bond dissociation energy (BDE) of approximately 99 kcal mol^{-1}, and cyclohexadiene (CHD), with a lower BDE of around 78 kcal mol^{-1}. The potential energy surfaces (PES) for the oxidation of CHE and CHD are shown in Fig. 6.3 and 6.4.

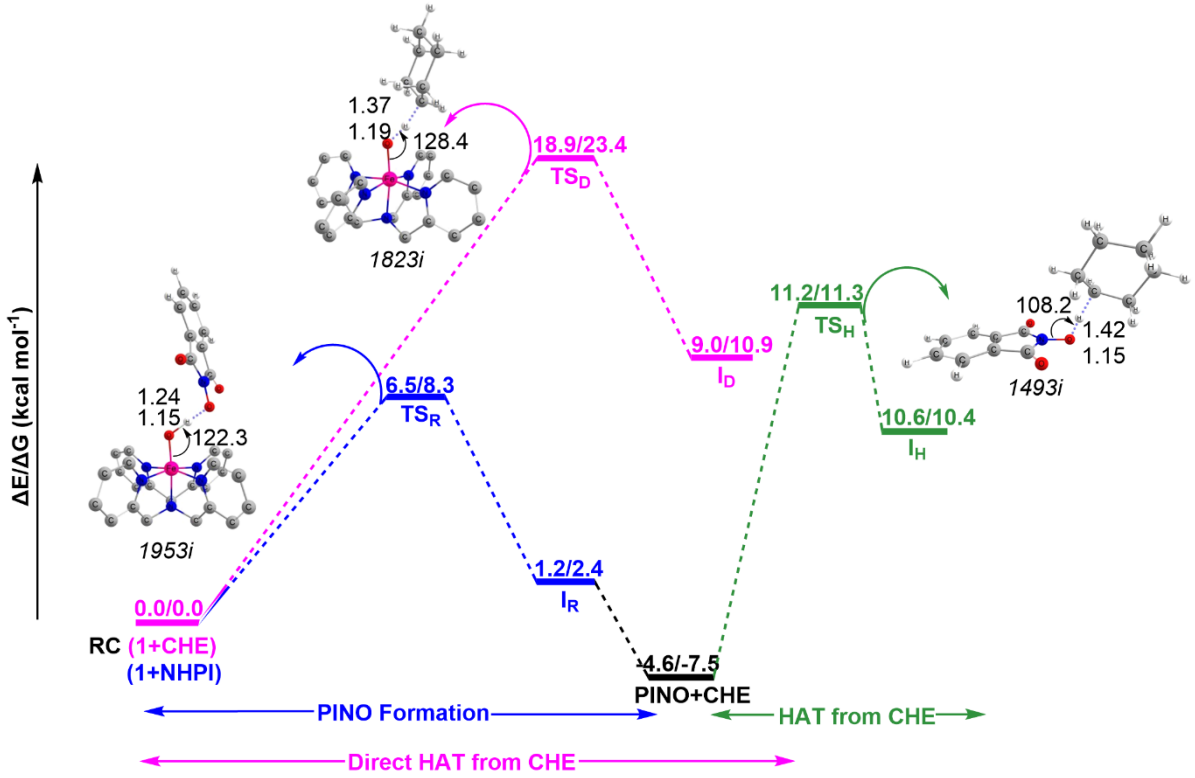

Fig. 6.3 Potential energy profile for the direct and mediator C-H activation pathways of CHE by complex 1 and through PINO formation, geometry of the transition states, imaginary frequency, and geometrical parameters (bond length in Å and angle in degree). The energies (kcal mol^{-1}) are given as B2+ZPE/B2+G^{corr}_{298K}, using B3LYP as the functional.

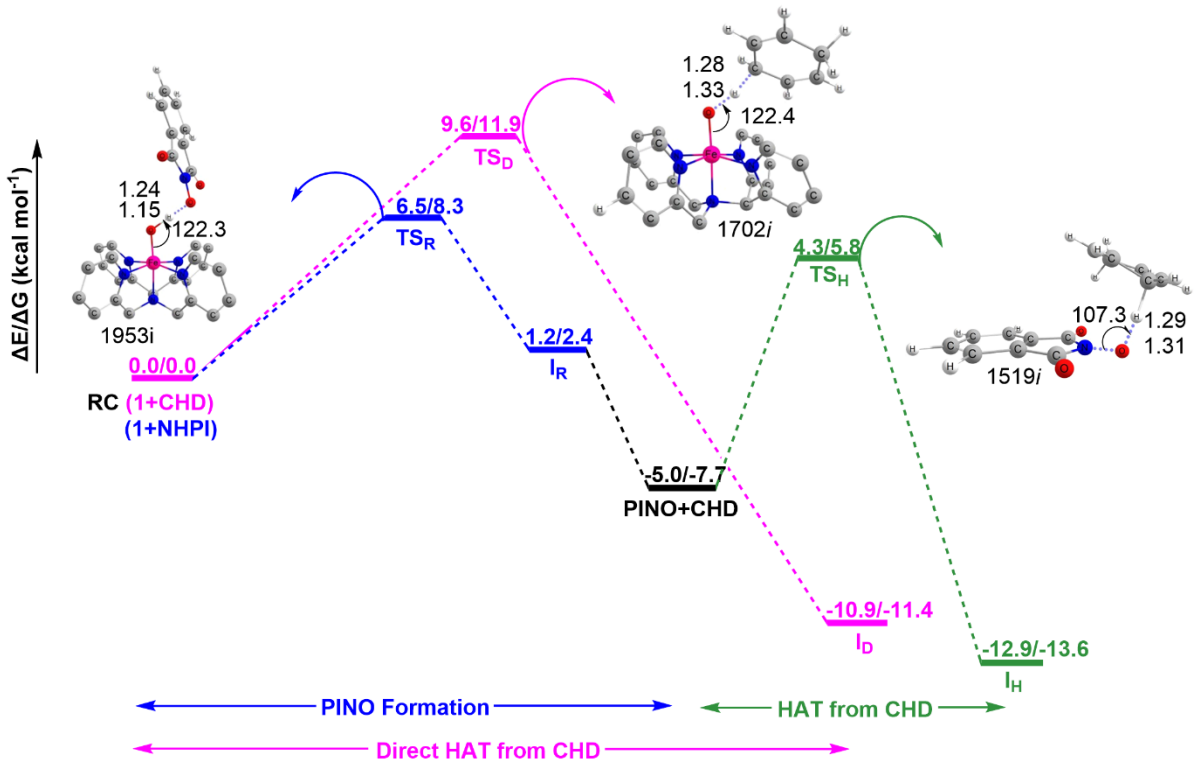

Fig. 6.4 Potential energy profile for the direct and mediator C-H activation pathways of CHD by complex 1 and through PINO formation, geometry of the transition states, imaginary frequency, and geometrical parameters (bond length in Å and angle in degree). The energies (kcal mol^{-1}) are given as B2+ZPE/B2+G^{corr}_{298K}, using B3LYP as the functional.

The activation barrier for CHE is higher than that for EB throughout the reaction, with a reduction of 3.1 kcal mol^{-1} in the NHPI-mediated pathway. For CHD, all barriers, as depicted in Fig. 6.4, are lower compared to those for EB and CHE. Interestingly, for CHD, the mediator's efficiency is notably reduced, with the activation energy lowered by only 0.3 kcal mol^{-1} by NHPI. This is due to the fact that the barrier height decreases more sharply with BDE in the direct pathway compared to the radical-mediated pathway as shown in the Fig. 6.1.

The investigation has also focused on identifying a more efficient mediator, specifically NHQI, which has been shown to exhibit a significantly higher hydrogen atom transfer (HAT) rate compared to NHPI, as reported in previous studies.[36,50] The associated potential energy surface for the substrate ethylbenzene (EB) is also illustrated in Fig. 6.1.

According to Fig. 6.1 (purple line), the H-abstraction from NHQI is highly favorable, with a remarkably low energy barrier of approximately 1.0 kcal mol^{-1}. The subsequent rate-determining step (RDS), involving HAT from EB, proceeds with an activation energy of about 10.8 kcal mol^{-1}. This makes the pathway involving the NHQI mediator more favorable by 3.7 kcal mol^{-1} compared to alternative pathways. Thus, in the context of EB, the NHQI mediator demonstrates a superior efficiency over NHPI, with an overall energy advantage of 1.1 kcal mol^{-1}. So, from the aforementioned analysis it is clear that the reactivity of the Fe(IV)O complex has significantly enhanced in the presence of a mediator than in the absence of a mediator.

The C-H bond cleavage adheres to the BEP principle, as the activation energy consistently decreases in line with the bond dissociation energies (BDE) of the substrates (from CHE and EB to CHD), regardless of whether the abstractor is an aminoxyl radical or a Fe(IV)O complex. The corresponding plot provides a nice correlation between activation energy and BDE as presented in Fig. 6.5.

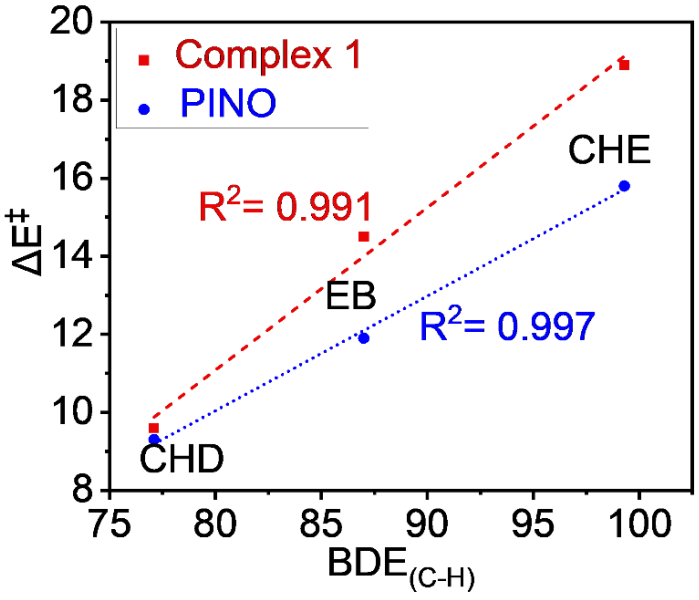

Fig. 6.5. Plot of activation energy (kcal mol^{-1}) of the reaction vs. bond dissociation energy (BDE) of the substrates.

However, this BEP correlation with BDE breaks down when comparing C-H and the O-H bond cleavage by the Fe(IV)O complex. So, to gain a comprehensive understanding of the mediator's mechanistic pattern, it is crucial to address the concern that involves explaining why the cleavage of the O-H bond in the mediator is significantly more favorable than the cleavage of the C-H bond in the substrate, even though the C-H bond has a comparable or even lower bond dissociation energy (BDE) than the O-H bond. This phenomenon can be explained using the Marcus cross relation (Eq. 6.5), as detailed by Mayer and his co-workers.[7,74]

$$k_{AH/B} = \sqrt{k_{AH/A} k_{BH/B} K_{eq} f} \quad \text{----------} \quad \text{Eq. 6.5}$$

This cross-relation predicts the rate constant for the following cross-reaction:

$$A - H + B \rightarrow A + H - B \text{ --------- Eq. 6.6}$$

In Eq. 6.5, the first and second terms under the square root represent the rate constants for the self-exchanged HAT reactions. The third term denotes the equilibrium constant for the reaction shown in Eq. 6.6. So, according to Eq. 6.5, the rate constant for the cross-reaction is dependent on these self-exchange reactions. In the case of C-H bonds, these self-exchange reactions are dramatically slow.[7] Consequently, the Fe(IV)O-catalyzed abstraction of hydrogen from hydrocarbon substrates is significantly slower compared to that when hydroxylamines act as mediators.

6.4.3: Thermodynamic Control of Reactivity

In this part of study, we have calculated the E-O bond energy (where E = Fe for ferryl and E = N for nitroxyl) before and after H-abstraction. The results are presented in the Table 6.3.

Table 6.3 The Fe-O and N-O bond and their bond dissociation enthalpy in reactant and intermediate computed at the B1 level of theory, using B3LYP as the functional.

Bond	ΔH_{BDE}
Fe=O (in reactant Fe(IV)O)	85.3
Fe-OH (in Intermediate)	70.4
N-O (in PINO)	162.3
N-OH (in NHPI)	137.7

From Table 6.3, it is clear that the Fe-O bond enthalpy decreases by 14.9 kcal mol^{-1} from the reactant state (85.3 kcal mol^{-1}) to the intermediate state (70.4 kcal mol^{-1}). Similarly, the N-O bond enthalpy in the mediator decreases from 162.3 to 137.7 kcal mol^{-1}, a reduction of 24.6 kcal mol^{-1}, indicating a more exothermic reaction. Consistent with these findings, the nitroxyl radical-mediated pathway (mediator pathway) is observed to be more exothermic than the direct pathway, as depicted in the potential energy surfaces in Fig. 6.2. Therefore, it can be confidently concluded that the mediator pathway is more favorable from both kinetic and thermodynamic standpoints.

6.4.4: Distortion Energy

Next, we examine the distortion energy necessary to achieve the transition states, which considerably contributes to the activation energy. The Eq. 6.7 presented in the computational details section is used to determine the distortion energies ($\Delta E^{\ddagger}_{dis}$) of the oxidants and substrate in order to reach the transition states. The related data have been compiled and are shown in Table 6.4 below.

Table 6.4 Distortion energy ($\Delta E^{\ddagger}_{dis}$) in kcal mol^{-1}, along with the substrate's (ΔS) and oxidant's (ΔO) contribution.

Reaction	ΔS	ΔO	$\Delta E^{\ddagger}_{dis}$
1+EB	13.1	5.2	18.3
1+NHPI	8.5	1.7	10.2
PINO+EB	11.1	3.1	14.2
1+CHE	17.4	7.5	24.9
1+NHPI	8.5	1.7	10.2
PINO+CHE	16.4	4.2	20.6
1+CHD	10.0	4.0	14.0
1+NHPI	8.5	1.7	10.2
PINO+CHD	9.3	2.5	11.8
1+EB	13.1	5.2	18.3
1+NHQI	7.0	1.2	8.2

QINO+EB	4.2	3.1	7.3

The values in Table 6.4 clearly show that the distortion energy is consistently lower in the transition state catalyzed by the mediator radical compared to that in the reaction catalyzed by complex 1. This evidence suggests that mediator radicals exhibit greater activity than metal-oxo complexes, further supporting the mediator mechanism. Additionally, the distortion energy values help to explain the higher reactivity of the QINO radical (7.3 kcal mol^{-1}) compared to that of PINO (14.2 kcal mol^{-1}).

The steric factor might play a significant role, as the abstractor site 'O' in Fe(IV)O is pretty blocked (~ 7.6% free space as calculated using the SambVca 2.1 program)[75] by the macrocycles, whereas it is completely exposed in PINO or QINO, making these species more reactive toward HAT.

6.4.5: Quantum Mechanical Tunneling (QMT)

Based on previous literature, H-abstraction reactions might exhibit significant tunneling effects due to the light mass of the hydrogen atom. This aspect was briefly mentioned in the section on spin state preferences. To fully elucidate the reactivity pattern, a comprehensive study of the quantum mechanical tunneling (QMT) effects on the reactivity of C-H abstraction from EB, catalyzed by Fe(IV)O complexes and a mediator radical system, has been carried out. The findings are presented in Table 6.5.

Table 6.5 The imaginary frequencies of the transition states ($\nu^{\ddagger}_{H}$), transmission coefficients for H (κ_H) and D (κ_D), kinetic isotope effect at 298 K, tunneling correction values ($\Delta\Delta E^{\ddagger}_{tun,}$ in kcal mol^{-1}) at 298 K, tunneling corrected barrier ($\Delta E - \Delta\Delta E^{\ddagger}_{tun}$) at the B2+ZPE level, using B3LYP as the functional and the tunneling contribution (% tunneling) of the overall reaction.

Reactions	$\nu^{\ddagger}_{H}$	κ_H	κ_D	KIE_{Eck}	$\Delta\Delta E^{\ddagger}_{tun}$	ΔE-$\Delta\Delta E^{\ddagger}_{tun}$	%tunneling
1-EB	1832	136.7	10.9	80.6	2.9	11.6/15.0	99.3
1-NHPI	1953	21.5	9.2	16.2	1.8	4.7/6.5	95.3
PINO-EB	1690	17.4	5.8	19.9	1.7	10.3/13.0	94.3

The last column of Table 6.5 shows that tunneling contributes significantly to all of the reactions. A comparison of KIE with experimental data for the reactions of 1 + EB has already been discussed earlier.

There are experimental reports of KIE values for the reaction of PINO with p-xylene at 298 K, which are 25.0 in acetic acid and 28.4 in acetonitrile[76] Our computed KIE value of 20 for the reaction between PINO and EB shows excellent agreement with the experimental results. After tunneling corrections were incorporated into the barrier heights, the overall efficiency of the mediator pathway improved energetically by approximately 1.3 kcal mol^{-1}.

It is an important to note that the mediator enhances the reactivity of complex 1 only when the triplet state pathway is considered. However, the quintet state barrier for complex 1 (11.6 kcal mol^{-1}) is lower than that for the HAT by PINO (12.0 kcal mol^{-1}), providing additional evidence for the *S*=1 state reactivity of complex 1 beyond what is indicated by the KIE.

6.5: Conclusions

This study presents a comprehensive computational investigation into the mechanism and efficiency of Fe(IV)O-catalyzed C-H activation enhanced by mediators. The investigation focuses on the Fe(IV)O complex $[Fe(IV)ON4Py]^{2+}$, along with two mediators, NHPI and NHQI, and three substrates: ethylbenzene, cyclohexane, and cyclohexadiene. Complex 1 primarily proceeds via the S = 1 pathway, as evidenced by the primary H/D kinetic isotope effect. The findings also reveal that NO-H bond cleavage catalyzed by Fe(IV)O from the mediator is significantly more favorable than the C-H activation of the substrate, with no direct correlation to the bond dissociation energy of the respective bonds.

This discrepancy is clarified using the Marcus cross-relation, which incorporates the self-exchange reaction rate—a rate that is notably slower for C-H bonds compared to that for O-H bonds. This slow rate results in the C-H bond being relatively unreactive, leading to the formation of the mediator radical first in the system rather than a direct HAT from the substrate.

The mediator radical then abstracts a hydrogen atom from the substrates, demonstrating a greater abstraction power than the iron-oxo complexes. The activation barriers and exothermicity of the reactions demonstrate that the mediator pathway is favored under both thermodynamic and kinetic control. This conclusion is further supported by the distortion energy required for the reactants to reach the transition state, along with the higher steric hindrance in Fe(IV)O compared with PINO or QINO. Quantum mechanical tunneling plays a substantial role in these reactions, with our results showing excellent agreement with available experimental data, particularly concerning the kinetic isotope effect. Additionally, NHQI is found to be more reactive than PINO. The activation energy of the substrates aligns with the bond dissociation energy (BDE) and follows the Bell-Evans-Polanyi (BEP) principle.

This investigation not only provides valuable insights into how NHPI and NHQI mediate reaction energetics but also justifies the proposed mechanism in its entirety. The findings highlight the potential for discovering more effective mediators, encouraging bioinorganic chemists to explore novel ways to enhance the reactivity of metal-oxo complexes.

Chapter 1:

1. B.M. Gardner, C.C.C.S. Johansson and T.J. Colacot, *Industrial Milestones in Organometallic Chemistry*, 2020, 1-22.
2. S. Rafique, M. Idrees, A. Nasim, H. Akbar and A. Athar, *Biotechnol. Mol. Biol. Rev.*, 2010, **5**, 38-45.
3. M. L. Crawley and B. M. Trost, *Applications of Transition Metal Catalysis in Drug Discovery and Development: An Industrial Perspective,* 2012.
4. B. McCloy, *Some Applications of Transition Metal Complexes,* 1995.
5. S. Sahu and D. P. Goldberg, *J. Am. Chem. Soc.*, 2017, **138**, 11410–11428.
6. E. B. Bauer, *Isr. J. Chem.*, 2017, **57**, 1131–1150.
7. B. Mondal, L. Roy, F. Neese and S. Ye, *Isr. J. Chem.*, 2016, **56**, 763–772.
8. M. Guo, T. Corona, K. Ray and W. Nam, *ACS Cent. Sci.*, 2019, **5**, 13–28.
9. K. Rydel Ciszex, T. Pacześniak, I. Zaborniak and P. Błoniarz, K. Surmacz, A. Sobkowiak, P. Chmielarz, *Processes*, 2020, **8**, 1683.
10. A. J. Jasniewski and L. Que, *Chem. Rev.*, 2018, **118**, 2554-2592.
11. J. C. Hsieh, *Chem. Rec.*, 2021, **21**, 3370–3381.
12. M. Costas, M. P. Mehn, M. P. Jensen and L. Que, *Chem. Rev.,* 2004, **104**, 939–986.
13. X. P. Shan and L. Que, *J. Inorg. Biochem.,* 2006, **100**, 421-433.
14. C. A. Grapperhaus, B. Mienert, E. Bill, T. Weyhermuller and K. Wieghardt, *Inorg. Chem.,* 2000, **39**, 5306-5317.
15. M. H. Lim, J.-U. Rohde, A. Stubna, M. R. Bukowski, M. Costas, R. Y. N. Ho, E. Munck, W. Nam and L. Que, Jr, *Proc. Natl. Acad. Sci. U. S. A.,* 2003, **100**, 3665-3670.
16. J. Kaizer, E. J. Klinker, N. Y. Oh, J.-U. Rohde, W. J. Song, A. Stubna, J. Kim, E. Munck, W. Nam and L. Que, Jr, *J. Am. Chem. Soc.,* 2004, **126**, 472-473.
17. N. Y. Oh, Y. Suy, M. J. Park, M. S. Seo, J. Kim and W. Nam, *Angew. Chem., Int. Ed.,* 2005, **44**, 4235-4239.
18. W. Nam, *Acc. Chem. Res.,* 2007, **40**, 522–531.
19. M. R. Bukowski, K. D. Koehntop, A. Stubna, E. L. Bominaar, J. A. Halfen, E. Münck, W. Nam and L. Que, Jr, *Science*, 2005, **310**, 1000–1002.

20. E. J. Klinker, J. Kaizer, W. W. Brennessel, N. L. Woodrum, C. J. Cramer and L. Que, Jr, *Angew. Chem., Int. Ed.,* 2005, **44**, 3690-3694.
21. C. V. Sastri, K. Oh, Y. J. Lee, M. S. Seo, W. Shin and W. Nam, *Angew. Chem., Int. Ed.,* 2006, **45**, 3992-3995.
22. Y. Suh, M. S. Seo, K. M. Kim, Y. S. Kim, H. G. Jang, T. Tosha, T. Kitagawa, J. Kim and W. Nam, *J. Inorg. Biochem.,* 2006, **100**, 627-633.
23. K. Nehru, M. S. Seo, J. Kim and W. Nam, *Inorg. Chem.,* 2007, **46**, 293-298.
24. V. Balland, M.-F. Charlot, F. Banse, J.-J. Girerd, T. A. Mattioli, E. Bill, J.-F. Bartoli, P. Battioni and D. Mansuy, *Eur. J. Inorg. Chem.,* 2004, 301-308.
25. M. Martinho, F. Banse, J.-F. Bartoli, T. A. Mattioli, P. Battioni, O. Horner, S. Bourcier and J.-J. Girerd, *Inorg. Chem.,* 2005, **44**, 9592-9596.
26. M. R. Bukowski, P. Comba, A. Lienke, C. Limberg, C. L. de Laorden, R. Mas-Balleste, M. Merz and L. Que, *Angew. Chem., Int. Ed.,* 2006, **45**, 3446-3449.
27. L. Ji, A. Franke, M. Brindell, M. Oszajca, A. Zahl and R. Van Eldik, *Chem. – Eur. J.,* 2014, **20**, 14437–14450.
28. X. Shan and L. Que, J. *Inorg. Biochem.,* 2006, **100**, 421–433.
29. H. Hirao, L. Que, W. Nam and S. Shaik, *Chem. – Eur. J.,* 2008, **14**, 1740–1756.
30. R. Kumar, B. Pandey, A. Sen, M. Ansari, S. Sharma and G. Rajaraman, *Coord. Chem. Rev.,* 2020, **419**, 213397.
31. P. C. Andrikopoulos, C. Michel, S. Chouzier and P. Sautet, *ACS Catal.,* 2015, **5**, 2490–2499.
32. B. K. Mai and Y. Kim, *Angew. Chem., Int. Ed.,* 2015, **54**, 3946–3951.
33. D. Schröder, S. Shaik and H. Schwarz, *Acc. Chem. Res.,* 2000, **33**, 139–145.
34. Y. H. Kwon, B. K. Mai, Y. M. Lee, S. N. Dhuri, D. Mandal, K. B. Cho, Y. Kim, S. Shaik and W. Nam, *J. Phys. Chem. Lett.,* 2015, **6**, 1472–1476.
35. C. Krebs, D. G. Fujimori, C. T. Walsh and J. M. Bollinger, in *Accounts of Chemical Research*, 2007, **40**, 484–492.
36. S. Shaik, D. Kumar, S. P. de Visser, A. Altun and W. Thiel, *Chem. Rev.*, 2005, **105**, 2279–2328.
37. G. F. Hendry and T. G. Jones, *J. Med. Gene.*, 1980, **17**, 1-14.
38. F. Ogliaro, M. Filatov and S. Shaik, *Eur. J. Inorg. Chem.*, 2000, 2455–2458.

39. K. L. Stone, R. K. Behan and M. T. Green, *Proc. Natl. Acad. Sci. U. S. A.*, 2005, **102**, 16563–16565.
40. M. S. Liao, J. D. Watts and M. J. Huang, *J. Phys. Chem. A*, 2005, **109**, 7988–8000.
41. S. Shaik, D. Kumar, S. P. de Visser, A. Altun and W. Thiel, *Chem. Rev.*, 2005, **105**, 2279–2328.
42. D. Mallick and S. Shaik, *J. Am. Chem. Soc.*, 2017, **139**, 11451−11459.
43. A. Mukhopadhyaya and Md E. Ali, *J. Phys. Chem. A,* 2024, **128**, 12, 2339–2348.
44. K. M. Paolesse, R. Kadish, K. M. Smith and R. Guilard, *Porphyr. Handbook.*, 2000, **2**, 201–232.
45. J. M. Bollinger Jr, J. C. Price, L. M. Hoffart, E. W. Barr and C. Krebs, *Eur. J. Inorg. Chem.,* 2005, **2005** 4245–4254.
46. J. N. Barlow, Z. Zhang, P. John, J. E. Baldwin and C. J. Schofield, *Biochemistry.,* 1997, **36**, 3563–3569.
47. D. P. Galonic, E. W. Barr, C. T. Walsh, J. M. Bollinger and C. Krebs, *Nat. Chem. Biol.,* 2007, **3**, 113–116.
48. E. I. Solomon, T. C. Brunold, M. I. Davis, J. N. Kemsley, S.-K. Lee, N. Lehnert, F. Neese, A. J. Skulan, Y.-S. Yang, J. Zhou, *Chem. Rev.*, 2000, **100**, 235–349.
49. C. Wegeberg, M. L. Skavenborg, A. Liberato, J. N. McPherson, W. R. Browne, E. D. Hedegård and C. J. McKenzie, *Inorg. Chem.*, 2021, **60**, 1975–1984.
50. J. L. Lee, D. L. Ross, K. S. Barman, J. W. Ziller and A. S. Borovik, *Inorg. Chem.*, 2021, **60**, 13759–13783.
51. G. Mukherjee, J. K. Satpathy, U. K. Bagha, M. Q. E. Mubarak, C. V. Sastri and S. P. De Visser, *ACS Catal.*, 2021, **11**, 9761–9797.
52. X. Engelmann, I. Monte-Pérez, and K. Ray, *Angew. Chem., Int. Ed.*, 2016, **55**, 7632–7649.
53. H. Hirao, F. Li, L. Que and K. Morokuma, *Inorg. Chem.*, 2011, **50**, 6637–6648.
54. L. Kaur and D. Mandal, *Inorganica Chim. Acta*, 2024, **572**, 122292.
55. M. Kumar, M. K. Gupta, M. Ansari and A. Ansari, ***Phys. Chem. Chem.* Phys.,** 2024, **26**, 4349–4362.
56. H. Fujii, *Coord. Chem. Rev.*, 2002, **226**, 51–60.
57. L. Kaur and D. Mandal, *Inorg. Chem.*, 2022, **61**, 14582–14590.
58. A. R. McDonald and L. Que, *Coord. Chem. Rev.*, 2013, **257**, 414–428.

59. H. Schwarz, S. Shaik, *Acc. Chem. Res.*, 2000, **33**, 139–145.

60. J. U. Rohde, J. H. In, M. H. Lim, W. W. Brennessel, M. R. Bukowski, A. Stubna, E. Münck, W. Nam and L. Que, *Science.,* 2003, **299**, 1037–1039.

61. S. Kal, S. Xu and L. Que, *Angew. Chemie - Int. Ed.,* 2020, 59, 7332–7349.

62. S. P. de Visser, J. U. Rohde, Y. M. Lee, J. Cho and W. Nam, *Coord. Chem. Rev.,* 2013, **257**, 381–393.

63. W. Nam, *Acc. Chem. Res.*, 2015, **48**, 2415–2423.

64. Y. M. Lee, S. N. Dhuri, S. C. Sawant, J. Cho, M. Kubo, T. Ogura, S. Fukuzumi and W. Nam, *Angew. Chemie - Int. Ed.*, 2009, **48**, 1803–1806.

65. J. Kaizer, E. J. Klinker, N. A. Oh, J. Rohde, W. J. Song, A. Stubna, J. Kim, E. Munck, W. Nam and L. Que, *J. Am. Chem. Soc.*, 2004, **126**, 472–473.

66. E. Andris, K. Segers, J. Mehara, L. Rulíše and J. Roithová, *Angew. Chemie*, 2020, **132**, 23337–23344.

67. J. England, J. Prakash, M. A. Cranswick, D. Mandal, Y. Guo, E. Münck, S. Shaik and L. Que, *Inorg. Chem.*, 2015, **54**, 7828–7839.

68. H. H. Limbach, ed. J. T. Hynes, J. Klinman, H. H. Limbach and R. L. Schowen, *Wiley-VCH, Weinheim,* 2007, **1 and 2**, 135–221.

69. S. T. Kleespies, W. N. Oloo, A. Mukherjee and L. Que, *Inorg. Chem.*, 2015, **54**, 5053–5064.

70. S. Hammes-Schiffer and A. A. Stuchebrukhov, *Chem. Rev.*, 2010, **110**, 6939–6960.

71. J. M. Mayer, *Acc. Chem. Res.*, 2011, **44**, 36–46.

72. W. Lai, C. Li, H. Chen and S. Shaik, *Angew. Chem., Int. Ed.*, 2012, **51**, 5556–5578.

73. P. R. Ortiz de Montellano, *Chem. Rev.*, 2010, **110**, 932–948.

74. K. U. Ingold, D. A. Pratt, *Chem. Rev.* 2014, **114**, 9022–9046.

75. M. Salamone, M. Bietti, *Acc. Chem. Res.* 2015, **48**, 2895–2903.

76. H. Park and D. Lee, *Chem. - A Eur. J.*, 2020, **26**, 5916–5926.

77. S. P. de Visser, *J. Am. Chem. Soc.*, 2006, **128**, 15809–15818.

78. D. Janardanan, D. Usharani and S. Shaik, *Angew. Chem., Int. Ed.,* 2012, **51**, 4421–4425.

79. D. Usharani, D. Janardanan, C. Li and S. Shaik, *Acc. Chem. Res.*, 2013, **46**, 471–482.

80. C. Geng, S. Ye and F. Neese, *Angew. Chemie - Int. Ed.*, 2010, **49**, 5717–5720.

81. S. Shaik, M. Filatov, D. Schröder and H. Schwarz*, Chem. – Eur. J.,* 1998, **4**, 193–199.

82. D. Mandal and S. Shaik, *J. Am. Chem. Soc.*, 2016, **138**, 2094– 2097.

83. D. Janardanan, D. Usharani, H. Chen and S. Shaik, *J. Phys. Chem. Lett.*, 2011, **2**, 2610–2617.

84. D. Mandal, R. Ramanan, D. Usharani, D. Janardanan, B. Wang and S. Shaik, *J. Am. Chem. Soc.,* 2015, **137**, 722– 733.

85. M. J. Park, J. Lee, Y. Suh, J. Kim and W. Nam, J. Am. Chem. Soc., 2006, 128, 2630.

86. Y. Zhou, X. Shan, R. Mas-Ballesté, M. R. Bukowski, A. Stubna, M. Chakrabarti, L. Slominski, J. A. Halfen, E. Münck and L. Que, *Angew. Chem., Int. Ed.,* 2008, **47**, 1896–1899.

87. C. V. Sastri, J. Lee, K. Oh, Y. J. Lee, J. Lee, T. A. Jackson, K. Ray, H. Hirao, W. Shin, J. A. Halfen, J. Kim, L. Que, S. Shaik and W. Nam, *Proc. Natl. Acad. Sci. U. S. A.,* 2007, **104**, 19181–19186.

88. Y. Hitomi, K. Arakawa and M. Kodera, *Chem. Commun.,* 2014, **50**, 7485–7487.

89. E. J. Klinker, S. Shaik, H. Hirao and L. Que, Angew. Chem., Int. Ed., 2009, **48**, 1291–1295.

90. M. S. Seo, J. Y. Kim, J. Annaraj, Y. Kim, Y.-M. Lee, S.-J. Kim, J. Kim and W. Nam, *Angew. Chem., Int. Ed.,* 2007, **46**, 377– 380.

91. R. Latifi, L. Tahsini, B. Karamzadeh, N. Safari, W. Nam and S. P. De Visser, *Arch. Biochem. Biophys.,* 2011, **507**, 4–13.

92. K. Ray, Y. M. Lee and W. Nam, *Coord. Chem. Rev.,* 2017, **334**, 25–42.

93. S. N. Dhuri, K. B. Cho, Y. M. Lee, S. Y. Shin, J. H. Kim, D. Mandal, S. Shaik and W. Nam, *J. Am. Chem. Soc.,* 2015, **137**, 8623–8632.

94. P. Barman, A. K. Vardhaman, B. Martin, S. J. Wörner, C. V. Sastri and P. Comba, *Angew. Chem.,* 2015, **127**, 2123– 2127.

95. D. F. Leto, R. Ingram, V. W. Day and T. A. Jackson, *Chem. Commun.,* 2013, **49**, 5378–5380.

96. H. Yoon, Y. M. Lee, X. Wu, K. Bin Cho, R. Sarangi, W. Nam and S. Fuhkuzumi, *J. Am. Chem. Soc.,* 2013, **135**, 9186– 9194.

97. M. Guo, T. Corona, K. Ray and W. Nam, *ACS Cent. Sci.,* 2019, **5**, 13–28.

98. X. Wu, M. S. Seo, K. M. Davis, Y. M. Lee, J. Chen, K. Bin Cho, Y. N. Pushkar and W. Nam, *J. Am. Chem. Soc.,* 2011, **133**, 20088–20091.

99. K.-B. Cho, S. Shaik and W. Nam, *J. Phys. Chem. Lett.,* 2012, **3**, 2851–2856.

100. S. Liu, K. Mase, C. Bougher, S. D. Hicks, M. M. Abu-Omar and S. Fukuzumi, *Inorg. Chem.*, 2014, **53**, 7780– 7788.

101. K. Bin Cho, H. Kang, J. Woo, Y. J. Park, M. S. Seo, J. Cho and W. Nam, *Inorg. Chem.,* 2014, **53**, 645–652.

102. T. Ishizuka, H. Kotani and T. Kojima, *Dalton Trans.,* 2016, **45**, 16727–16750.

103. T. Matsuo and J. M. Mayer, *Inorg. Chem.*, 2005, **44**, 2150-2158.

104. T. Kojima, K. Nakayama, K. Ikemura, T. Ogura and S. Fukuzumi, *J. Am. Chem. Soc.,* 2011, **133**, 11692–11700.

105. S. Ohzu, T. Ishizuka, Y. Hirai, H. Jiang, M. Sakaguchi, T. Ogura, S. Fukuzumi and T. Kojima, *Chem. Sci.,* 2012, **3**, 3421–3431.

106. S. N. Dhuri, S. S. Mi, Y. M. Lee, H. Hirao, Y. Wang, W. Nam and S. Shaik, *Angew. Chem., Int. Ed.*, 2008, **47**, 3356–3359.

107. A. R. McDonald, Y. Guo, V. V. Vu, E. L. Bominaar, E. Münck and L. Que, *Chem. Sci.,* 2012, **3**, 1680–1693.

108. I. Monte-Pérez, X. Engelmann, Y. M. Lee, M. Yoo, E. Kumaran, E. R. Farquhar, E. Bill, J. England, W. Nam, M. Swart and K. Ray, *Angew. Chem., Int. Ed.,* 2017, **56**, 14384–14388.

109. J. U. Rohde and L. Que, *Angew. Chem., Int. Ed.,* 2005, **44**, 2255–2258.

110. A. Barbieri, O. Lanzalunga, A. Lapi and S. Di Stefano, *J. Org. Chem.*, 2019, **84**, 13549–13556.

111. M. D. B. Mancini, M. Bernardini, B. E. Birzu, A. D. Santis, S. D. Stefano, F. Frateloreto, D. Khaksar, A. Lapi, G. Olivo and O. Lanzalunga, *Eur. J. Org Chem.*, 2023, **26**, No. e202300360.

112. M. D. B. Mancini, A. D. Gelsomino, S. D. Stefano, F. Frateloreto, A. Lapi, O. Lanzalunga, G. Olivo and S. Sajeva, *ACS Omega.,* 2021, **6**, 26428−26438.

113. J. M. Bae, M. M. L. Seul, A. Lee, S. Y. Lee, K. H. Bok, J. Kim and C. Kim, *Inorg. Chim. Acta*., 2016, **451**, 8−15.

114. C. Annunziatini, M. F. Gerini, O. Lanzalunga and M. Lucarini, *J. Org. Chem.*, 2004, **69**, 3431–3438.

115. Y. Cai, N. Koshino, B. Saha and J. H. Espenson, *J. Org. Chem.*, 2005, **70**, 238.

116. M. Bietti, V. Forcina, O. Lanzalunga, A. Lapi, T. Martin, M. Mazzonna, and M. Salamone., *J. Org. Chem.,* 2016, **81**, 11924−11931.

117. G. A. DiLabio, P. Franchi, O. Lanzalunga, A. Lapi, F. Lucarini, M. Lucarini, M. Mazzonna, V. K. Prasad and B. Ticconi, *J. Org. Chem.*, 2017, **82**, 6133–6141.

Chapter 2:

1. Jensen, *Introduction to Computational Chemistry*, 2nd ed, John Wiley and Sons, 2007.
2. D. B. Cook. *Handbook of Computational Quantum Chemistry*. Dover Publications, 2005.
3. R. G. Parr and W. Yang, *Density-Functional Theory of Atoms and Molecules*, Oxford University Press, 1995.
4. David C. Young. *Computational Chemistry: A Practical Guide for Applying Techniques* to *Real World Problems*. John Wiley & Sons, 2001.
5. E. G. Lewars., *Computational Chemistry: Introduction to the Theory and Applications of Molecular and Quantum Mechanics*, 3rd ed. Springer., 2016.
6. C. J. Cramer. *Essentials of Computational Chemistry: Theories and Models*. John Wiley & Sons, 2004.
7. E. Schrödinger, *Ann. Phys.*, 1926, **384**, 361–376.
8. A. Szabo, N. S. Ostlund, *Modern Quantum Chemistry: Introduction to Advanced Electronic Structure Theory*, Dover Publications, 1996.
9. P. W. Atkins, R. S. Friedman, *Molecular Quantum Mechanics*, Oxford University Press, 2011.
10. I.N. Levine**,** *Quantum Chemistry*, 7th ed, Pearson, 2013.
11. M. Born, J. R. Oppenheimer, *Ann. Phys.* 1927, **84**, 457–484.
12. B. T. Sutcliffe, R. G. Woolley, R. G., *J. Chem. Phys.* 2012, **137**, 22A544.
13. D. R. Hartree, *Proc. Camb. Philol. Soc.* 1928, **24**, 89-110.
14. C.C.J. Roothaan**,** *Rev. Mod. Phys.* 1951, **23**, 69–89.
15. R. J. Bartlett and M. Musiał, *Chem. Rev*., 2007, **107**, 4866-4896.
16. P. Hohenberg and W. Kohn, *Phys. Rev*., 1964, **136**, B864-B871.
17. W. Kohn and L. J. Sham, *Phys. Rev*., 1965, **140**, A1133-A1138.
18. J. P. Perdew and Y. Wang, *Phys. Rev. B*, 1992, **45**, 13244-13249.
19. A. D. Becke, *J. Chem. Phys.*, 1995, **102**, 1039-1045.
20. C. E. Dykstra, G. Frenking, K. S. Kim, G.E Scuseria ,*Theory and Applications of Computational Chemistry: The First Forty Years*, Elsevier: Amsterdam, NL, 2005.
21. D. M. Ceperley and B. J. Alder, *Phys. Rev. Lett*., 1980, **45**, 566-569.
22. J. P. Perdew and Y. Wang, *Phys. Rev. B*, 1986, **33**, 8800-8802.
23. J. P. Perdew, K. Burke, and M. Ernzerhof, *Phys. Rev. Lett*., 1996, **77**, 3865-3868.

24. A. D. Becke, *J. Chem. Phys.*, 1993, **98**, 1372–1377.
25. C.Lee, W.Yang, R. G. P., *Phys. Rev.* 1988, **37**,785–78.
26. P. J. Stephens, F. Devlin, C. Chabalowski and M. J. Frisch, J. Phys. Chem. B, 1994, 98, 11623–11627.
27. S. H. Vosko, L. Wilk and M. Nusair, *Can. J. Phys.*, 1980, **58**, 1200–1211.
28. C. Lee, W. Yang and R. G. Parr, *Phys. Rev. B.*, 1988, **37**, 785–789.
29. J. P. Perdew, K. Burke, and M. Ernzerhof, *J. Chem. Phys*., 1996, **105**, 9384-9391.
30. S. C. Chan, Z. Z. Ang, P. Gupta, R. Ganguly, Y. Li, S. Ye and J. England, *Inorg. Chem*., 2020, **59**, 4118–4128.
31. M. J. Baird, A. S. Borovik, and G. M. Bernard, *J. Am. Chem. Soc.*, 2001, **123**, 7106-7112.
32. J. M. D. Smith, R. D. Hall, and R. H. Crabtree, *J. Am. Chem. Soc.*, 2004, **126**, 12412-12420.
33. M. B. Smith, L. M. Schreiber, and J. R. Long, *Coord. Chem. Rev.*, 2006, **250**, 743-764.
34. D. Mandal and S. Shaik, *J. Am. Chem. Soc.*, 2016, **138**, 2094–2097.
35. M. Kumar, M. K. Gupta, M. Ansari and A. Ansari, *Dalt. Trans*., 2024, **26**, 4349–4362.
36. D. Mandal, D. Mallick and S. Shaik, *Acc. Chem. Res.*, 2018, **51**, 107–117.
37. A. Altun, J. Breidung, F. Neese and W. Thiel, *J. Chem. Theory Comput.*, 2014, **10**, 3807–3820.
38. J. C. Slater, *Phys. Rev.*, 1951, **81**, 385-390.
39. T. H. Dunning Jr., *J. Chem. Phys.*, 1989, **90**, 1007-1023.
40. T. Marino, M. G. Fortino, N. Russo, M. Toscano and M. E. Alberto, *Int. J. Mol. Sci.*, 2021, **22**, 1234-1245.
41. Y. Wang, X. Jin, H. S. Yu, D. G. Truhlar and X. He, *Proc. Natl. Acad. Sci. U. S. A*.**, 2017**, **114**, 8487–8492.
42. D. E. Woon and T. H. Dunning Jr., *J. Chem. Phys*., 1994, **100**, 2975-2988.
43. J. A. Pople, *Int. J. Quantum Chem.,* 1967, **1**, 269-276.
44. J. R. D. Feller, *J. Chem. Phys.*, 1996, **105**, 6211-6219.
45. L. S. Turner, A. J. Morrison, and J. R. Williams, *Inorg. Chem*., 2022, **61**, 1428-1441.
46. P. J. Hay and W. R. Wadt, J. Chem. Phys., 1985, 82, 270–283.
47. P. Fuentealba, H. Preuss, H. Stoll and L. Von Szentpály, Chem. Phys. Lett., 1982, 89, 418–422.

48. M. J. Frisch, G. W. Trucks, H. B. Schlegel, et al., *J. Chem. Phys.*, 1996, **104**, 6377-6384.
49. L. K. Anderson and H. J. Fisher, *J. Phys. Chem. B*, 2021, **125**, 11632-11643.
50. K. L. Zhang, M. R. Cooper, and P. J. Knight, *Phys. Chem. Chem. Phys*., 2023, **25**, 4850-4863.
51. G. A. Voth and A. L. Garcia, *J. Chem. Phys*., 1995, **102**, 663-678.
52. K. Mathew, R. Sundararaman, K. Letchworth-Weaver, T. A. Arias and R. G. Hennig, *J. Chem. Phys*., 2005, **123**, 164112.
53. A. V. Marenich, R. M. Olson, C. P. Kelly, C. J. Cramer and D. G. Truhlar, *J. Chem. Theory Comput.*, 2007, **3**, 2011–2033.
54. E. L. Moreira, *Int. J. Quantum Chem*., 2013, **113**, 1511-1521.
55. J. M. Thomas and A. R. Cossi, *Chem. Rev.*, 2013, **113**, 845-877.
56. A. Stone, *The theory of intermolecular forces*, oUP oxford, 2013.
57. S. Grimme, S. Ehrlich and L. Goerigk, *J. Comput. Chem.*, 2011, **32**, 1456–1465.
58. R. H. Fowler and E. A. Guggenheim, *Trans. Faraday Soc.*, 1939, **35**, 155-167.
59. D. Mandal, R. Ramanan, D. Usharani, D. Janardanan, B. Wang and S. Shaik, *J. Am. Chem. Soc.*, 2015, **137**, 722–733.
60. L. Gagliardi, M. J.Behrens, L.T Richards, *Coord. Chem. Rev*., 2019**, 394**, 34-47.
61. J. Eckart, *Phys. Rev*., 1930, **35**, 1303-1307.
62. Gaussian 16, Revision C.01, M. J. Frisch, G. W. Trucks, H. B. Schlegel, G. E. Scuseria, M. A. Robb, J. R. Cheeseman, G. Scalmani, V. Barone, G. A. Petersson, H. Nakatsuji, X. Li, M. Caricato, A. V. Marenich, J. Bloino, B. G. Janesko, R. Gomperts, B. Mennucci, H. P. Hratchian, J. V. Ortiz, A. F. Izmaylov, J. L. Sonnenberg, D. Williams-Young, F. Ding, F. Lipparini, F. Egidi, J. Goings, B. Peng, A. Petrone, T. Henderson, D. Ranasinghe, V. G. Zakrzewski, J. Gao, N. Rega, G. Zheng, W. Liang, M. Hada, M. Ehara, K. Toyota, R. Fukuda, J. Hasegawa, M. Ishida, T. Nakajima, Y. Honda, O. Kitao, H. Nakai, T. Vreven, K. Throssell, J. A. Montgomery, Jr., J. E. Peralta, F. Ogliaro, M. J. Bearpark, J. J. Heyd, E. N. Brothers, K. N. Kudin, V. N. Staroverov, T. A. Keith, R. Kobayashi, J. Normand, K. Raghavachari, A. P. Rendell, J. C. Burant, S. S. Iyengar, J. Tomasi, M. Cossi, J. M. Millam, M. Klene, C. Adamo, R. Cammi, J. W. Ochterski, R. L. Martin, K. Morokuma, O. Farkas, J. B. Foresman, and D. J. Fox, Gaussian, Inc., Wallingford CT, 2016.
63. Gaussian, Inc., GaussView, Version 6, Gaussian, Inc., Wallingford, CT, 2016.
64. G. A. Andrienko. *Chemcraft Molecular Visualization Program*, version 1.8.

65. T. Lu, F. Chen, *J. Comput. Chem.,* 2012, **33**, 580-592.

Chapter 3:

1. C. Krebs, D. G. Fujimori, C. T. Walsh and J. M. Bollinger, *Acc. Chem. Res.*, 2007, **40**, 484-492.
2. L. Que, *Acc. Chem. Res.*, 2007, **40**, 493–500.
3. W. Nam, *Acc. Chem. Res.*, 2007, **40**, 522–531.
4. D. C. Lacy, R. Gupta, K. L. Stone, J. Greaves, J. W. Ziller, M. P. Hendrich and A. S. Borovik, *J. Am. Chem. Soc.*, 2010, **132**, 12188–12190.
5. W. Nam, Y. M. Lee and S. Fukuzumi, *Acc. Chem. Res.*, 2014, **47**, 1146–1154.
6. W. N. Oloo and L. Que, *Acc. Chem. Res.*, 2015, **48**, 2612–2621.
7. A. S. Borovik, *Chem. Soc. Rev.*, 2011, **40**, 1870–1874.
8. L. Ji, A. Franke, M. Brindell, M. Oszajca, A. Zahl and R. Van Eldik, *Chem. -Eur. J.*, 2014, **20**, 14437–14450.
9. X. Shan and L. Que, *J. Inorg. Biochem.*, 2006, **100**, 421–433.
10. C. V Sastri, J. Lee, K. Oh, Y. Jin Lee, J. Lee, T. A. Jackson, K. Ray, H. Hirao, W. Shin, J. A. Halfen, J. Kim, L. Que, S. Shaik and W. Nam, *Proc. Natl. Acad. Sci. U.S.A.,* 2007, **104**, 19181-19186.
11. H. Hirao, L. Que, W. Nam and S. Shaik, *Chem. -Eur. J.*, 2008, **14**, 1740–1756.
12. R. Kumar, B. Pandey, A. Sen, M. Ansari, S. Sharma and G. Rajaraman, *Coord. Chem. Rev.*, 2020, **419**, 213397.
13. H. Park and D. Lee, *Chem. -Eur. J.*, 2020, **26**, 5916–5926.
14. P. C. Andrikopoulos, C. Michel, S. Chouzier and P. Sautet, *ACS Catal.*, 2015, **5**, 2490–2499.
15. D. Mandal, R. Ramanan, D. Usharani, D. Janardanan, B. Wang and S. Shaik, *J. Am. Chem. Soc.*, 2015, **137**, 722–733.
16. B. K. Mai and Y. Kim, *Angew. Chem. Int. Ed.*, 2015, **54**, 3946–3951.
17. D. Schröder, S. Shaik and H. Schwarz, *Acc. Chem. Res.*, 2000, **33**, 139–145.
18. D. Mandal and S. Shaik, *J. Am. Chem. Soc.*, 2016, **138**, 2094–2097.
19. Y. H. Kwon, B. K. Mai, Y. M. Lee, S. N. Dhuri, D. Mandal, K. Bin Cho, Y. Kim, S. Shaik and W. Nam, *J. Phys. Chem. Lett.*, 2015, **6**, 1472–1476.
20. J. U. Rohde, J. H. In, M. H. Lim, W. W. Brennessel, M. R. Bukowski, A. Stubna, E. Münck,

W. Nam and L. Que, *Science.*, 2003, **299**, 1037–1039.

21. M. Bukowski R., K. Koehntop D., A. Stubna, E. Bominaar L., J. Halfen A., E. Münck, W. Nam and L. Que Jr., *Science.*, 2005, **310**, 1000–1002.
22. M. Puri and L. Que, *Acc. Chem. Res.*, 2015, **48**, 2443–2452.
23. W. Nam, *Acc. Chem. Res.*, 2015, **48**, 2415–2423.
24. W. Nam, Y. M. Lee and S. Fukuzumi, *Acc. Chem. Res.*, 2018, **51**, 2014–2022.
25. A. R. McDonald and L. Que, *Coord. Chem. Rev.*, 2013, **257**, 414–428.
26. M. Costas, M. P. Mehn, M. P. Jensen and L. Que, *Chem. Rev.*, 2004, **104**, 939–986.
27. X. Engelmann, I. Monte-Pérez and K. Ray, *Angew. Chem. Int. Ed.*, 2016, **55**, 7632–7649.
28. M. S. Seo, J. Y. Kim, J. Annaraj, Y. Kim, Y.-M. Lee, S.-J. Kim, J. Kim and W. Nam, *Angew. Chem. Int. Ed.,* 2007, 46, 377–380.
29. B. Wang, Y. M. Lee, W. Y. Tcho, S. Tussupbayev, S. T. Kim, Y. Kim, M. S. Seo, K. Bin Cho, Y. Dede, B. C. Keegan, T. Ogura, S. H. Kim, T. Ohta, M. H. Baik, K. Ray, J. Shearer and W. Nam, *Nat. Commun.*, 2017, **8**, 14839.
30. R. Latifi, L. Tahsini, B. Karamzadeh, N. Safari, W. Nam and S. P. De Visser, *Arch. Biochem. Biophys.*, 2011, **507**, 4–13.
31. K. Ray, Y. M. Lee and W. Nam, *Coord. Chem. Rev.*, 2017, **334**, 25–42.
32. S. N. Dhuri, K. Bin Cho, Y. M. Lee, S. Y. Shin, J. H. Kim, D. Mandal, S. Shaik and W. Nam, *J. Am. Chem. Soc.*, 2015, **137**, 8623–8632.
33. J. Hohenberger, K. Ray and K. Meyer, *Nat. Commun.*,2012, **3**, 720.
34. S. Shaik, M. Filatov, D. Schröder and H. Schwarz, *Chem. -Eur. J.*, 1998, **4**, 193–199.
35. S. Shaik, H. Chen and D. Janardanan, *Nat. Chem.*, 2011, **3**, 19–27.
36. D. Janardanan, D. Usharani and S. Shaik, *Angew. Chem. Int. Ed.*, 2012, **51**, 4421–4425.
37. J. E. M. N. Klein, D. Mandal, W. M. Ching, D. Mallick, L. Que and S. Shaik, *J. Am. Chem. Soc.*, 2017, **139**, 18705–18713.
38. D. Mandal, D. Mallick and S. Shaik, *Acc. Chem. Res.*, 2018, **51**, 107–117.
39. S. L. Abram, I. Monte-Pérez, F. F. Pfaff, E. R. Farquhar and K. Ray, *Chem. Commun.*, 2014, **50**, 9852–9854.
40. Y. Sun, H. Tang, K. Chen, L. Hu, J. Yao, S. Shaik and H. Chen, *J. Am. Chem. Soc.*, 2016, **138**, 3715–3730.
41. Y. Kang, H. Chen, Y. J. Jeong, W. Lai, E. H. Bae, S. Shaik and W. Nam, *Chem. -Eur. J.*, 2009,

15, 10039–10046.

42. G. Mukherjee, J. K. Satpathy, U. K. Bagha, M. Q. E. Mubarak, C. V. Sastri and S. P. De Visser, *ACS Catal.*, 2021, **11**, 9761–9797.
43. Y. Zhou, X. Shan, R. Mas-Ballesté, M. R. Bukowski, A. Stubna, M. Chakrabarti, L. Slominski, J. A. Halfen, E. Münck and Q. Lawrence, *Angew. Chem. Int. Ed.*, 2008, **47**, 1896–1899.
44. T. Chantarojsiri, Y. Sun, J. R. Long and C. J. Chang, *Inorg. Chem.*, 2015, **54**, 5879–5887.
45. Y. Hitomi, K. Arakawa and M. Kodera, *Chem. Commun.*, 2014, **50**, 7485–7487.
46. E. J. Klinker, S. Shaik, H. Hirao and L. Que, *Angew. Chem. Int. Ed.*, 2009, **48**, 1291–1295.
47. D. Ley, D. Gerbig and P. R. Schreiner, *Org. Biomol. Chem.*, 2012, **10**, 3781–3790.
48. P. R. Schreiner, H. P. Reisenauer, D. Ley, D. Gerbig, C. H. Wu and W. D. Allen, *Science.*, 2011, **332**, 1300–1303.
49. A. D. Becke, *J. Chem. Phys.*, 1993, **98**, 1372–1377.
50. C. Lee, eitao Yang and R. G. Parr, *Phys. Rev. B.*, 1988, **37**, 785.
51. I. Schapiro, K. Sivalingam and F. Neese, *J. Chem. Theory Comput.*, 2013, **9**, 3567–3580.
52. P. J. Hay and W. R. Wadt, *J. Chem. Phys.*, 1985, **82**, 270–283.
53. J. D. Dill and J. A. Pople, *J. Chem. Phys.*, 1975, **62**, 2921–2923.
54. D. Janardanan, D. Usharani, H. Chen and S. Shaik, *J. Phys. Chem. Lett.*, 2011, **2**, 2610–2617.
55. J. Tomasi, B. Mennucci and R. Cammi, *Chem. Rev.*, 2005, **105**, 2999–3093.
56. A. V. Marenich, C. J. Cramer and D. G. Truhlar, *J. Phys. Chem. B*, 2009, **113**, 6378–6396.
57. P. Fuentealba, H. Preuss, H. Stoll and L. Von Szentpály, *Chem. Phys. Lett.*, 1982, **89**, 418–422.
58. Gaussian 16, Revision C.01, M. J. Frisch, G. W. Trucks, H. B. Schlegel, G. E. Scuseria, M. A. Robb, J. R. Cheeseman, G. Scalmani, V. Barone, G. A. Petersson, H. Nakatsuji, X. Li, M. Caricato, A. V. Marenich, J. Bloino, B. G. Janesko, R. Gomperts, B. Mennucci, H. P. Hratchian, J. V. Ortiz, A. F. Izmaylov, J. L. Sonnenberg, D. Williams-Young, F. Ding, F. Lipparini, F. Egidi, J. Goings, B. Peng, A. Petrone, T. Henderson, D. Ranasinghe, V. G. Zakrzewski, J. Gao, N. Rega, G. Zheng, W. Liang, M. Hada, M. Ehara, K. Toyota, R. Fukuda, J. Hasegawa, M. Ishida, T. Nakajima, Y. Honda, O. Kitao, H. Nakai, T. Vreven, K. Throssell, J. A. Montgomery, Jr., J. E. Peralta, F. Ogliaro, M. J. Bearpark, J. J. Heyd, E. N. Brothers, K. N. Kudin, V. N. Staroverov, T. A. Keith, R. Kobayashi, J. Normand, K. Raghavachari, A. P. Rendell, J. C. Burant, S. S. Iyengar, J. Tomasi, M. Cossi, J. M. Millam, M. Klene, C. Adamo, R. Cammi, J. W. Ochterski, R. L. Martin, K. Morokuma, O. Farkas, J. B. Foresman, and D. J. Fox, Gaussian,

Inc., Wallingford CT, 2016.

59. R. A. Massoud and M. A. Makhyoun, *J. Struct. Chem.*, 2019, **60**, 882–889.
60. H. Eyring, *J. Chem. Phys.*, 1935, **3**, 63–71.
61. B. Carl Eckart, *Phys. Rev.*, 1930, **35**, 1303-1309.
62. D. K. Maity, R. L. Bell and T. N. Truong, *J. Am. Chem. Soc.*, 2000, **122**, 897–906.
63. F. Zhang and T. S. Dibble, *Phys. Chem. Chem. Phys.*, 2011, **13**, 17969–17977.
64. A. G. Vandeputte, M. K. Sabbe, M. F. Reyniers, V. Van Speybroeck, M. Waroquier and G. B. Marin, *J. Phys. Chem. A*, 2007, **111**, 11771–11786.
65. C. Gonzalez and H. B. Schlegel, *J. Chem. Phys.*, 1991, **95**, 5853–5860.
66. C. Gonzalez and H. Bernhard Schlegel, *J. Chem. Phys.*, 1989, **90**, 2154–2161.
67. E. Wigner, *J. Chem. Phys.*, 1937, **5**, 726–736.
68. S. Canneaux, F. Bohr and E. Henon, *J. Comput. Chem.*, 2014, **35**, 82–93**.**

Chapter 4:

1. M. M. Abu-omar, A. Loaiza and N. Hontzeas, *Chem. Rev.,* 2005, **105**, 2227-2252.
2. C. Krebs, D. G. Fujimori, C. T. Walsh and J. M. Bollinger, *Acc. Chem. Res.*, 2007, **40**, 484–492.
3. M. T. Green, *Curr. Opin. Chem. Biol.*, 2009, **13**, 84–88.
4. P. R. O. De Montellano, *Chem. Rev.*, 2010, **110**, 932–948.
5. S. Shaik, W. Lai, H. Chen and Y. Wang, *Acc. Chem. Res.*, 2010, **43**, 1154–1165.
6. J. M. Mayer, *Acc. Chem. Res.*, 2011, **44**, 36–46.
7. C. Wang, *Synlett*, 2013, **24**, 1606–1613.
8. J. J. Warren, T. A. Tronic and J. M. Mayer, *Chem. Rev.*, 2010, **110**, 6961–7001.
9. A. Gunay and K. H. Theopold, *Chem. Rev.*, 2010, **110**, 1060–1081.
10. K. L. Stone and A. S. Borovik, *Curr. Opin. Chem. Biol.*, 2009, **13**, 114–118.
11. A. R. McDonald and L. Que, *Coord. Chem. Rev.*, 2013, **257**, 414–428.
12. D. Mandal, R. Ramanan, D. Usharani, D. Janardanan, B. Wang and S. Shaik, *J. Am. Chem. Soc*., 2015, **137**, 722– 733.
13. B. K. Mai and Y. Kim, *Angew. Chem., Int. Ed.,* 2015, **54**, 3946–3951.
14. R. Kumar, B. Pandey, A. Sen, M. Ansari, S. Sharma and G. Rajaraman, *Coord. Chem. Rev.*, 2020, **419**, 213397.

15. H. Park and D. Lee, *Chem. Eur. J.*, 2020, **26**, 5916–5926.
16. C. V Sastri, J. Lee, K. Oh, Y. Jin Lee, J. Lee, T. A. Jackson, K. Ray, H. Hirao, W. Shin, J. A. Halfen, J. Kim, L. Que, S. Shaik and W. Nam, *PNAS.,* 2007, **104**, 19181-19186.
17. H. Hirao, L. Que, W. Nam and S. Shaik, *Chem. Eur. J.*, 2008, **14**, 1740–1756.
18. W. Nam, Y. M. Lee and S. Fukuzumi, *Acc. Chem. Res.*, 2014, **47**, 1146–1154.
19. S. Hong, Y. M. Lee, K. B. Cho, K. Sundaravel, J. Cho, M. J. Kim, W. Nam, *J. Am. Chem. Soc*., 2011, **133**, 11876-11879.
20. S. Sahu, M. G. Quesne, C. G. Davies, M. Dürr, I. Ivanović-Burmazović, M. A. Siegler, G. N. L. Jameson, S. P. De Visser and D. P. Goldberg, *J. Am. Chem. Soc.*, 2014, **136**, 13542–13545.
21. S. Sahu, L. R. Widger, M. G. Quesne, S. P. De Visser, H. Matsumura, P. Moënne-Loccoz, M. A. Siegler and D. P. Goldberg, *J. Am. Chem. Soc.*, 2013, **135**, 10590–10593.
22. J. U. Rohde, J. H. In, M. H. Lim, W. W. Brennessel, M. R. Bukowski, A. Stubna, E. Münck, W. Nam and L. Que, *Science.*, 2003, **299**, 1037–1039.
23. M. Bukowski R., K. Koehntop D., A. Stubna, E. Bominaar L., J. Halfen A., E. Münck, W. Nam and L. Que Jr., *Science.*, 2005, **310**, 1000–1002.
24. L. Que, *Acc. Chem. Res.,* 2007, **40**, 493–500.
25. W. Nam, Acc. Chem. Res., 2007, **40**, 522–531.
26. M. Puri and L. Que, *Acc. Chem. Res.*, 2015, **48**, 2443–2452.
27. W. Nam, Y. M. Lee and S. Fukuzumi, *Acc. Chem. Res.*, 2018, **51**, 2014–2022.
28. K. Ray, Y. M. Lee and W. Nam, *Coord. Chem. Rev.*, 2017, **334**, 25–42.
29. X. Engelmann, I. Monte-Pérez and K. Ray, *Angew. Chem., Int. Ed.,* 2016, **55**, 7632–7649.
30. S. P. De Visser, *J. Am. Chem. Soc.*, 2006, **128**, 15809–15818.
31. M. S. Seo, J. Y. Kim, J. Annaraj, Y. Kim, Y.-M. Lee, S.-J. Kim, J. Kim and W. Nam, *Angew. Chem., Int. Ed.,* 2007, **119**, 381–384.
32. B. Wang, Y. M. Lee, W. Y. Tcho, S. Tussupbayev, S. T. Kim, Y. Kim, M. S. Seo, K. Bin Cho, Y. Dede, B. C. Keegan, T. Ogura, S. H. Kim, T. Ohta, M. H. Baik, K. Ray, J. Shearer and W. Nam, *Nat. Commun.*, 2017, **8**, 14839.
33. S. P. De Visser, *JPP.*, 2013, **17**, 954–963.
34. S. N. Dhuri, K. Bin Cho, Y. M. Lee, S. Y. Shin, J. H. Kim, D. Mandal, S. Shaik and W. Nam, *J. Am. Chem. Soc.*, 2015, **137**, 8623–8632.
35. P. E. M. Siegbahn, *J. Am. Chem. Soc.*, 2009, **131**, 18238–18239.

36. P. E. M. Siegbahn and R. H. Crabtree, *J. Am. Chem. Soc.,* 1999, **2**, 117–127.
37. P. Barman, A. K. Vardhaman, B. Martin, S. J. Wörner, C. V. Sastri and P. Comba, *Angew. Chem., Int. Ed.*, 2015, **127**, 2123–2127.
38. S. Shi, Y. Wang, A. Xu, H. Wang, D. Zhu, S. B. Roy, T. A. Jackson, D. H. Busch and G. Yin, *Angew. Chem., Int. Ed.,* 2011, **123**, 7459–7462.
39. S. C. Sawant, X. Wu, J. Cho, K.-B. Cho, S. H. Kim, M. S. Seo, Y.-M. Lee, M. Kubo, T. Ogura, S. Shaik and W. Nam, *Angew. Chem., Int. Ed.,* 2010, **122**, 8366–8370.
40. D. F. Leto, R. Ingram, V. W. Day and T. A. Jackson, *Chem. Commun.*, 2013, **49**, 5378–5380.
41. H. Yoon, Y. M. Lee, X. Wu, K. Bin Cho, R. Sarangi, W. Nam and S. Fuhkuzumi, *J. Am. Chem. Soc.*, 2013, **135**, 9186–9194.
42. M. Guo, T. Corona, K. Ray and W. Nam, *ACS Cent. Sci.*, 2019, **5**, 13–28.
43. X. Wu, M. S. Seo, K. M. Davis, Y. M. Lee, J. Chen, K. Bin Cho, Y. N. Pushkar and W. Nam, *J. Am. Chem. Soc.*, 2011, **133**, 20088–20091.
44. M. Guo, M. S. Seo, Y. M. Lee, S. Fukuzumi and W. Nam, *J. Am. Chem. Soc.*, 2019, **141**, 12187–12191.
45. J. Chen, Z. Jiang, S. Fukuzumi, W. Nam and B. Wang, *Coord. Chem. Rev.*, 2020, **421**, 213443.
46. S. Liu, K. Mase, C. Bougher, S. D. Hicks, M. M. Abu-Omar and S. Fukuzumi, *Inorg. Chem.*, 2014, **53**, 7780–7788.
47. K. Bin Cho, H. Kang, J. Woo, Y. J. Park, M. S. Seo, J. Cho and W. Nam, *Inorg. Chem.*, 2014, **53**, 645–652.
48. T. Ishizuka, H. Kotani and T. Kojima, *Dalt. Trans.*, 2016, **45**, 16727–16750.
49. T. Ishizuka, H. Sugimoto, S. Itoh and T. Kojima, *Coord. Chem. Rev.*, 2022, **466**, 214536.
50. F. Ogliaro, S. P. de Visser, J. T. Groves and S. Shaik, *Angew. Chem., Int. Ed.,* 2001, **113**, 2958–2962.
51. P. K. Sharma, S. P. De Visser, F. Ogliaro and S. Shaik, *J. Am. Chem. Soc.*, 2003, **125**, 2291–2300.
52. T. Kojima, H. Kotani, H. Shimomura, K. Ikeda, T. Ishizuka, Y. Shiota and K. Yoshizawa, *J. Am. Chem. Soc.*, 2020, **142**, 16982–16989.
53. T. Kojima, K. Nakayama, K. Ikemura, T. Ogura and S. Fukuzumi, *J. Am. Chem. Soc.*, 2011, **133**, 11692–11700.
54. S. Ohzu, T. Ishizuka, Y. Hirai, H. Jiang, M. Sakaguchi, T. Ogura, S. Fukuzumi and T. Kojima,

Chem. Sci., 2012, **3**, 3421–3431.

55. S. N. Dhuri, S. S. Mi, Y. M. Lee, H. Hirao, Y. Wang, W. Nam and S. Shaik, *Angew. Chem., Int. Ed.,* 2008, **47**, 3356–3359.
56. W. K. Seok, A. K. Gupta, S. J. Roh, W. Lee and S. H. Han, *Bull. Korean Chem. Soc.*, 2007, **28**, 1311–1316.
57. D. Mandal and S. Shaik, *J. Am. Chem. Soc.*, 2016, **138**, 2094–2097.
58. L. Roecker and T. J. Meyer, *J. Am. Chem. Soc.*, 1987, **109**, 746–754.
59. M. R. Jo and W. K. Seok, *Bull. Korean Chem. Soc.*, 2011, **32**, 3003–3008.
60. A. D. Becke, *J. Chem. Phys.*, 1993, **98**, 1372–1377.
61. C. Lee, Eitao Yang and R. G. Parr, *Phys. Rev. B: Condens. Matter Mater. Phys.,* 1988, **37**, 785.
62. J. D. Dill and J. A. Pople, *J. Chem. Phys.*, 1975, **62**, 2921–2923.
63. P. J. Hay and W. R. Wadt, *J. Chem. Phys.*, 1985, **82**, 270–283.
64. D. Janardanan, D. Usharani, H. Chen and S. Shaik, *J. Phys. Chem. Lett.*, 2011, **2**, 2610–2617.
65. P. Fuentealba, H. Preuss, H. Stoll and L. Von Szentpály, *Chem. Phys. Lett.*, 1982, **89**, 418–422.
66. J. Tomasi, B. Mennucci and R. Cammi, *Chem. Rev.*, 2005, **105**, 2999–3093.
67. M. J. Frisch, G. W. Trucks, H. B. Schlegel, G. E. Scuseria, M. A. Robb, J. R. Cheeseman, G. Scalmani, V. Barone, G. A. Petersson, H. Nakatsuji, X. Li, M. Caricato, A. V. Marenich, J. Bloino, B. G. Janesko, R. Gomperts, B. Mennucci, H. P. Hratchian, J. V. Ortiz, A. F. Izmaylov, J. L. Sonnenberg, D. Williams-Young, F. Ding, F. Lipparini, F. Egidi, J. Goings, B. Peng, A. Petrone, T. Henderson, D. Ranasinghe, V. G. Zakrzewski, J. Gao, N. Rega, G. Zheng, W. Liang, M. Hada, M. Ehara, K. Toyota, R. Fukuda, J. Hasegawa, M. Ishida, T. Nakajima, Y. Honda, O. Kitao, H. Nakai, T. Vreven, K. Throssell, J. A. Montgomery Jr., J. E. Peralta, F. Ogliaro, M. J. Bearpark, J. J. Heyd, E. N. Brothers, K. N. Kudin, V. N. Staroverov, T. A. Keith, R. Kobayashi, J. Normand, K. Raghavachari, A. P. Rendell, J. C. Burant, S. S. Iyengar, J. Tomasi, M. Cossi, J. M. Millam, M. Klene, C. Adamo, R. Cammi, J. W. Ochterski, R. L. Martin, K. Morokuma, O. Farkas, J. B. Foresman and D. J. Fox, Gaussian 16, Revision C.01, Gaussian, Inc., Wallingford, CT, 2016.
68. L. Falivene, Z. Cao, A. Petta, L. Serra, A. Poater, R. Oliva, V. Scarano and L. Cavallo, *Nat. Chem.*, 2019, **11**, 872–879.
69. R. A. Massoud and M. A. Makhyoun, *J. Struct. Chem.*, 2019, **60**, 882–889.
70. H. Eyring, *J. Chem. Phys.*, 1935, **3**, 63–71.

71. C. Eckart, Phys. Rev., 1930, 35, 1303–1309.
72. D. K. Maity, R. L. Bell and T. N. Truong, *J. Am. Chem. Soc.*, 2000, **122**, 897–906.
73. F. Zhang and T. S. Dibble, *Phys. Chem. Chem. Phys.*, 2011, **13**, 17969–17977.
74. A. G. Vandeputte, M. K. Sabbe, M. F. Reyniers, V. Van Speybroeck, M. Waroquier and G. B. Marin, *J. Phys. Chem. A*, 2007, **111**, 11771–11786.
75. C. Gonzalez and H. B. Schlegel, *J. Chem. Phys.*, 1991, **95**, 5853–5860.
76. C. Gonzalez and H. Bernhard Schlegel, *J. Chem. Phys.*, 1989, **90**, 2154–2161.
77. E. Wigner, *J. Chem. Phys.*, 1937, **5**, 726–736.
78. S. Canneaux, F. Bohr and E. Henon, *J. Comput. Chem.*, 2014, **35**, 82–93.
79. S. Shaik, H. Chen and D. Janardanan, *Nat. Chem.*, 2011, **3**, 19–27.
80. D. Mandal, D. Mallick and S. Shaik, *Acc. Chem. Res.*, 2018, **51**, 107–117.
81. P. Brandi, C. Galli and P. Gentili, *J. Org. Chem.*, 2005, **70**, 9521–9528.
82. A. Barbieri, O. Lanzalunga, A. Lapi and S. Di Stefano, *J. Org. Chem.*, 2019, **84**, 13549–13556.
83. S. P. De Visser, L. Tahsini and W. Nam, *Chem. Eur. J.*, 2009, **15**, 5577–5587.
84. Y. -R. Luo, *Comprehensive Handbook of Chemical Bond Energies*, Taylor & Francis, Boca Raton, 2007.
85. J. E. M. N. Klein, D. Mandal, W. M. Ching, D. Mallick, L. Que and S. Shaik, *J. Am. Chem. Soc.*, 2017, **139**, 18705–18713.

Chapter 5:

1. C. Krebs, D. G. Fujimori, C. T. Walsh and J. M. Bollinger, *Acc. Chem. Res.*, 2007, **40**, 484–492.
2. L. Que, Acc. *Chem. Res.*, 2007, **40**, 493–500.
3. W. Nam, *Acc. Chem. Res*., 2007, **40**, 522–531.
4. D. C. Lacy, R. Gupta, K. L. Stone, J. Greaves, J. W. Ziller, M. P. Hendrich and A. S. Borovik, *J. Am. Chem. Soc*., 2010, **132**, 12188–12190.
5. W. Nam, Y. M. Lee and S. Fukuzumi, *Acc. Chem. Res*., 2014, **47**, 1146–1154.
6. W. N. Oloo and L. Que, *Acc. Chem. Res*., 2015, **48**, 2612– 2621.
7. A. S. Borovik, *Chem. Soc. Rev.*, 2011, **40**, 1870–1874.
8. L. Ji, A. Franke, M. Brindell, M. Oszajca, A. Zahl and R. Van Eldik, *Chem. – Eur. J.*, 2014, **20**, 14437–14450.

9. X. Shan and L. Que, *J. Inorg. Biochem*., 2006, **100**, 421–433.
10. R. H. Holm, P. Kennepohl and E. I. Solomon, *Chem. Rev.*, 1996, **96**, 2239–2314.
11. E. I. Solomon, T. C. Brunold, M. I. Davis, J. N. Kemsley, S. -K. Lee, N. Lehnert, F. Neese, A. J. Skulan, Y. -S. Yang and J. Zhou, *Chem. Rev.*, 2000, **100**, 235–349.
12. M. Costas, M. P. Mehn, M. P. Jensen and L. Que, *Chem. Rev.*, 2004, **104**, 939–986.
13. L. Que and R. Y. N. Ho, *Chem. Rev.*, 1996, **96**, 2607–2624.
14. E. L. Hegg and L. Que, *Eur. J. Biochem.*, 1997, **250**, 625–629.
15. L. Que, *Nat. Struct. Biol.*, 2000, **7**, 182–184.
16. K. D. Koehntop, J. P. Emerson and L. Que, *J. Biol. Inorg. Chem.*, 2005, **10**, 87–93.
17. P. C. A. Bruijnincx, G. van Koten and R. J. M. Klein Gebbink, *Chem. Soc. Rev.*, 2008, **37**, 2716–2744.
18. S. Kal and L. Que, *J. Biol. Inorg. Chem.*, 2017, **22**, 339–365.
19. J. M. Bollinger Jr, J. C. Price, L. M. Hoffart, E. W. Barr and C. Krebs, *Eur. J. Inorg. Chem.,* 2005, 4245–4254.
20. J. M. Bollinger Jr and C. Krebs, *J. Inorg. Biochem.*, 2006, **100**, 586–605.
21. J. N. Barlow, Z. Zhang, P. John, J. E. Baldwin and C. J. Schofield, *Biochemistry*, 1997, **36**, 3563–3569.
22. G. Capitani, E. Hohenester, L. Feng, P. Storici, J. F. Kirsch and J. N. Jansonius, *J. Mol. Biol.*, 1999, **294**, 745–756.
23. O. A. Andersen, T. Flatmark and E. Hough, *J. Mol. Biol.*, 2001, **34**, 279–291.
24. J. C. Price, E. W. Barr, B. Tirupati, J. M. Bollinger and C. Krebs, *Biochemistry*, 2003, **42**, 7497–7508.
25. J. C. Price, E. W. Barr, T. E. Glass, C. Krebs and J. M. Bollinger, *J. Am. Chem. Soc.*, 2003, **125**, 13008–13009.
26. P. J. Riggs-Gelasco, J. C. Price, R. B. Guyer, J. H. Brehm, E. W. Barr, J. M. Bollinger and C. Krebs, *J. Am. Chem. Soc.*, 2004, **126**, 8108–8109.
27. J. C. Price, E. W. Barr, L. M. Hoffart, C. Krebs and J. M. Bollinger, *Biochemistry*, 2005, **44**, 8138–8147.
28. S. Sinnecker, N. Svensen, E. W. Barr, S. Ye, J. M. Bollinger, F. Neese and C. Krebs, *J. Am. Chem. Soc.*, 2007, **129**, 6168–6179.
29. L. M. Hoffart, E. W. Barr, R. B. Guyer, J. M. Bollinger and C. Krebs, *Proc. Natl. Acad. Sci.*

U. S. A., 2006, **103**, 14738–14743.

30. D. P. Galonic, E. W. Barr, C. T. Walsh, J. M. Bollinger and C. Krebs, *Nat. Chem. Biol.*, 2007, **3**, 113–116.
31. D. G. Fujimori, E. W. Barr, M. L. Matthews, G. M. Koch, J. R. Yonce, C. T. Walsh, J. M. Bollinger, C. Krebs and P. J. Riggs-Gelasco, *J. Am. Chem. Soc.*, 2007, **129**, 13408–13409.
32. J. R. Hagadorn, L. Que and W. B. Tolman, *Inorg. Chem.*, 2000, **39**, 6086–6090.
33. J. R. Hagadorn, L. Que, W. B. Tolman and *J. Am. Chem. Soc.*, 1998, 1**20**, 13531–13532.
34. J. R. Hagadorn, L. Que, W. B. Tolman, I. Prisecaru and E. Münck, *J. Am. Chem. Soc.*, 1999, **121**, 9760–9761.
35. A. Beck, B. Weibert and N. Burzlaff, *Eur. J. Inorg. Chem.*, 2001, 521–527.
36. A. Beck, A. Barth, E. Hubner and N. Burzlaff, *Inorg. Chem.*, 2003, **42**, 7182–7188.
37. S. J. Friese, B. E. Kucera, L. Que and W. B. Tolman, *Inorg. Chem.*, 2006, **45**, 8003–8005.
38. P. C. A. Bruijnincx, M. Lutz, A. L. Spek, W. R. Hagen, B. M. Weckhuysen, G. Van Koten and R. J. M. K. Gebbink, *J. Am. Chem. Soc.*, 2007, **129**, 2275–2286.
39. S. Friedle, E. Reisner and S. J. Lippard, *Chem. Soc. Rev.*, 2010, **39**, 2768–2779.
40. A. R. McDonald, Y. Guo, V. V. Vu, E. L. Bominaar, E. Münck and L. Que, *Chem. Sci.*, 2012, **3**, 1680–1693.
41. I. Monte Pérez, X. Engelmann, Y. M. Lee, M. Yoo, E. Kumaran, E. R. Farquhar, E. Bill, J. England, W. Nam, M. Swart and K. Ray, *Angew. Chem., Int. Ed.*, 2017, **56**, 14384–14388.
42. L. Kaur and D. Mandal, *Dalton. Trans.*, 2024, **53**, 7527–7535.
43. J. U. Rohde and L. Que, *Angew. Chemie - Int. Ed.*, 2005, **44**, 2255–2258.
44. P. J. Cappillino, J. S. McNally, F. Wang and J. P. Caradonna, *J. Chem. Soc. Dalton. Trans.*, 2012, **41**, 474–483.
45. D. Mandal, R. Ramanan, D. Usharani, D. Janardanan, B. Wang and S. Shaik, *J. Am. Chem. Soc.*, 2015, **137**, 722– 733.
46. D. Mandal and S. Shaik, *J. Am. Chem. Soc.*, 2016, **138**, 2094–2097.
47. M. J. Frisch, G. W. Trucks, H. B. Schlegel, G. E. Scuseria, M. A. Robb, J. R. Cheeseman, G. Scalmani, V. Barone, G. A. Petersson, H. Nakatsuji, X. Li, M. Caricato, A. V. Marenich, J. Bloino, B. G. Janesko, R. Gomperts, B. Mennucci, H. P. Hratchian, J. V. Ortiz, A. F. Izmaylov, J. L. Sonnenberg, D. Williams-Young, F. Ding, F. Lipparini, F. Egidi, J. Goings, B. Peng, A. Petrone, T. Henderson, D. Ranasinghe, V. G. Zakrzewski, J. Gao, N. Rega, G. Zheng, W. Liang,

M. Hada, M. Ehara, K. Toyota, R. Fukuda, J. Hasegawa, M. Ishida, T. Nakajima, Y. Honda, O. Kitao, H. Nakai, T. Vreven, K. Throssell, J. A. Montgomery Jr., J. E. Peralta, F. Ogliaro, M. J. Bearpark, J. J. Heyd, E. N. Brothers, K. N. Kudin, V. N. Staroverov, T. A. Keith, R. Kobayashi, J. Normand, K. Raghavachari, A. P. Rendell, J. C. Burant, S. S. Iyengar, J. Tomasi, M. Cossi, J. M. Millam, M. Klene, C. Adamo, R. Cammi, J. W. Ochterski, R. L. Martin, K. Morokuma, O. Farkas, J. B. Foresman and D. J. Fox, *Gaussian 16, Revision C.01*, Gaussian, Inc., Wallingford, CT, 2016.

48. A. D. Becke, *J. Chem. Phys*., 1993, **98**, 1372–1377.
49. C. Lee, E. Yang and R. G. Parr, *Phys. Rev. B: Condens. Matter Mater. Phys*., 1988, **37**, 785.
50. A. Altun, J. Breidung, F. Neese and W. Thiel, *J. Chem. Theory Comput.*, 2014, **10**, 3807–3820.
51. Y. Cao, J. A. Valdez-Moreira, S. Hay, J. M. Smith and S. P. de Visser, *Chem. – Eur. J.*, 2023, **29**, No. e202300271.
52. K. Bleher, P. Comba, D. Kass, K. Ray and H. Wadepohl, J. Inorg. Biochem., 2023, **241**, 112123.
53. D. Mandal, D. Mallick and S. Shaik, *Acc. Chem. Res.*, 2018, **51**, 107–117.
54. C. Wegeberg, M. L. Skavenborg, A. Liberato, J. N. McPherson, W. R. Browne, E. D. Hedegård and C. J. McKenzie, *Inorg. Chem.*, 2021, **60**, 1975–1984.
55. A. Katoch and D. Mandal, *Dalton Trans*., 2022, **51**, 11641– 11649.
56. A. Katoch and D. Mandal, *Dalton Trans*., 2024, **53**, 2386-2394.
57. L. Kaur and D. Mandal, *Inorg. Chem.,* 2022, **61**, 14582-14590.
58. L. Kaur and D. Mandal, *Dalton Trans*., 2024, **53**, 7527-7535.
59. P. J. Hay and W. R. Wadt, *J. Chem. Phys*., 1985, **82**, 270–283.
60. J. D. Dill and J. A. Pople, *J. Chem. Phys*., 1975, **62**, 2921– 2923.
61. P. Fuentealba, H. Preuss, H. Stoll and L. Von Szentpály, *Chem. Phys. Lett*., 1982, **89**, 418–422.
62. J. Tomasi, B. Mennucci and R. Cammi, *Chem. Rev*., 2005, **105**, 2999–3093.
63. D. Janardanan, D. Usharani, H. Chen and S. Shaik, *J. Phys. Chem. Lett*., 2011, **2**, 2610–2617.
64. L. Falivene, Z. Cao, A. Petta, L. Serra, A. Poater, R. Oliva, V. Scarano and L. Cavallo, *Nat. Chem*., 2019, **11**, 872–879.
65. R. A. Massoud and M. A. Makhyoun, *J. Struct. Chem*., 2019, **60**, 882–889.
66. S. Canneaux, F. Bohr and E. Henon, *J. Comput. Chem*., 2014, **35**, 82–93.
67. H. Eyring, *J. Chem. Phys*., 1935, **3**, 63–71.

68. D. K. Maity, R. L. Bell and T. N. Truong, *J. Am. Chem. Soc*., 2000, **122**, 897–906.
69. F. Zhang and T. S. Dibble, *Phys. Chem. Chem. Phys*., 2011, **13**, 17969–17977.
70. A. G. Vandeputte, M. K. Sabbe, M. F. Reyniers, V. Van Speybroeck, M. Waroquier and G. B. Marin, *J. Phys. Chem. A*, 2007, **111**, 11771–11786.
71. L. Cheng, C. Doubleday and R. Breslow, *Proc. Natl. Acad. Sci. U. S. A.*, 2015, **112**, 4218–4220.
72. S. Shaik, H. Chen and D. Janardanan, *Nat. Chem.*, 2011, **3**, 19–27.
73. Y. -R. Luo, *Comprehensive Handbook of Chemical Bond Energies*, Taylor & Francis, Boca Raton, 2007.
74. A. Barbieri, O. Lanzalunga, A. Lapi and S. Di Stefano, *J. Org. Chem*., 2019, **84**, 13549–13556.
75. E. J. Klinker, Ph.D. Dissertation. Department of Chemistry, University of Minnesota, Minneapolis, MN.

Chapter 6:

1. Nam, W. *Acc. Chem. Res.,* 2007, **40**, 522–531.
2. Krebs, C.; Galonić F. D.; Walsh, C. T.; Bollinger, J. M., Jr. *Acc. Chem. Res*., 2007, **40**,484−492.
3. Green, M. T. *Curr. Opin. Chem. Biol*., 2009, **13**, 84−88.
4. Montellano, P. R. O. De. *Chem. Rev.,* 2010, **110**, 932–948.
5. Shaik, S.; Lai, W.; Chen, H.; Wang, Y. *Acc. Chem. Res*., 2010, **43**, 1154−1165.
6. Que, L., Jr. *Acc. Chem. Res*., 2007, **40**, 493−500.
7. Mayer, J. M. *Acc. Chem. Res*., 2011, **44**, 36−46.
8. Wang, C. *Synlett.,* 2013, **24**, 1606–1613.
9. Warren, J. J.; Tronic, T. A.; Mayer, J. M. *Chem. Rev*., 2010, **110**, 6961−7001.
10. Gunay, A.; Theopold, K. H. *Chem. Rev.,* 2010, **110**, 1060–1081.
11. Stone, K. L.; Borovik, A. S. *Curr. Opin. Chem. Biol.,* 2009, **13**, 114–118.
12. McDonald, A. R.; Que, L., Jr. *Coord. Chem. Rev*., 2013, **257**, 414−428.
13. Katoch, A.; Mandal, D. *Dalton. Trans.,* 2022, **51**, 11641–11649.
14. Katoch, A.; Mandal, D. *Dalton. Trans.,* 2024, **53**, 2386–2394.
15. Mandal, D.; Ramanan, R.; Usharani, D.; Janardanan, D.; Wang, B.; Shaik, S. *J. Am. Chem. Soc.,* 2015, **137**, 722–733.
16. Klein, J. E. M. N.; Mandal, D.; Ching, W. M.; Mallick, D.; Que, L.; Shaik, S. *J. Am. Chem.*

Soc., 2017, **139**, 18705–18713.

17. Nam, W.; Lee, Y. M.; Fukuzumi, S. *Acc. Chem. Res.,* 2014, **47**, 1146–1154.
18. Hong, S.; Lee, Y.-M.; Cho, K.-B.; Sundaravel, K.; Cho, J.; Kim, M. J.; Shin, W.; Nam, W. *J. Am. Chem. Soc*., 2011, **133**, 11876−11879.
19. Sahu, S.; Quesne, M. G.; Davies, C. G.; Dürr, M.; Ivanović -Burmazović, I.; Siegler, M. A.; Jameson, G. N. L.; de Visser, S. P.; Goldberg, D. P. *J. Am. Chem. Soc*., 2014, **136**, 13542−13545.
20. Sahu, S.; Widger, L. R.; Quesne, M. G.; de Visser, S. P.; Matsumura, H.; Moënne-Loccoz, P.; Siegler, M. A.; Goldberg, D. P. *J. Am. Chem. Soc*., 2013, **135**, 10590−10593.
21. Mandal, D.; Mallick, D.; Shaik, S. *Acc. Chem. Res.,* 2018, **51**, 107–117.
22. Sastri, C. V.; Lee, J.; Oh, K.; Lee, Y. J.; Lee, J.; Jackson, T. A.; Ray,K.; Hirao, H.; Shin, W.; Halfen, J. A.; Kim, J.; Que, L., Jr.; Shaik, S.; Nam,W. *Proc. Nat. Acad. Sci. U.S.A.,* 2007, **104**, 19181−19186.
23. Hirao, H.; Que, L.; Nam, W.; Shaik, S. *Chem. - Eur.J.,* 2008, **14**, 1740−1756.
24. Kumar, R.; Pandey, B.; Sen, A.; Ansari, M.; Sharma, S.; Rajaraman, G. *Coord. Chem. Rev.,* 2020, **419**, 213397.
25. Park, H.; Lee, D. *Chem. - Eur. J.,* 2020, **26**, 5916−5926.
26. Kaur, L.; Mandal, D. *Inorg. Chim. Acta.,* 2024, **572**, 122292.
27. Kaur, L.; Mandal, D. *Dalton. Trans.,* 2024, **53**, 7527–7535.
28. Kaur, L.; Mandal, D. *Inorg. Chem0.,* 2022, **61**, 14582–14590.
29. Barbieri, A.; Lanzalunga, O.; Lapi, A.; Di Stefano, S. *J. Org. Chem.,* 2019, **84**, 13549−13556.
30. Mancini, M. D. B.; Bernardini, M.; Birzu, B. E.; Santis, A. D.; Stefano, S. D.; Frateloreto, F.; Khaksar, D.; Lapi, A.; Olivo, G.; Lanzalunga, O. *Eur. J. Org. Chem*., 2023, **26***,* 1-10.
31. Mancini, M. D. B.; Gelsomino, A. D.; Stefano, S. D.; Frateloreto, F.; Lapi, A.; Lanzalunga, O.; Olivo, G.; Sajeva, S. *ACS Omega.,* 2021, **6**, 26428–26438.
32. Bae, J. M.; Lee, M. M.; Lee, S. A.; Lee, S. Y.; Bok, K. H.; Kim,J.; Kim, C. *Inorg. Chim. Acta.*, 2016, **451**, 8−15.
33. Annunziatini, C.; Gerini, M. F.; Lanzalunga, O.; Lucarini, M. J. *J. Org. Chem.,* 2004, **69**, 3431–3438.
34. Cai, Y.; Koshino, N.; Saha, B.; Espenson, J. H. *J. Org. Chem.,* 2005, **70**, 238–243.
35. Bietti, M.; Forcina, V.; Lanzalunga, O.; Lapi, A.; Martin, T.; Mazzonna, M.; Salamone, M. *J.*

Org. Chem., 2016, **81**, 11924–11931.

36. Kushch, O. V.; Hordieieva, I. O.; Kompanets, M. O.; Zosenko, O. O.; Opeida, I. A.; Shendrik, A. N. *J. Org. Chem.,* 2021, **86**, 3792–3799.
37. Baciocchi, E.; Gerini, M. F.; Lanzalunga, O. *J. Org. Chem*., 2004, **69**, 8963−896.
38. D'Alfonso, C.; Bietti, M.; DiLabio, G. A.; Lanzalunga, O.;Salamone, M. *J. Org. Chem.,* 2013, **78**, 1026−1037.
39. Galli, C.; Gentili, P.; Lanzalunga, O. *Angew. Chem., Int. Ed.,* 2008, **47**, 4790−4796.
40. Cho, K.-B.; Wu, X.; Lee, Y.-M.; Kwon, Y. H.; Shaik, S.; Nam, W. *J. Am. Chem. Soc*., 2012, **134**, 20222−20225.
41. Kwon, Y. H.; Mai, B. K.; Lee, Y. M.; Dhuri, S. N.; Mandal, D.; Cho, K. Bin; Kim, Y.; Shaik, S.; Nam, W. *J. Phys. Chem. Lett.,* 2015, **6**, 1472–1476.
42. Hermans, I.; Vereecken, L.; Jacobs, P. A.; Peeters, J. *Chem. Commun.,* 2004, **4**, 1140–1141.
43. Mazzonna, M.; Bietti, M.; DiLabio, G. A.; Lanzalunga, O.; Salamone, M. *J. Org. Chem*., 2014, **79**, 5209−5218.
44. Minisci, F.; Punta, C.; Recupero, F. *J. Mol. Catal. A Chem.,* 2006, **251**, 129–149.
45. Minisci, F.; Punta, C.; Recupero, F.; Fontana, F.; Pedulli, G. F. *Chem. Commun.,* 2002, **7**, 688–689.
46. White, M. C.; Zhao, J. *J. Am. Chem. Soc.,* 2018, **140**, 13988−14009.
47. Dantignana, V.; Pérez-Segura, M. C.; Besalú-Sala, P.; Delgado-Pinar, E.; Martínez-Camarena, Á.; Serrano-Plana, J.; Álvarez-Núñez, A.; Castillo, C. E.; García-España, E.; Luis, J. M.; Basallote, M. G.; Costas, M.; Company, A. *Angew. Chem., Int. Ed.,* 2023, **135**, 1-10.
48. Kupper, C.; Mondal, B.; Serrano-Plana, J.; Klawitter, I.; Neese, F.; Costas, M.; Ye, S.; Meyer, F. *J. Am. Chem. Soc.,* 2017, **139**, 8939–8949.
49. Usharani, D.; Lacy, D. C.; Borovik, A. S.; Shaik, S. *J. Am. Chem. Soc.,* 2013, **135**, 17090–17104.
50. Dilabio, G. A.; Franchi, P.; Lanzalunga, O.; Lapi, A.; Lucarini, F.; Lucarini, M.; Mazzonna, M.; Prasad, V. K.; Ticconi, B. *J. Org. Chem.,* 2017, **82**, 6133–6141.
51. Becke, A. D. *J. Chem. Phys.,* 1993, **98**, 1372−1377.
52. Lee, C. T.; Yang, W. T.; Parr, R. G. *Phys. Rev. B.,* 1988, **37**, 785−789.
53. Altun, A.; Breidung, J.; Neese, F.; Thiel, W. *J. Chem. Theory Comput.,* 2014, **10**, 3807−3820.
54. Chen, H.; Lai, W.; Shaik, S. *J. Phys. Chem. Lett*., 2010, **1**, 1533–1540.

55. Dill, J. D.; Pople, J. A. *J. Chem. Phys.,* 1975, **62**, 2921–2923.

56. Hay, P. J.; Wadt, W. R. *J. Chem. Phys.,* 1985, **82**, 270–283.

57. Janardanan, D.; Usharani, D.; Chen, H.; Shaik, S. *J. Phys. Chem. Lett.,* 2011, **2**, 2610–2617.

58. Fuentealba, P.; Preuss, H.; Stoll, H.; Von Szentpály, L. *Chem. Phys. Lett.,* 1982, **89**, 418-422.

59. Tomasi, J.; Mennucci, B.; Cammi, R. *Chem. Rev.,* 2005, **105**, 2999–3093.

60. Marenich, A. V.; Cramer, C. J.; Truhlar, D. G. *J. Phys. Chem. B.,* 2009, **113**, 6378–6396.

61. M. J. Frisch, G. W. Trucks, H. B. Schlegel, G. E. Scuseria, M. A. Robb, J. R. Cheeseman, G. Scalmani, V. Barone, G. A. Petersson, H. Nakatsuji, X. Li, M. Caricato, A. V. Marenich, J. Bloino, B. G. Janesko, R. Gomperts, B. Mennucci, H. P. Hratchian, J. V. Ortiz, A. F. Izmaylov, J. L. Sonnenberg, D. Williams-Young, F. Ding, F. Lipparini, F. Egidi, J. Goings, B. Peng, A. Petrone, T. Henderson, D. Ranasinghe, V. G. Zakrzewski, J. Gao, N. Rega, G. Zheng, W. Liang, M. Hada, M. Ehara, K. Toyota, R. Fukuda, J. Hasegawa, M. Ishida, T. Nakajima, Y. Honda, O. Kitao, H. Nakai, T. Vreven, K. Throssell, J. A. Montgomery Jr., J. E. Peralta, F. Ogliaro, M. J. Bearpark, J. J. Heyd, E. N. Brothers, K. N. Kudin, V. N. Staroverov, T. A. Keith, R. Kobayashi, J. Normand, K. Raghavachari, A. P. Rendell, J. C. Burant, S. S. Iyengar, J. Tomasi, M. Cossi, J. M. Millam, M. Klene, C. Adamo, R. Cammi, J. W. Ochterski, R. L. Martin, K. Morokuma, O. Farkas, J. B. Foresman and D. J. Fox, *Gaussian 16, Revision C.01*, Gaussian, Inc., Wallingford, CT, 2016.

62. Andrienko, G. A. Chemcraft Molecular Visualization Program, Version 1.8 (build 445).

63. Eyring, H. *J. Chem. Phys*., 1935, **3**, 107−115.

64. Eckart, C. *Phys. Rev.,* 1930, **35**, 1303−1309.

65. Canneaux, S.; Bohr, F.; Henon, E. *J. Comput. Chem.,* 2014, **35**, 82−93.

66. Cheng, L.; Doubleday, C.; and Breslow, R. *Proc. Natl. Acad. Sci. U. S. A.,* 2015, **112**, 4218–4220.

67. England, J.; Prakash, J.; Cranswick, M. A.; Mandal, D.; Guo,Y.; Munck, E.; Shaik, S.; Que, L., Jr. *Inorg. Chem*., 2015, **54**, 7828−7839.

68. Schröder, D.; Shaik, S.; Schwarz, H. *Acc. Chem. Res*., 2000, **33**,139−145.

69. Schulze, C.; Schwarz, H. *Angew. Chem. Inr. Ed. Engl.,* 1990, **29**, 509.

70. E. J. Klinker, Ph.D. Dissertation. Department of Chemistry, University of Minnesota, Minneapolis, MN.

71. Klinker, E. J.; Shaik, S.; Hirao, H.; Que, L. *Angew. Chem., Int. Ed*., 2009, **48**, 1291−1295.

72. Mandal, D.; Shaik, S. *J. Am. Chem. Soc*., 2016, **138**, 2094− 2097.

73. Dao, R.; Zhao, C.; Yao, J.; Li, H. *Phys. Chem. Chem. Phys.,* 2018, **20**, 28249−28256.

74. Mayer, J. M. *J. Phys. Chem. Lett*., 2011, **2**, 1481−1489.

75. Falivene, L.; Cao, Z.; Petta, A.; Serra, L.; Poater, A.; Oliva, R.; Scarano, V.; Cavallo, L. *Nat. Chem.,* 2019, **11**, 872–879.

76. Koshino, N.; Saha, B.; Espenson, J. H. *J. Org. Chem.,* 2003, **68**, 9364−9370.

- Transition metals are widely used in various fields, ranging from materials science to medicine, because of their versatile chemistry and ability to facilitate complex reactions. Among them, iron oxo complexes are particularly notable, especially in catalysis, where they are involved in key biological processes. For example, iron oxo species play a vital role in enzymes that catalyze important reactions like C-H activation, which is crucial for many biological transformations. This has led to the development of biomimetic catalysts designed to mimic these natural processes. In our thesis, we employed density functional theory (DFT) to explore C-H activation by iron(IV) oxo complexes, providing valuable insights into their reactivity and mechanisms.
- Building on these findings, our computational study using the DFT method reveals the potential for the rational design of metal-based catalysts. By systematically tuning ligands and substituents, we can optimize quantum mechanical tunneling effects, enhancing catalytic reactivity. Specifically, our results indicate that incorporating strong electron-donating groups can further improve catalytic efficiency. These insights pave the way for future research in the bioinorganic community, particularly in developing oxidants with tailored electronic properties.
- Further investigation into the natural preference of iron over ruthenium as a cofactor in C–H activation reactions not only deepens our understanding of the catalytic mechanisms involved but also opens the door for exploring other metal frameworks, such as Mn, Cr, and Co, through DFT calculations. The ability to apply these methods across a broader range of metal-oxo complexes presents an opportunity for gaining more comprehensive insights into their reactivity and mechanistic pathways.
- An amazing concept was observed to identify the potential of carboxylate-enriched Fe(IV)O complexes to increase reactivity, providing a detailed explanation of how this

enhancement occurs. These insights suggest that increasing the carboxylate content in metal-oxo catalysts could lead to the development of more efficient C–H activation catalysts. This work motivates the bioinorganic community to focus on the synthesis of oxidants with carboxylate-rich ligated macrocyclic compounds, further advancing the field.

- Moreover, the investigation into the role of N-hydroxy mediators in Fe(IV)O-catalyzed C–H activation reactions highlights their significant contribution to reactivity. The DFT analysis of these mediators, such as NHPI and NHQI, not only supports the proposed reaction mechanism but also emphasizes the need for further exploration of effective mediators. This comprehensive outlook paves the way for the rational design of metal-oxo catalysts with enhanced reactivity and efficiency, guiding future developments in the field.

1. **A. Katoch** and D. Mandal, Effect of the Substituent on C–H Activation Catalyzed by a Non-Heme Fe(IV)O Complex: A Computational Investigation of Reactivity and Hydrogen Tunneling, *Dalton Trans*., 2022, **51**, 11641– 11649.
2. **A. Katoch** and D. Mandal, High-Valent Nonheme Fe(IV)O/Ru(IV)O Complexes Catalyze C–H Activation Reactivity and Hydrogen Tunneling: A Comparative DFT Investigation, *Dalton Trans.*, 2024, **53**, 2386– 2394.
3. **A. Katoch** and D. Mandal, Impact of Carboxylate Ligation on the C–H Activation Reactivity of a Non-Heme Fe(IV)O Complex: A Computational Investigation, *Dalton Trans.,* 2024, **53**, 15264-15272.
4. **A. Katoch** and D. Mandal, Computational Insights into Hydrogen Atom Transfer Mediators in C−H Activation Catalysis of Nonheme Fe(IV)O Complexes, *J. Phys. Chem. B*., 2025, **129**, 88-95.

1. Atomistic Modelling Workshop on Amsterdam Modelling Suite Organized by Nyro Research India, Kochi, and SCM, Netherlands from 7th to 11th June 2021.
2. Workshop on Quantum Chemistry Thermodynamic Approach Organized by Zastra Innovations Pvt. Ltd from July 25th to 27th July 2023.
3. TCB (Theoretical Chemistry and Biology) Symposium Organized by NIPER Mohali on 15th October 2022.
4. International Conference on Molecules and Materials Technology Organized by Department of Chemistry National Institute of Technology, Kurukshetra held from 21st to 22nd April 2023.
5. International Conference on Advances in Chemical and Applied Sciences for Sustainable Development Organized by JECRC University, Jaipur, Rajasthan held from 29th to 30th March 2024.

Thesis_AK_DM_Plag.pdf

ORIGINALITY REPORT

14%	5%	13%	1%
SIMILARITY INDEX	INTERNET SOURCES	PUBLICATIONS	STUDENT PAPERS

PRIMARY SOURCES

1	Debasish Mandal, Rajeev Ramanan, Dandamudi Usharani, Deepa Janardanan, Binju Wang, Sason Shaik. "How Does Tunneling Contribute to Counterintuitive H-Abstraction Reactivity of Nonheme Fe(IV)O Oxidants with Alkanes?", Journal of the American Chemical Society, 2015 Publication	1%
2	Lovleen Kaur, Debasish Mandal. "Impact of ring size on the C H activation reactivity of iron(IV)–oxo complexes: A computational study with TMC macrocycles", Inorganica Chimica Acta, 2024 Publication	1%
3	pubs.acs.org Internet Source	1%
4	Debasish Mandal, Sason Shaik. "Interplay of Tunneling, Two-State Reactivity, and Bell–Evans–Polanyi Effects in C–H Activation by Nonheme Fe(IV)O Oxidants", Journal of the American Chemical Society, 2016 Publication	<1%
5	www.science.gov Internet Source	<1%
6	D. Balcells, O. Eisenstein. "Theoretical Studies on the Reaction Mechanism of Metal-Assisted CH Activation", Elsevier BV, 2013 Publication	<1%

Dmandal